STARS

Electronic Theses and Dissertations, 2004-2019

2017

Laser-induced crystallization mechanisms in chalcogenide glass materials for advanced optical functionality

Laura Sisken
University of Central Florida

STARS Citation

Showcase of Text, Archives, Research & Scholarship

LASER-INDUCED CRYSTALLIZATION MECHANISMS IN CHALCOGENIDE GLASS
MATERIALS FOR ADVANCED OPTICAL FUNCTIONALITY

by

LAURA SISKEN
B.S. Missouri University of Science and Technology, 2012
M.S. University of Central Florida, 2014

A dissertation submitted in partial fulfillment of the requirements
for the degree of Doctor of Philosophy
in the College of Optics and Photonics
at the University of Central Florida
Orlando, Florida

Fall Term
2017

Major Professor:
Kathleen Richardson

ABSTRACT

Glass-ceramics (GC) are promising candidates for gradient refractive index (GRIN) optics. These multi-phase, composite materials also exhibit improved physical properties as compared to the parent base glass resulting from the formation of a secondary crystalline phase(s). Nanocrystal phase formation in a multi-component chalcogenide glass (ChG), $(GeSe_2-3As_2Se_3)_{(1-x)}-(PbSe)_x$ glass where x = 0-40 has been investigated, and the role of the starting material morphology has been correlated to the resulting composite's optical properties including refractive index, transmission, dispersion, and thermo-optic coefficient. Optical property evolution was related to the type and amount of the crystal phases formed, since through control of the local volume fraction of crystalline phase(s), the *effective* material properties of the composite can locally be varied. Through computational and experimental studies, tailored nanocomposites exhibiting gradient index properties have been realized. A Raman spectroscopic technique was developed as a means to spatially quantify the extent of conversion from glass to glass ceramic, and to confirm that the scale length of the local refractive index modification can be correlated to the extent of crystallization as validated by X-ray diffraction (XRD). Spatial control of the crystallization was examined by using a laser to locally modify the amount of nucleation and/or growth of crystallites in the glass. A novel technique converse to laser-induced crystallization was also developed and demonstrated that a glass ceramic could be locally re-vitrified back to a fully glassy state, through a laser-induced vitrification (LIV) method. Proof-of-concept demonstrator optics were developed using furnace and laser induced crystallization methods to validate experimental and computational approaches to modify the local volume fraction of nano-crystals. These demonstrators exhibited tailorable optical functionality as

iii

focusing optics and diffractive optics. This work paves the way for the design and fabrication of nanocomposite GRIN optics and their use in the mid-wave infrared.

I dedicate this to my friends and family that have helped shape me into the person whom I have become, and to God for making me, Jesus for saving me, and the Holy Spirit for empowering me.

ACKNOWLEDGMENTS

members. I would also like to include Dr. Shah for his support through the early portions of this work.

Lastly I would like to acknowledge Dr. Kathleen Richardson for her support throughout my time at UCF. Without the effort she had spent to improve not just my scientific knowledge, but to allow me the opportunity to see the aspects of academia, national labs, industry, paper writing, and conferences I would not have the additional soft skills I do today.

TABLE OF CONTENTS

LIST OF FIGURES

LIST OF TABLES

LIST OF ACRONYMS

2PA	Two-photon Absorption
3D	Three Dimensional
ChG	Chalcogenide Glass
CTE	Coefficient of Thermal Expansion
CVD	Chemical Vapor Deposition
CW	Continuous Wave
dn/dT	Thermo-optic Coefficient
DSC	Differential Scanning Calorimeter
EDS	Electron Dispersion X-Ray Spectroscopy
f_v/V_f	Volume fraction
FTIR	Fourier Transform Interferometry
G	Growth Heat Treatment
GAP-Se	$GeSe_2$-As_2Se_3-PbSe glass
GRIN	Gradient Refractive Index
HAZ	Heat Affected Zones
HT	Heat Treatment
I	Rate of Nucleation
IR	Infrared
LIV	Laser Induced Vitrification
LLPS	Liquid-liquid Phase Separation
LWCO	Long-wave Cut-off

LWIR	Long-wave Infrared
MPA	Multiple Photon Absorption
MWIR	Mid-wave Infrared
N	Nucleation Heat Treatment
n_{eff}	Effective Refractive Index
υ_{MWIR}	Mid-wave Abbe Number
OCT	Optical Coherence Tomography
PCM	Phase Change Material
PTR	Photo-thermal Refractive
QCL	Quantum Cascade Laser
SAED	Selected Area Electron Diffraction
SEM	Scanning Electron Microscope
SWIR	Short-wave Infrared
RIU	Refractive Index Units
RMS	Root Mean Square
RR	Repetition Rate
RT	Room Temperature
SWaP	Size, Weight, and Performance
SWCO	Short-wave Cut-off
TEM	Transmission Electron Microscope
T_g	Glass Transition Temperature
T_m	Crystal Endotherm Temperature

T_P Crystallization peak Temperature

T_x Crystallization Onset Temperature

U   Rate of Crystallization

XRD   X-ray Diffraction

WLI   White Light Interferometry

1   MOTIVATION

1.1   <u>Infrared optics</u>

Infrared (IR) optical systems have increased in their usage across many different commercial applications, as well as in their more traditional role in military and defense. These systems are now commercially used in medicine [1], the automotive industry [2], safety [3], security, and quality control [4]. In military applications they are now found on vehicles, ships, planes, and soldiers for use in both night vision imaging systems and in low visibility conditions such as dust or fog.

Some problems that have plagued IR systems are that they tend to use expensive, bulky optics and costly, large, externally cooled, large pitch detectors. These attributes have limited the applications of these systems to use in military and defense where the cost and bulk of the system is outweighed by the benefits of its use. With recent advances in detectors and their reduction in size and cost, there exists a parallel need to enhance the optical components, either in their optical function and/or compactness. This push for systems with reduced size and weight, while maintaining or improving optical performance (SWaP) in both commercial and non-commercial applications will enable greater application of IR imaging systems across diverse platforms. Additionally there is a push to make the systems more affordable. Unfortunately, there exists a chicken and the egg problem for detector cost and development, which is one of the main costs of IR systems. An increased demand is needed to decrease the cost of manufacturing the detectors and to have investors willing to invest in their improvement. The cost though has been too high for commercial applications, which would much more easily increase the demand on the detectors. The other main cost of the system is the optics, which is

largely from the production of the material used and shaping these materials into their final form. These costs in the optical systems can be reduced through the use of new materials and forming techniques, and is less dependent on the product demand to bring about improvements.

Traditional optical imaging systems in the IR utilize bulk crystalline optics which are expensive to make and form into optics. Additionally there are a limited number of IR transparent crystals that can be manufactured into their desired size, shape and form, which means there are limited material properties that designers can use to optimize system performance. This necessitates the use of additional optical elements to be able to correct for various aberrations in the system. One avenue that has been used to increase the available material property values, and to reduce fabrication cost with techniques like precision glass molding [5], are IR transparent non-oxide glasses.

1.2 Non-oxide glasses

Non-oxide glasses that are transparent out into the LWIR include chalcogenide glasses (ChGs) and halide glasses (based on group VII constituents). Halide glasses are typically soft and less thermally robust, limiting their use in optical systems that have rugged environmental specifications [6]. This work focuses on ChGs, glasses which contain at least one chalcogen, and typically include other glass formers or intermediates such as As, Ge, Ga, and Sb. Additional elements can be added into these glasses, which in turn change both their structure and resulting material properties, with the most important properties to the current discussion being the glass' optical properties.

The glass forming ability of each compositional family is dependent on the specific composition used, as well as the quenching method (thermal history) used to bring the

molten material below the glass transition temperature down to room temperature. The glass forming region of certain compositions can be extended by using constituents that aid in modifying the glass network (modifiers and intermediates), and also by using more aggressive quenching techniques such as forced air [7,8], water [7,9,10], or ice water [1,11] as compared to a traditional static air cooling environment. Each glass composition also has its own resistance to crystallization and it is a general rule that small melts, while more easily quenched to a glassy state, do not possess the compositional homogeneity (high quality mixing) needed to yield optically homogeneous materials. For commercial glasses this resistance to crystallization (often referred to as crystallization stability) needs to be high in order to produce melts of commercial size with high optical (refractive index) homogeneity, but needs to be lower if one is interested in intentionally inducing crystallization in the material after glass formation. The balance of these competing factors, represents the regime examined in this dissertation. The challenge of working near the barrier of 'devitrification', the region where an originally vitreous glass is near the thermodynamic threshold of crystallization onset, while preserving the attributes which would allow the creation of material with good optical quality (low loss and manufacturability), is at the core of the present effort.

Chalcogenide glasses have high transparency in the IR due to their low phonon-energies from the relatively large atomic weights of the constituent elements [12-14]. With the ability to modify the transmission window and refractive index by tailoring the composition of these glasses, there is a large potential for infrared systems to be able to capitalize on these materials. Figure 1-1 below shows several example transmission

windows for the different types of ChGs. As the included constituents start to have larger

atomic sizes/weights, the transmission window of the glass shifts further into the IR.
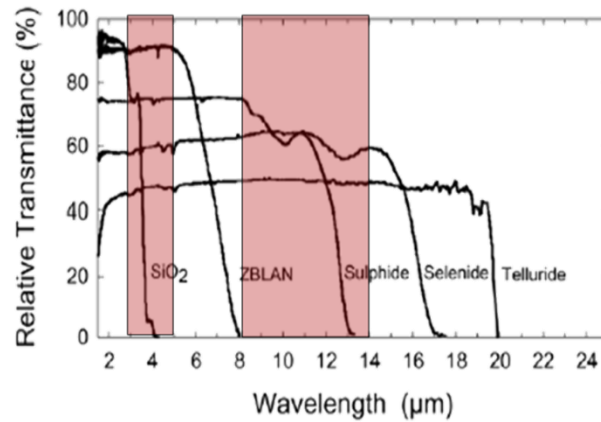
Figure 1-1 The transparency ranges for various glasses in the IR are shown with the highlighted regions being the MWIR and LWIR transmission windows. As the mass of the constituent atoms increases from oxides, through the different chalcogenides into the Tellurides, the LWIR cut-off wavelength increases (multi-phonon edge). [15]

Of the many glass-forming compositions and glass families of ChG, there are still

only a handful of commercially available compositions. One reason for this is the poor

thermal and mechanical properties that normally occur in these glasses, including low

thermal conductivity [16], low heat capacity [16], low fracture toughness [17], low glass

transition temperature, and increased photo-sensitivity compared to many other optical

materials, especially silicate glasses. Additionally some compositions are not as thermally

stable against crystallization and thus, are unable to be scaled up in commercial

production. Another class of materials that can be used to increase the available materials

for use in MWIR optics are glass ceramics.

1.3   Glass ceramics

Glass ceramics are materials that have crystalline precipitates inside of a glassy

matrix. These composites often have improved material physical properties than glasses

on their own (often referred to as the parent glass from which conversion/partial crystallization results). Additionally, glass ceramics are attractive in that they maintain their ease of formation (glass melting versus crystal growth) and fabrication (precision glass molding) as much of the forming is largely done while the material is in its 'glassy' state, prior to crystallization. Glass ceramics have been shown to possess the added benefits of improved thermal and mechanical properties, specifically hardness and fracture toughness, realized by adding precipitates with a higher fracture toughness and lower thermal expansion [18,19]. This is especially attractive for infrared glasses as they tend to be plagued by low glass transition temperatures and low fracture strength, dictated specifically by the weak bonds of the covalent network that links the large, highly polarizable atoms that make up the glass' network. In order to create the crystallites inside of the parent glassy matrix in a controlled manner avoiding spontaneous random growth, the material must be nucleated and then grown using a composition specific time/temperature heat treatment protocol.

Glass ceramics typically start with a parent glass material, a fully vitreous solid with no long-range order. Through a secondary thermal treatment that is specific to the composition, crystallites controllably grow following thermodynamically defined nucleation and growth rates, defined again by the chemistry of the melt and the thermal history of the glass. These crystallites are then able to improve the thermo-mechanical properties of the base glass alone. One way this occurs is through an increased fracture toughness. This occurs when a crack propagates through the material and runs into the crystalline inclusions, which are harder than the glassy matrix, and arrest further crack propagation into the glass. The thermal expansion of the material can also be reduced if

the crystalline phase has a lower coefficient of thermal expansion, as the total thermal expansion of the material can be approximated with the lever rule of how much of the volume fraction is in each phase and their respective values of the coefficient of thermal expansion.

Traditionally, glass ceramics are formed through a two-step heat treatment (HT) process [20,21] or through the use of nucleating agents added to form the seeds of crystallites which reduce the activation energy barrier required for subsequent growth. This growth is enabled through a secondary HT (growth) step [22]. Without a nucleating agent, homogeneous nucleation is realized by a first step that nucleates the glass. This process results in seeds or nanosized nuclei (typically several atoms in size) that can later be grown into crystals. There are two types of nucleation, homogeneous and heterogeneous nucleation [22]. Homogeneous nucleation occurs through density fluctuations and diffusion within the material that enables species to migrate to form a critical radius nuclei that remains stable in the competition of surface and volume free energy [22]. Heterogeneous nucleation on the other hand occurs at the sites of included nucleating agents or at phase boundaries where the driving force for crystallization is lowered due to the existence of the boundary [22]. The number density of nuclei, which are later grown to form crystals, is dependent on the temperature and time of the nucleation step. Once nuclei are created, they can then be grown into crystals in a secondary HT step. If no nuclei are present, crystallization cannot proceed. The final size of the crystals depends on the temperature and time of the growth step. While these can occur randomly, nuclei formation and subsequent growth in an optical glass ceramic

requires control of number density and size of crystallites demanding control of both steps in the process. These steps are depicted in Figure 1-2.

Base	Nucleated	Grown
V_g = 100%	V_g = 100-V_x%	V_g = 100-V_x%
	Where V_x is small	Where V_x is 10-20%

V_g = volume fraction of glass
V_x = volume fraction of crystal
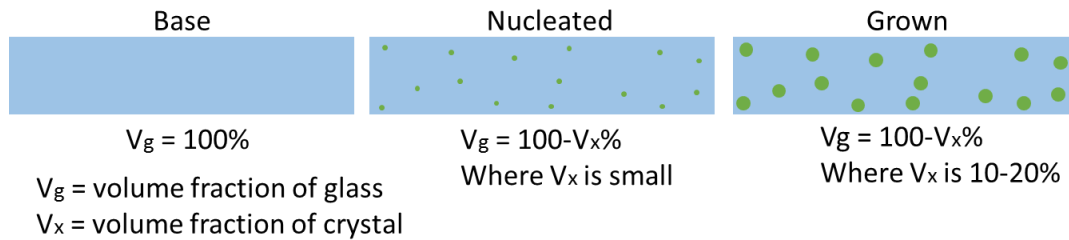
Figure 1-2 A glass ceramic starts out as a base glass, with no crystallites inside, with a 100% volume fraction of glass. After a nucleation step, there is a small number of nuclei formed which dictate the sites where subsequent thermal treatment will enable crystal growth. Following a secondary growth HT, constituents from the parent glass diffuse to the nuclei and grow to larger sizes resulting in a desired volume fraction of crystals. V_g is now reduced by a proportional amount; V_x for our studies where maintaining optical transparency is required, typically reaches 10-20%. [23]

A separation in the temperatures where nucleation and growth process of the crystals occurs is essential when creating optical glass ceramic in order to controllably form nuclei and then grow the crystals to minimize scatter losses from large size distributions and/or large crystal sizes. If nucleation and crystallization are both occurring at the same time (i.e., at a temperature where the *rates* of each process is high), then there will be a large distribution of crystal sizes as nuclei will continually be forming and crystals will be growing at the same rate as ones that formed before it. In a material with separated I-U curves, only nucleation or only growth will occur at a given temperature. We depict this construction of both the nucleation (I) and growth rate (U) curves, as a function of temperature in the schematic illustrated in Figure 1-3. Nucleation and growth curves can be quantitatively constructed via thermal analysis to determine if a material has a separation between its nucleation and growth temperature regimes, and what temperatures should be used for nucleation and growth steps in the material. Most

materials will not have a pristine I-U curve such as that shown in Figure 1-3, rather, they will have at least a partial overlap in their nucleation and growth curves. This makes the curves necessary to determine the appropriate temperatures that need to be used to control both nucleation and growth processes in the formation of an optical glass ceramic.

In order to characterize the nucleation and growth rates of the base glass material of interest, I and U curves can be created. The I curve shows the nucleation rate of the material as a function of HT temperature, while a U curve shows the growth rate of a material as a function of HT temperature and shown in Figure 1-3. The curves show a decreased rate at low and high temperatures, which are from the kinetic and thermodynamic barriers respectively [24].
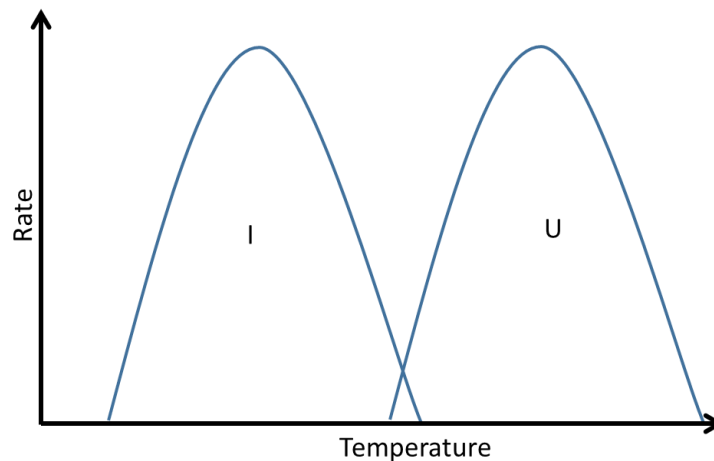
Figure 1-3 Representative nucleation and growth rate curves are shown, where I is the nucleation rate curve, and U is the growth rate curve. [23]

To create absolute IU curves, one needs to nucleate different samples at different temperatures for a different durations and then grow at a fixed, high temperature for a fixed amount of time to grow the crystals to a large enough size to be able to be seen through microscopy. The number of individual crystals are then counted and the nucleation rate for each temperature can be calculated [25,26]. To create the U curve,

samples are grown at different temperatures and different times, with or without a previous nucleation step, and then the average size of the resultant crystals are measured for the different times at each temperature in order to calculate the growth rate [25,27]. With a lack of IR microscopes, particularly in the MWIR and LWIR, this technique is non-practical for many ChGs except with the use of SEM/TEM. Small angle X-ray scattering along with XRD would be able to extract the growth rates of the material assuming that there is isotropic growth, and would potentially be able to give information about the nucleation rate assuming that one knows the shape of the crystals that are formed as these techniques give information about the size of crystals and the total volume fraction of them. Additionally, the methods discussed in the above references rely on the assumption that there is a single crystalline phase formed, which often is not a suitable assumption in multicomponent glass systems. Despite these limitations, a calculation of the *relative* I or U rate is sufficient to determine what temperatures should be used to induce mainly nucleation or growth in the material at a given temperature.

The method used to create nucleation- and growth-like curves (relative I-U curves) has been developed by authors in a variety of glass systems [20,21,28]. As I-U curves are composition specific and not known for most glassy materials, the technique is tedious and time consuming but necessary for carefully constructing heat treatment protocols for optical glass ceramics. The process uses the thermo-gram of a differential scanning calorimeter (DSC), as seen in Figure 1-4. The main features in this thermo-gram are the glass transition region, and crystallization peaks. The glass transition temperature, T_g, is measured as the inflection point (minimum of the 1st derivative of the heat flow signal) on the left hand side of the dip on the left side of the plot. The crystallization peaks are

9

the peaks shown on the right hand side of the plot. The peak crystallization temperature, T_p, is the peak of a crystallization peak, and the crystallization temperature, T_x, is the onset of the first crystallization peak. The presence of multiple crystal peaks is indicative of several crystal phases that are able to form in the glass at high temperatures. The stability of the glass against crystallization is defined as T_x- T_g, and if this value is greater than 100°C it is considered thermally stable against crystallization [16]. A high stability against crystallization is not beneficial for glass ceramics, as controlled crystallization is wanted. On the other hand, too low of a glass stability could lead to crystallization occurring during glass forming or the crystallization process may be uncontrollable.
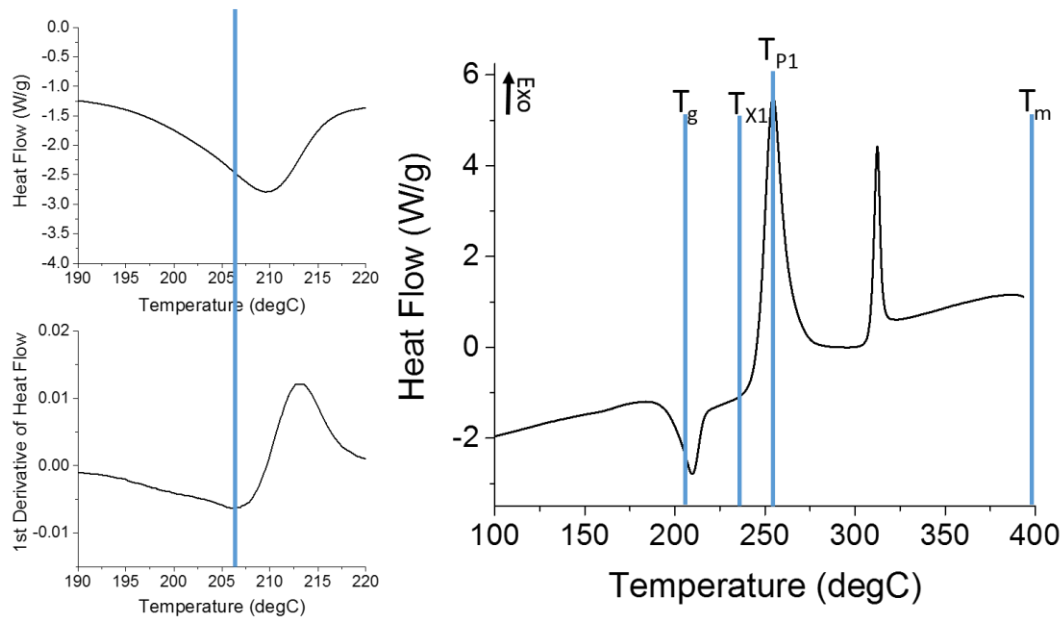
Figure 1-4 In a DSC thermo-gram there are three main features, including an endothermic dip (left upper figure) where the inflection point or the minimum of the first derivative of the slope (magnification of this region is on the left lower trace); this temperature defines the glass transition temperature (T_g) determined to be 208 °C in the present example; exothermic peaks from crystallization (shown at right) define the onset of the first crystallization peak (T_{x1}) and peak temperature is T_{P1}. A secondary endothermic dip occurs at higher temperatures (not shown here) at a temperature which corresponds to the melting endotherm of the first crystalline species (T_{m1}). The figure here depicts two crystallization peaks, due to two phases of crystals present in the glass.

To make the relative I-U curves, the size and position of the first crystallization peak is tracked for different HTs that are performed on the glass. For the nucleation-like curve the sample is heated to a nucleation temperature and then held isothermally for a specified amount of time. The temperature is then dropped to below the glass transition temperature of the material, and a traditional DSC run is performed. The location of the first crystallization peak is then determined. This process is continued for different potential nucleation temperatures. The nucleation-like curve is then created by plotting Equation 1 for each HT temperature used, where I is the relative nucleation rate, T_{pi} is the peak crystallization temperature for no HT and T_{px} is the peak crystallization temperature for a given HT temperature. [20,21]

$$I = \frac{1}{T_{pi}} - \frac{1}{T_{px}} \tag{1}$$

For a growth-like curve the sample is heated to a growth temperature and then held isothermally for a specified amount of time. The temperature is then dropped to below the glass transition temperature of the material, and a traditional DSC run is performed. The area under the first crystallization peak is then determined. This process is continued for different potential growth temperatures. The growth-like curve is then created by plotting Equation 2 for each HT temperature used, where U is the relative growth rate, a_i is the peak area for no HT and a_x is the peak area for a given HT temperature. [21,28]

$$U = a_i - a_x \tag{2}$$

With knowledge of the relative nucleation and growth rates, glass ceramics can be created with controlled number density and crystallite size.

Glass ceramics can be created from a wide range of glass compositions that cover spectral regions from the visible into the IR, for both optical and non-optical applications.

For optical applications, the crystallites typically need to be $\leq \lambda/10$ for the wavelength of use (λ), and of a similar size in order to minimize scattering from the crystallites. This wavelength scaling of crystal size allows for larger crystals to be able to be crated in IR glass ceramic, while maintaining optical transparency in the wavelengths of interest.

Commercially made optical glass ceramics include ZERODUR (Schott) and VISION (Corning). ZERODUR is a lithium-aluminosilicate glass that has a very low coefficient of thermal expansion. This composite material is generally not optically clear, and is used for non-optical applications where a low CTE is needed, such as mirror substrates in telescopes. VISION glass ceramics are semi-transparent and often used for cookware. These materials are able to withstand high heat and sudden, large temperature changes. The thermal properties, coefficient of thermal expansion (CTE) or thermal shock coefficients, were able to be tuned in these materials by tuning the type and amount of the crystal phase that was precipitated in the formation of the glass ceramic. Here, one of the precipitated phases has a negative CTE while the second phase's CTE is positive.

Another non-optical application of glass ceramics is its use in bone grafts in biomedicine [29,30]. Bio-active calcium phosphate glasses with MgO and TiO_2 have had their glass ceramic crystallization mechanism studied. With these glasses being non-optical, there is not a restriction on how large or optically scattering the crystals are. This allows for more tailoring of the type and amount of crystals needed for the composite to be bioactive [29]. The different crystal phases that are able to be formed in these composites can effect properties such as degradation rates in the human body [30].

While halide containing non-oxide glasses are largely not used in many systems due to their poor thermal-mechanical stability, alkali-halide containing chalcogenide glasses

12

have been widely studied as candidates for use as optical glasses and glass ceramics [17,31-35]. Depending on the amount of halide added into the material, the transparency can span from the VIS into the LWIR. One glass system that has been extensively studied is the Ge-Ga-Se glass forming region with incorporations of alkali halides such as KX and CsX, where X = Cl or Br. The addition of these metal- or alkali-halides helps to facilitate homogenous, controlled crystallization in these glasses. These types of glass ceramic have been able to maintain transparency from the NIR through LWIR (for short HT), reduce the expansion coefficient [36], and modify the hardness of the material. Additional studies of these glasses with RbI, were able to show molding of the glass-ceramic, where the molding process did not affect the transparency or distribution of crystals in the glass ceramic [18]. This specific glass ceramic has the potential to create low dn/dT materials, as the RbI crystals have a negative dn/dT and could cancel out part or most of the positive dn/dT of the parent glass.

Apart from evaluating how the specific glass' composition impacts material property changes, additional studies have investigated the role of the parent glass composition on the glass' respective crystallization mechanism. In a $65GeSe_2–25Ga_2Se_3–10CsI$ glass shown to exhibit liquid-liquid phase separation (LLPS), crystallization was not seen until after the glass' droplet phase had a maximum number of droplets, and it was surmised that these droplets were Ge_2Se_3 rich, and that the crystals form in these regions [17]. While limited efforts were made to correlate chemistry to phase formation, this glass family was not examined for correlation of specific properties to parent glass morphology. The study highlighted that the glass was useful for several applications

13

since it has high rare-earth solubility suitable for active applications, which increases with an increase in the gallium content.

Additionally, these halide-free glasses have also been made through ball-milling and sintering of the starting constituents. This technique has shown to result in the production of glass compositions that would normally crystallize upon melting for sizes that are of use for optical applications. Transmission of these glasses were shown to extend between 2-11μm [37]. Additionally, these glasses can then be heat-treated the same way as other glasses to form glass ceramics. Upon crystallization (also referred to as 'ceramization'), using a 390°C thermal heat treatment protocol for 2-60 min, a decrease in the density, an increase in the Young's modulus, a decrease in the Vickers hardness, and an increase in the toughness was observed [37]. On the other hand in a study on a different glass system, [8] researchers saw an increase in the Vickers hardness with crystallization of Ge-As-Pb-Se glass with precipitation of PbSe and $PbSe_2$ crystals.

Hence, the choice of parent matrix and extent/type of precipitated phase formation, is critical to defining both the desired post-heat treated glass ceramic microstructure and resulting physical properties of the glass ceramic. As will be discussed for the present work, the primary target properties of interest are optical properties. It is also noted that both the optical and other physical properties resulting in the formation of the optical nanocomposite (glass ceramics having a nano-scale secondary crystalline phase) will also play a role in the resulting glass ceramic's function.

1.4 $GeSe_2$-As_2Se_3-PbSe (GAP-Se)

Another system that has been recently studied by our team and others, is the multi-component chalcogenide system $GeSe_2$-As_2Se_3-PbSe (GAP-Se). This system was

originally studied by researchers at the University of Rennes (France) [31,38]; they showed that the glass forming region for this composition is to the left of the red line seen in Figure 1-5. These early studies focused on forming glass ceramics with a high volume fraction of crystallites using a single, long HT at low temperatures, where nucleation would occur quickly and growth would occur slowly. These conditions were used in order to have a high density of small crystals [38]. Further studies have been conducted that expand upon material properties of both the base glass and glass ceramic for multiple compositions [39,40].

The $(GeSe_2\text{-}3As_2Se_3)_{1-x}PbSe_x$ tie-line, where x=0-40 in increments of 5%, has been studied [39,40], and is depicted in Figure 1-5 as the dashed blue line. The amount of Pb was varied, as it was postulated that an increase in Pb content would increase the potential for precipitation of a high-Pb containing crystal phase. The appearance of such a phase, readily formed by the reduction in glass stability imparted by Pb in the glass, would also enable easier precipitation of Pb-containing crystallites. A secondary motivation was that Pb-containing crystals would be high index, and a small volume fraction would result in a measurable increase in the glass ceramic's refractive index. These details will be discussed in subsequent sections.

The physical properties of the base glass used in this study can be found from these studies [39,40]. The most pertinent information in those studies with respect this work is base glass morphology, glass transition temperature, peak crystallization temperature, and relative nucleation and growth rates.
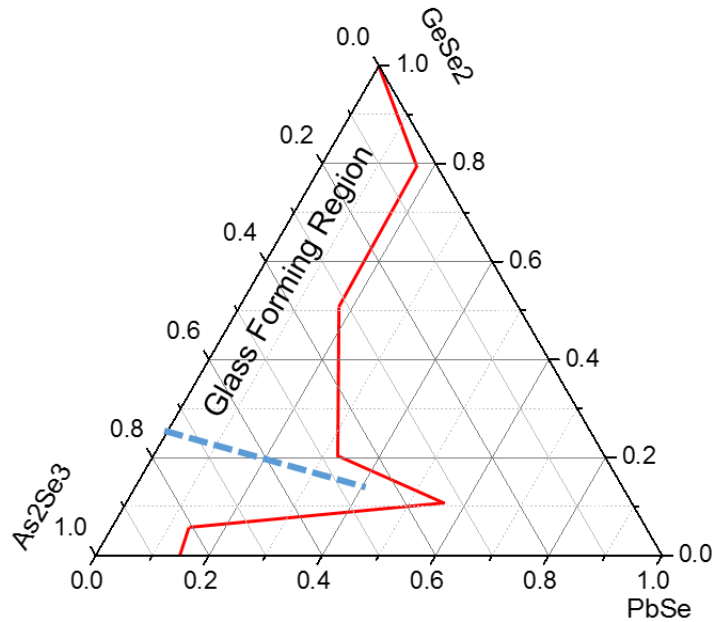
Figure 1-5 The glass forming region of $GeSe_2$-As_2Se_3-PbSe is to the left of the red line. The blue dashed line is the tie-line of a 1:3 $GeSe_2$ to As_2Se_3 ratio used in this study. [41]

In both these studies and others on similar non-stoichiometric (composition cannot be written as a sum of constituent materials ie. $GeSe_2$, As_2Se_3, and PbSe) variations with the same constituents a large region of LLPS was observed [42,43]. This phenomenon may be common in other glasses with these constituents as it was seen for such a wide range of compositions in both studies. This region of phase-separation in the glass is commonly referred to as the immiscibility dome. In [40] homogeneous glass was able to be achieved below 10 mol% PbSe, and above 40 mol% PbSe. Between 10 and 25 mol% PbSe droplets that were Pb-rich, and As and Ge-poor. Between 35 and 40 mol% PbSe, the opposite was observed. In between these two regions, spinodal decomposition is observed. An overview of the base glass morphology in terms of droplet size and composition is in Table 1-1, and additional information for above 40 mol% PbSe can be found in [40].

16

Table 1-1 The phase morphology of the GAP-Se base glass samples exhibiting LLPS is shown, including the size and Pb-content within the two glass phases for select compositions. [40]

Mol% PbSe in Glass	Total at% Pb	Phase separation diameter (nm)	At% Pb In Matrix	At% Pb In Droplet
0	0	0	0	0
5	1.14	0		
10	2.35	150	1	13.5
15	3.64	150		
20	5	100	1.7	12.3
25	6.45			
30	8	50	9.5	6.5
35	9.66	50		
40	11.43	50	13	7.3

With such compositional changes present in the base glass' morphology, transitions were seen in many of the physical properties that were measured on the base glass in these studies. Differences were also seen in the changes of material properties with the amount of Pb in the glass. According to [39] the amount of change seen is partially determined by the starting phase morphology. The composition in the two separated phases effects the crystallization behavior of the material, and the Pb-rich droplets change composition much more rapidly with small additions of Pb into the glass, while in the Pb-rich matrix small additions of Pb change the composition of this Pb-rich matrix material much less. Additionally, the base glass morphology is also affected by the batch size and cooling rate of the glass. As was seen in [39] where there were changes in the droplet size and in the optical homogeneity of melts of different sizes and/or cooling rates. These changes in the phase separation were then seen to affect the nucleation of the material (i.e. slower cooled showed evidence of nucleation from the quenching process). The density and index of the melts were also affected.

Besides the base glass morphology, the glass transition temperature and peak

crystallization temperature are also pertinent for this study and give information on the

stability of the glass. These values are listed below for the different compositions in

Table 1-2, and additional information can be found in [40]. As the PbSe content was

increased, a decrease is seen in the temperature of the first crystallization peak and the

glass transition temperature remains fairly constant [40]. This causes the glass stability to

decrease. After 55 mol% PbSe, the material is no longer able to form a glass and

crystallizes upon quenching even for small melt volumes ($< 10g$).

Table 1-2 The glass transition temperature (T_g), peak crystallization temperature (T_{px1}), and glass stability (ΔT) are shown for the different compositions used in this study. [40]

Mol% PbSe in Glass	T_g (°C)	T_{px1} (°C)	$\Delta T = T_x - T_g$ (°C)
0	210	N/A	N/A
5	203	353	149.8
10	210	355	144.9
15	200	317	116.24
20	201	304	102.4
25	202	294	92.7
30	201	285	84.1
35	201	271	70.6
40	200	258	58

Relative nucleation (I) and growth (U) rates within the GAP-Se system were

constructed as part of the study by Buff and co-workers [39] for the 20 and 40 mol%

PbSe samples. In this work, it was shown that the absolute position in temperature space

(onset of nucleation and growth rates within the I-U curves) was impacted by the size of

the glass melt, which was expected from the variation in 'thermal history,' if a larger melt size is cooled. As will be discussed in [44], this result impacts the resulting LLPS in both the size (of secondary droplets) and composition (in this case, Pb content in either the droplets or matrix). As one might expect, the size and composition scales with the melt size and melt/quench conditions. As ChGs are typically poor thermal conductors, larger melts will likely have higher concentrations of 'frozen in nuclei' intrinsically formed. A shift of the U curve to higher temperatures is seen for the lower Pb-content glass. This is reflected in Figure 1-6. From these two figures, one can see that the choice of heat treatment temperature in a typical two step nucleation and growth protocol, will distinctly define the number of nuclei formed in the first step that subsequently grow in the second heat treatment step. Additionally, if a nucleation step was performed before the growth step, a shift to lower temperatures was seen for the growth curve as compared to a protocol employing a single 'growth only' thermal processing step. This additional nucleation step allows for more crystal sites to grow during the growth step for lower temperatures where spontaneous crystallization may not normally occur, but crystallization can occur if a nucleation site is present.
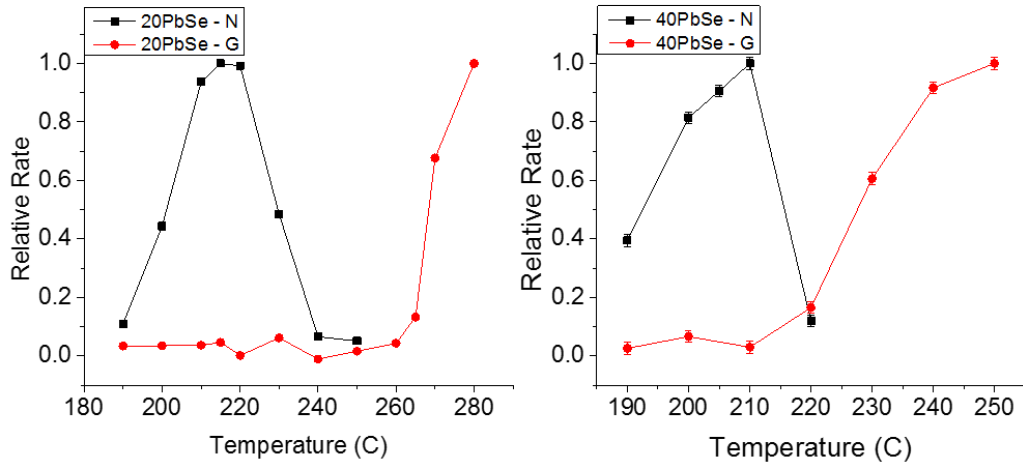
Figure 1-6 Nucleation and growth-like curves are shown for the 20 (left) and 40 (right) mol% PbSe compositions [39,41].

Spatial control of this crystallization process opens new doors into the optical functionality of components by enabling the control of nuclei formation and/or by crystal growth within the material. If one can spatially control the formation of nuclei and/or their limited growth (crystallization) while avoiding any spontaneous crystal phase formation, an optical component with spatially defined optical functionality, or refractive index can be developed.

1.5   Gradient refractive index optics

Besides creating new optical materials, another way to expand the optical design space for IR optical systems is to decrease the number of optical components by adding optical functionality into the individual components. An approach investigated over the past decades to enable this largely in visible materials, is through the use of gradient refractive index (GRIN) profiles. GRIN profiles in materials have been shown to correct for dispersion in [45,46] as well as other aberrations [47,48] in IR transparent glasses. The use of GRIN functionality has also been shown to reduce the time and cost of

20

manufacturing elements by eliminating the need to make aspheres over spherical optics [47,49]. Ideally if one could have full three dimensional (3D) control of a material's refractive index, then all aberrations could be accounted for and little to no shaping of the optic past a planar surface would be needed [50]. This could drastically reduce the number of elements needed while improving the optical performance of a system, which in turn would greatly decrease the SWaP and increase the potential for the system to be used in commercial applications [46,51]. These issues form the underlying motivation for our work, specifically applied to materials suitable for use in the infrared.

There are multiple techniques that have been developed in order to create GRIN elements for various wavelength ranges, with each fabrication technique utilizing different materials and different potential GRIN profiles that can be created with them. Some current techniques used to form GRIN materials are ion exchange [52-55], thermal poling [56-58], chemical vapor deposition (CVD) [47,59,60], stacking and pressing of different material layers [61-67], metamaterials [68,69], photo-induced changes [70-72], and induced ceramization [73-75].

1.5.1   GRIN by the ion-exchange method

The traditional method developed initially by researchers at the University of Rochester to create GRIN optics for visible applications is through ion exchange, with the most typical materials being Na_2O-based glasses immersed in $AgNO_3$ solutions to promote an exchange of Na for Ag ions. The diffusion of the Ag particles into the glass, while being exchanged for the similar ionic radius Na ions, forms a compositional gradient of these ions, which causes a gradient in the glass' polarizability and refractive index. Through different processing parameters, various profiles can be created, though

21

the shape of the exchange profiles are limited to typical monotonic depletion to the diffusion process. The process also is often vary time consuming. Typical index changes seen with this technique are 0.04-0.09. [52-55]

1.5.2   GRIN by the thermal poling method

Similar to ion exchange, thermal poling has been shown to enable the re-distribution of atoms within a glass through the application of an electric field (between electrodes) at elevated temperature. Such migration of ionic species within the glass can modify the resulting macroscopic structure, imparting asymmetry to the typical centrosymmetric nature of amorphous glasses' resulting in a change of the material's $\chi^{(2)}$ and $\chi^{(3)}$. Using structured (patterned) electrodes to control where mobility occurs (or not), spatial control of charge migration can result in compositional gradients which result in modification to the chemical reactivity and also the optical properties within a single glass material. Poling is a technique that was first applied to glass in the 1990's and employs an applied electric field and its resulting current to induce migration of a charged species within the glass. Such field-induced mobility creates anisotropy in a glass leading to an induced χ^2 that results in measurable second-harmonic generation. It has recently been shown that through patterning of the electrodes used on the glass (rather than using a blanket, homogeneous ITO coating for example) the induced field profile results in a non-homogeneous diffusion of the mobile ion species. This field gradient then gives rise to a mobility gradient which translates to a gradient in the glass matrix chemical composition, and thereby, its refractive index. Demonstrated in both oxide [56] and non-oxide glasses [57], the induced effective refractive index change (Δn_{eff}) can be on the order of ~0.02. Also with compositional tuning to restrict post-poled ion mobility, an index change can

be made to remain stable over long periods of time (> 6 months shown to date). Using the resulting gradient index profile from micro-structured electrodes, micro-lens arrays have been demonstrated using this technology based on a patented process [58].

1.5.3 GRIN by chemical vapor deposition

CVD is a GRIN methodology which can be used for materials in both visible and IR wavelength regimes, for crystalline or glassy species. Two main applications of CVD GRIN have been reported for optical fibers [59,60] and ZnS/Se [47]. Creating optical fibers with a radial gradient in the refractive index are commonly made by changing the doping levels of an additive, most commonly with Ge, as the deposition of the glass is occurring. The typical index variation for this process is ~0.01-0.02. ZnS/Se CVD GRIN is made by changing the amount of S versus Se in the CVD process along with a constant amount of Zn. Since the crystal structure of ZnS and ZnSe is the same and their lattice parameters are similar in size, both compounds form a solid-solution and a gradient of species can be produced. This change in amount of S for Se can create an index change of 0.2. CVD GRIN are limited to either axial or radial distributions, since the deposition process proceeds by layers. [47,59,60]

1.5.4 GRIN by stacking and pressing of different material layers

Stacking and pressing material layers of differing index has been accomplished for both polymers in the visible, and for glasses in the IR. For polymer GRIN structures, the individual material layer thickness is typically 50 μm with the index step between layers being minimal, and a total change in index of 0.04-0.09 has been performed. For glass GRIN elements the typical material thickness is on the order of mm, with a maximum total index variation of ~0.8. These structures can be formed by vertical stacking of

sheets (axial), or by stacking tubes inside of each other (radial). Due to the glassy nature of the material, a diffusion HT can be performed in order to smooth out the index profile eliminating sharp interfaces (distinct steps) between dissimilar materials. For both the polymer and glassy GRIN materials, the resultant GRIN stack can be deformed through hot pressing, and then be polished into a final lens structure. This coupling with pressing allows for more GRIN profiles inside of an element other than either the strictly axial or radial geometries which are limited by diffusion alone. The GRIN structures from this technique have flexibility with the potential profiles created, but they are not able to create fully arbitrary profiles as they are limited to the spatial variation in directions perpendicular to the stacking. [61-67]

Recently, advances have been made to dissolve various compositions of ChGs into solution [76-78] which enables the creation of ChG films of high optical quality that are suitable for use as conformal coatings. This solution-derived glass approach results in homogeneous glass solutions which upon thermal treatment to remove solvent, yields ChG layers with properties similar to the parent bulk glass. This processing advancement has led to the possibility of directly 'printing' unique optical features such as microlens arrays [79] and the incorporation of optical nanoparticles and quantum dots [80]. Using a 3D electrospray process, GRIN structures [81,82] have been formed by spatially varying composition and thickness of layers to result in multiple layers with gradients in effective refractive index, n_{eff}.

1.5.5   GRIN by metamaterials

Metamaterial GRIN materials have been created in systems such as Si, Ge, or in metallic nanostructures. These materials are planar, and therefore have limited

applications where they can be used. They do though have full spatial control of the index in the two dimensions they possess, and can have large index changes on the order of 2. Here the resulting GRIN results from dissimilar index materials (usually the parent material and air) where the patterning process removes materials to yield uniformly shaped air holes of defined dimensions, or an array of features of high and low index, with varying packing density (volume fraction). This approach relies on the parent material being 'etch-able' either via wet or dry processing routes and is complex in crystalline materials which exhibit preferential etch selectivity related to their crystallographic orientation. [68,69]

1.5.6 GRIN by photo-induced changes

Photo-induced changes have been used to create index changes over spatial dimensions of μm to mm scale. This technique typically uses glasses that are sensitive to light, including ChG, to change the index 0.02-0.1 refractive index units (RIU). These index variations though tend to be erasable at high temperatures and over time, but do have the advantage of being able to spatially determine where and how much of the index change will occur. [71,72] These modifications tend to be written as single line structures for use in applications such as waveguides if the index change is positive, or if the index change is negative such as with a waveguide cladding [70]. Blending the spatial ability of direct laser writing photo-exposure to induce a material change that lends itself to selective removal (etch or otherwise) has been shown in As_2S_3 and other GeAsSe glasses in bulk and film form [83,84]. Here, the exposing laser light serves to cross-link the exposed glass' structure, rendering it more resistant to etching. Thus patterning of GRIN

25

function of arbitrary optical behavior is realized. The process is time consuming and relies on the material's photo-structural modification ability and its etch selectivity.

1.5.7 GRIN by induced ceramization

Controlled crystallization or spatially controlled 'ceramization' of glasses has been used in multiple ways to create GRIN structures in glasses by inducing crystallites inside of a glassy matrix. The local refractive index is a function of the volume fraction of both phases present in the material (parent glass matrix and precipitated crystal phase(s)) at a given location. This allows for tailoring the final size and volume fraction of crystals enabling spatially specific modification of the local 'effective' refractive index. Using this approach, the formation of a secondary phase of crystallization in the material is stable over time and at high temperatures, unlike some laser-induced index changes which rely on localized structural reorganization (bond bending or severing) that may undergo reversal or relaxation with time or temperature (annealing).

One mature technology that utilizes such formation of a permanent, long-lived spatially defined refractive index change that is largely used in the formation of volume Bragg gratings and other optical components is photo-thermal refractive (PTR) glasses [73-75]. These glasses use UV-irradiation to form nucleation pre-cursors, and then use a two-step HT to nucleate and then grow crystals where the nucleation pre-cursors were created. The irradiation causes the cerium atoms to locally ionize, which then allows the local silver atoms to change into a neutral state. A low HT then causes these neutral silver atoms to cluster. These clusters then act as nucleation sites for NaF crystals that are grown in a second higher HT. By tuning the final size and distribution of the crystals, gradients in index can be formed. Elements from this technique are typically holographic

Bragg gratings, and utilize the two-tone index change created from areas with no crystals and areas with a high, consistent distribution of crystals. These PTR glasses come in several flavors that cover the spectral range of VIS to NIR, and can have index variations up to ~0.0005. [73-75]

For midwave (MWIR) and longwave (LWIR) IR optics, chalcogenide glass ceramics have been proposed and have been shown to be able to produce refractive index changes (Δn) on the order of 0.2 upon ceramization. Here, the Δn of the resulting optical composite, the glass ceramic (n_{GC}) can be defined as the total change of index as compared to that of the parent glass (n_{glass}). The Δn can be homogeneous throughout the resulting post-HTd material (such as through a furnace-based two-step nucleation and growth heat treatment process) where the entire material has been partially or fully converted from glass to ceramic (ceramized). Alternatively, the modification can be spatially varying if either the nucleation or growth protocol can define local regions of more or less glass ceramic or unmodified, parent glass. When the precipitated crystalline phase possesses a higher refractive index such as in the case of the materials explored in the present study, $\Delta n = n_{GC} - n_{glass}$ resulting in a positive refractive index change. The converse is also possible, depending on the parent glass and precipitated phase(s) refractive index. Since the glass ceramic is comprised of both the precipitated crystalline phase and the residual, 'depleted' parent glass, this relationship can more precisely be approximated by an effective medium approach that takes into account the relative properties and volume fractions of each of the optical composites' constituents. Equations 3-5 below, shows different approximations that can be used for an effective medium of mixtures. The refractive index was solved for using all three of these equations, in order

27

to see which best described the system used. For Equation 3, which is the Newton

equation, n is the refractive index of each constituent phase, and V is the volume fraction

before mixing.

$$n_{eff}^2 \approx n_{glass}^2 V_{glass} + n_{crystal\ 1}^2 V_{crystal\ 1} + n_{crystal\ 2}^2 V_{crystal\ 2} \cdots \quad (3)$$

Equation 4, which is the Gladstone-Dale equation, n is the refractive index of each

constituent phase, and V is the volume fraction after mixing.

$$n_{eff} - 1 \approx \left(n_{glass} - 1\right)V_{glass} + \left(n_{crystal\ 1} - 1\right)V_{crystal\ 1} +$$
$$\left(n_{crystal\ 2} - 1\right)V_{crystal\ 2} \cdots \quad (4)$$

Equation 5, which is the Gladstone-Dale equation, n is the refractive index of each

constituent phase, and V is the volume fraction after mixing.

$$\frac{n_{eff}^2-1}{n_{eff}^2+2} \approx \left(\frac{n_{glass}^2-1}{n_{glass}^2+2}\right)V_{glass} + \left(\frac{n_{crystal\ 1}^2-1}{n_{crystal\ 1}^2+2}\right)V_{crystal\ 1} + \left(\frac{n_{crystal\ 2}^2-1}{n_{crystal\ 2}^2+2}\right)V_{crystal\ 2} \cdots \quad (5)$$

While the discussion to this point has exclusively been related to the use of a two-step

thermal treatment to nucleate and/or grow the secondary phase(s) in the parent material,

alternative methods can be used to do either of these two steps. The use of laser-

irradiation to either selectively nucleate or grow the material would allow for full 3D

spatial control of the refractive index in these materials. As will be discussed in

subsequent section, the method as depicted in Figure 1-7 provides an example of a 2-D

GRIN structure which can be fabricated using this technique.
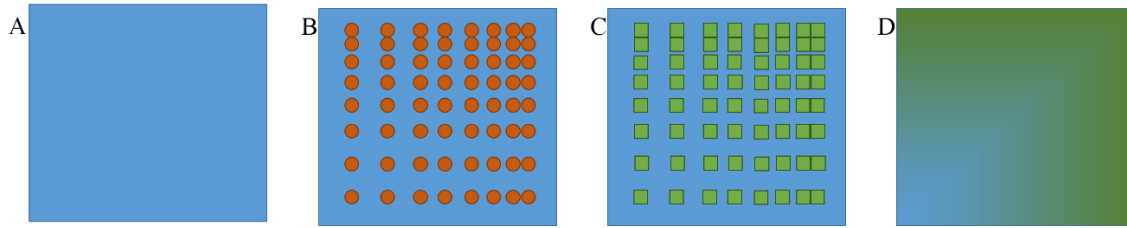
Figure 1-7 A schematic of a glass ceramic GRIN element formed from (A) a base glass that is then (B) nucleated spatially with a graded concentration of nuclei that then undergoes (C) subsequent HT so that the nuclei grow into crystals at the sites of prior nucleation (only). Here, the variation in number density of high index nanocrystals within the parent glass results in (D) an effective refractive index variation (Δn_{eff}) directly proportional to the local variation in both the volume fraction and the refractive index/indices of the crystal(s) formed. [41]

1.6   Laser-induced material modification

Laser modification of a material occurs through the interaction of the laser with the constituent electrons in the material [85]. In order for the light to interact with the electrons, the light needs to be absorbed by the material and cross over the optical bandgap of the material. For this to happen, the incoming light must have an energy that is equal to or above that of the optical bandgap of the material, and within the conduction band of the material. This excited electron can then transfer the absorbed energy from the photon to the bulk of the material through carrier-phonon coupling if the laser pulse length is long enough (ns-ps) [86]. For short laser pulses (ps-fs), there is not enough time for the energy to be transferred into the bulk through phonons, and an electron plasma is generated [86].

The light could also have an energy that is an integer fraction of energies in the conduction band of the material, and has a high enough intensity that multiple absorptions can occur nearly simultaneously. An example of non-linear absorption is two photon absorption (2PA) [87]. This can also occur with more than two photons, and is then called multi-photon absorption (MPA). For these non-linear absorptions, there needs

29

to be a high intensity of photons, since the absorption probability for multiple photons to be absorbed nearly simultaneously is much lower than that for single photon absorption. This dependence on the intensity of the incoming irradiation is the cause for the absorption to be considered non-linear. After an absorption occurs, the atom needs to relax back down into a lower energy state. This requires that the energy dissipates which can occur through a transfer as heat through phonons into the surrounding matrix of atoms bound together in the material. Additionally this energy could modify the bonds of the atom with its surrounding neighbors and can create color centers or other defects [88].

For light above the bandgap energy (shorter wavelength than the optical bandgap) the material is strongly, linearly absorbing with respect to the laser intensity as the electrons can be absorbed into the conduction band of the material on their own. In this case, the light is absorbed very close to the surface of the material, and can be considered a surface heat source for bulk material [89]. Additional non-linear absorption could also be present depending on the energy intensity of the light source as long as a multi-photon process does not ionize the material. For light below the bandgap energy (wavelengths longer than the optical bandgap) there could be both linear and non-linear absorption occurring [90]. In order to measure the contribution of each process, 2PA (typically most dominant of MPA) can be measured independently with an open aperture z-scan [90,91] or by measuring the optical absorbance for different laser pulse intensities or fluences [92], as typical absorption measurements will measure absorption processes occurring at the same time.

If the wavelength used is such that 2PA is the dominant absorption process, focusing a laser beam with a low enough intensity to not cause modification away from the focus

can then be used to modify the material only in the region around the focus. This can allow for high spatial resolution of material modification, and even be used to generate structures below the Rayleigh limit at the used wavelength [87,93].

Besides the wavelength of the light, other laser parameters such as repetition rate (RR) and pulse duration can also affect the material modifications occurring in the material. These two parameters work together to determine the irradiation peak power, as well as the amount of material relaxation between pulses. Shorter pulse durations on the fs to ps time scale equate to higher peak intensities and energy per pulse for a given repetition rate as seen from the Equation 6 for peak pulse intensity where I_p is the peak pulse intensity, P_{avg} is the average power, RR is the repetition rate, τ is the pulse duration, and w_0 is the beam waist. These higher peak intensities allow for more non-linear effects to occur, such as 2PA [85]. Additionally, since the pulse duration is shorter than the amount of time it takes for the energy to transfer from the electrons to the lattice in the form of heat (several hundred ps), the irradiation and modification is considered "non-thermal" [85].

$$I_p = \frac{1.76*P_{avg}}{w_0{}^2 \, RR\pi\tau} \tag{6}$$

The RR of the laser affects how quickly the material will heat up, and how much relaxation is able to occur before the next incoming pulse. Equation 7 below shows the characteristic length for heat to diffuse where l is the diffusion length, D is the diffusivity of the material, and τ is a characteristic time. This allows one to characterize how far the heat is able to travel during the laser pulse length, or in between pulses, depending on the characteristic time used. Heat accumulation can occur if the time between pulses is less than the time for the system to return to the starting temperature, and can cause rapid

31

heating in the material for MHz RR as depicted in Figure 1-8 [94,95]. This rapid heating

allows for a smaller heat affected zone (HAZ) than irradiations with lower RR would when

raising the material temperature to the same value [96,97]. The HAZ in a heat accumulation

regime is dominated by heat diffusion [85]. Also with the faster heating, high RR material

processing can be performed on a faster timescale, since less dwell time is needed to reach

the same temperature [96]. The RR also affects the peak pulse intensity like the pulse

duration does, as the higher the RR the lower the peak pulse intensity as shown in Equation

6.

$$l \approx \sqrt{D\tau} \tag{7}$$
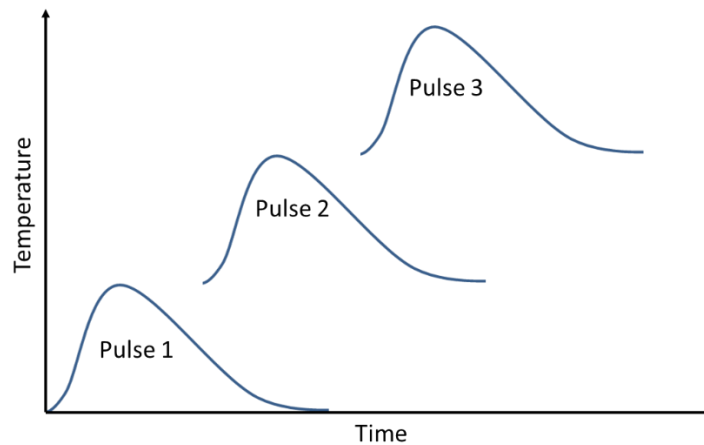
Figure 1-8 Heat accumulation occurs when the temperature increase from a single pulse
does not have enough time to completely return to room temperature before the next pulse
arrives. This can cause a rapid build-up of heat in a sample, and can impart more permanent
modification as compared to transient changes that can relax upon cooling. [23]

The pulse duration, in combination with the RR determines the peak pulse energies and

amount of heating in the material, which can affect other experimental parameters as well.

For instance, waveguides that are written with lower RR (higher pulse energy) need lower

NA objectives for writing, while higher RR (lower pulse energies) need higher NA

objectives [96]. The NA of the objective then affects the asymmetry of the waveguide, as a higher NA leads to a more symmetric waveguide.

One modification that is typically considered detrimental to forming optically transparent regions of modification, is laser ablation. Ablation though can be used in applications such as precision cutting, drilling, or polishing to remove material in a very controlled fashion and can be implemented on the micron scale [98]. The initiators of ablation include free electrons, defects or impurities, freed bound electrons, avalanche ionization, and/or electron tunneling [86]. The cause of ablation can vary depending on both the material and the laser parameters chosen.

One step just below the materials intrinsic ablation threshold is the energy threshold for melting the glass. With a laser-based process, localized melting of the material can be used in applications such as additive manufacturing, surface polishing, and welding. Lasers can be used in additive manufacturing through various methods, such as photo-curing for plastics [99], but with respect to melting it is typically used to melt layers of metal powder to solidify into the part being made [100]. In laser polishing, the laser is used to re-melt the top surface of the part so that the peaks melt into the valleys [98]. Laser welding can also be performed on various materials including metals, glasses, semi-conductors, and even combinations of these materials [101].

Below the melting point of the material, other property changes can occur that affect the chemical structure through the initiation of chemical reactions, through bond re-arrangement, or in some cases modification of existing bonds, through bond severing and reformation. One example of an induced chemical reaction is photo-polymerization, where light is used to trigger the chemical reaction that links monomers together as

33

polymers [87]. This technique is widely used in photo-lithography and 3D printing of plastics. An example of bond modification and re-arrangement is the photo-patterning of a region with a different etch rate, which depending on if it is faster or slower than the surrounding media will create a positive or negative relief structure [102]. This has been used to create micro-fluidic channels and cavities with materials such as Fotoran. Another example of processes resulting in bond changes is photo-expansion or photo-contraction of glasses, where structural modifications occur in the glass [15,103]. This expansion can cause a change in density, which can then causes changes in the refractive index of the material.

Controlled laser-induced refractive index changes were first performed by Davis *et al* in ZBLAN [104] with an ultrafast laser, and has since been performed in crystals, polymers, and multiple glass types [70,88,94]. Many of these index changes are considered metastable however, as they can often be relaxed out of the material at high enough temperatures that the bonds are able to relax back to their original state [95]. The ability and speed of this relaxation is material dependent.

One two-tone index structure with optical functionality that can be created with laser patterning is a diffraction grating. This type of structure is a diffractive optic, and is formed by linearly alternating refractive index values of n_1 and n_2 with a repeating pitch, where the phase shift of light between light traveling through the two regions is π. These can be created through either surface relief features, or index changes in the volume of the material [95]. The spacing of the alternating lines determines the angle at which the diffracted light will exit, and follows Equation 7 for incident light normal to the grating structure, where d is the distance between lines, θ_m is the angle of the light post grating, n

is the refractive index of the medium after the grating, m is the diffraction order, and λ is the wavelength used.

$$m\lambda = nd \sin \theta_m \tag{7}$$

Permanent refractive index changes can also be formed by locally inducing ceramization, as explained in section 1.5 above for laser-induced nucleation with subsequent thermal growth of crystals. The laser could also be used in the opposite technique where the entire starting glass is nucleated and then the laser locally grows the glass.

1.7   Laser-induced modification of GAP-Se materials

Efforts to use laser-induced processes to impart either nucleation or post-nucleation crystal growth has been carried out on GAP-Se materials in both bulk and thin film form. Work on GAP-Se films preceded work on GAP-Se bulk materials early in our team's DARPA program (Tech Area 2 program # FA8650-12-C-7225), as liquid-liquid phase LLPS issues in the bulk glasses (discussed below) made laser coupling into the bulk glass to realize volume refractive index modification, impossible. This previous work on 40 mol% PbSe films has shown that the deposited film is homogeneous, without phase separation [105]. Upon irradiation with a ns, 1064 nm continuous wave (CW) laser, the glass becomes phase separated and remains amorphous. This is shown in the TEM micrographs Figure 1-9 for the as-deposited, laser exposed (center) GAP-Se films [105]. Shown is evidence of laser-induced phase separation of the initially homogeneous glass film into a (still) amorphous film exhibiting liquid-liquid phase separation. If a subsequent heat treatment protocol is performed on the laser-exposed film, growth of the

Pb-rich amorphous regions of the laser exposed is then seen resulting in visible

nanocrystallites as confirmed by selective area electron diffraction (SAED).

As-deposited	Laser Exposed	Thermal Treatment

Homogeneous, Amorphous	Phase Separation, Amorphous	Nanocrystal Growth
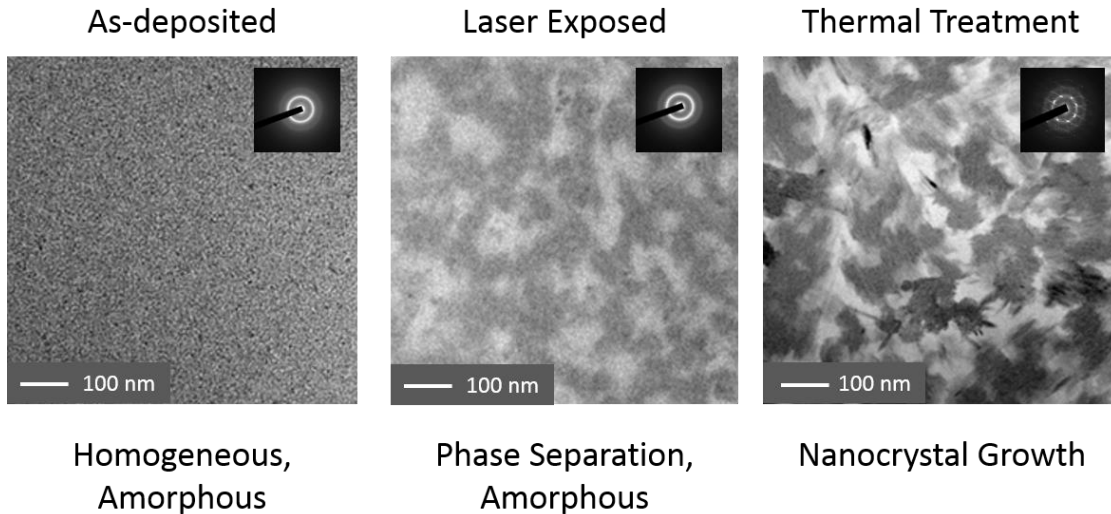
Figure 1-9 TEM images of 40mol% PbSe films, for as-deposited, laser nucleated, and furnace growth. In the upper right hand corner is a selected area electron diffraction pattern, which confirms either the amorphous nature (halo) or crystalline nature (spotty pattern) in the post-treated film. [105]

Post-irradiated GAP-Se film samples were subjected to varying HT protocols to

understand the effect of thermal growth of the post-irradiation phase separation on the

formation of the desired crystalline phases. Additionally, it allowed us to confirm if the

irradiation indeed acted as a nucleation step to induce the less stable, Pb-rich glassy phase

(shown clearly as the bright region in the dark field microscopic image in Figure 1-9,

center). Following HT, the refractive index for each of these exposures was measured in

the infrared using spectroscopic ellipsometry, as illustrated in Figure 1-10. Plotting the

resultant index measured at a wavelength of 4 μm versus HT protocol used (for a constant

laser exposure condition, discussed in detail in the paper) allowed construction of the

material's 'S-curve' which defines the process window for inducing a post-exposure

refractive index range. As shown in Figure 1-12, red data points highlight the changes in

films receiving both laser exposure and heat treatment, whereas the gold data points show the glass film's tendency to spontaneously crystallize in an uncontrolled manner after a single HT. The shift to lower temperatures for the start of observed growth shows that the irradiation was effectively able to phase separate the glass thereby 'nucleating' in this case, a Pb-rich, high index glassy phase more likely to crystallize at a lower temperature than the initially homogeneous amorphous film. Additionally, the S-curve provided insight on a process window intrinsic to the material whereby the locally exposed regions could be heat treated to impart an index change without spontaneously crystallizing the adjacent, unexposed regions. This would enable spatially defined index modification in the same optical element, with good (sub-100 nm) spatial resolution. These important findings obtained on films allowed us to realize that phase separation would provide an important role in controlling the spatially-induced compositional variation that served as a pre-cursor for localized crystallization for amorphous films. While not identical in morphology to what we observe in as-melted bulk glasses (as-deposited GAP-Se films are homogeneous and not phase separated), it guided the present effort carried out in this dissertation.

As the bulk glass for this composition was already phase separated when melted, it was unknown whether nucleation of this material was possible with laser irradiation [105]. Following a discussion of how the induced refractive index is characterized, we show how this understanding obtained on GAP-Se films was used to induce spatially varying refractive index modification in the bulk glasses of interest to this study.
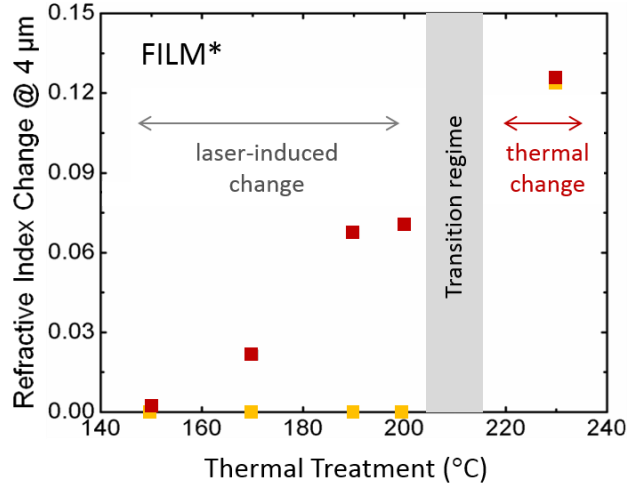
Figure 1-10 The refractive index for 40 mol% PbSe GAP-Se films for a growth only furnace HT (yellow) and laser nucleated plus furnace growth (red) plotted for the different thermal growth tempeatures used. Defined are the regions whereby only the laser-induced region grow with heat treatment (30 mins) at the shown temperatures (red samples below the transition regime) as compared to the regime where both the laser exposed glass and the unexposed glass both crystallizes. Above the transition regime, spatially varying crystallization is no longer controllable, as it is accompanied by spontaneous crystallization.

1.8 Quantification of refractive index modification and GRIN characterization

Traditional absolute refractive index measurements are most commonly performed

using spectroscopic ellipsometry [106,107], minimum deviation [108], and prism

coupling refractometry [109-114]. Most of these approaches involve near-surface

interaction of a probe beam with a sample and the corresponding modification of some

aspect of that beam following the interaction. Hence as a starting point, these methods are

useful in probing the surface refractive index and its changes, but do not all lend

themselves to good quantification of volume index changes. Spectroscopic ellipsometry

uses measured reflection and/or transmission data of a sample, and then fits the data to a

model to extract the refractive index. This measurement technique typically has a spot

size of approximately one cm, and is able to generate the entire dispersion curve for a

sample with one measurement. One issue with this technique is that the material model used for the samples must be correct, which can cause error in the absolute refractive index if the model does not sufficiently describe the system used. [106,107]

The minimum deviation technique uses a precisely manufactured prism of the material of interest to measure the refracted angle of a laser with a particular measurement wavelength going through the prism. The prism can then be rotated in order to determine the input angle with the minimum deviation of the refracted beam which can be used to directly solve for the refractive index. This technique can make highly precise measurements with error in the 5th decimal place, and measures the index over several mm throughout the bulk. The downside of this technique is that one must create a highly precise prism of the material that one wants measured. [108]

The prism coupling technique has the sample with an unknown refractive index in contact with a prism of known refractive index. The combination of prism and sample is then rotated to find the angle where total internal reflection occurs at the interface of the two materials. This technique measures the index over a spatial region of 1-2 mm along the surface, and only a few microns deep through the evanescent coupling of the light at the interface. As long as the refractive index of the prism used is well known and the alignment of the incoming beam is precise, the error of the measurement can be 0.0005 RIU in the IR. [109-114]

These traditional techniques to measure refractive indices take the measurement over regions of mm-cm widths, and as noted earlier, typically only measure the surface's index. In order to be able to characterize GRIN materials, more spatially selective measurement techniques need to be used. Some main categories of spatial refractive

index measurements are interferometers [53,115], optical coherence tomography [116-118], image and system analysis [64,66,69,71], and effective media calculations [62]. Interferometric measurements measure an average phase change throughout the entire thickness of a sample measured. This can be useful to determine the wavefront shaping that would/can occur if a laser beam passes through the optic or an index modification along a single axis, but cannot give information about the spatial variation in 3D. If an optic were sliced into thin sheets (or if there is only a 1D or 2D GRIN), this technique could be combined with an absolute refractive index measurement at the surface of the sample with a technique such as prism coupling to know the absolute refractive index profile of the sample.

Optical coherence tomography (OCT), a common imaging modality in biology, has recently gained application with characterization of polymer stacked GRIN materials. This characterization technique uses back reflections off of the boundary interfaces from the different refractive index layers. Using OCT with confocal scanning, both the thickness and refractive index of the layers can be measured and mapped spatially. Additionally by scanning over an arc, these measurements have been able to be used on post pressed and formed samples. This near final or final shape diagnostic is very useful to determine if there are any defects in an optic, where the defect is within the part's thickness, and what the defect is due to. This technique is very useful to be able to obtain the absolute, spatial refractive index profile, but needs the interfaces between layers of different indices for back reflections and therefore cannot be used on all GRIN profiles. This also is not used for IR transparent materials as of yet. [116-118]

System and image analysis measurements involve determining the effect the optic has on the light traveling through it, and is useful to determine if the designed optic can be used in a specific system. Specific techniques include imaging analysis [64], system performance characterization [66], and wavefront sensing [71]. Imaging analysis uses the analysis of an image going through an optic to see what the resolution is and if any distortions are occurring. This technique generally uses an image standard such as a USAF test chart or an image of a known diffraction grating [64]. System performance analysis generally places the optic in a pre-existing system and verifies whether the deigned optic is able to replace elements that were previously there in order to show that the functionality of the GRIN performs the way it was designed [66]. Wavefront sensing measures how the optical wavefront changes after passing through an optic [71]. This allows one to quantitatively say that the expected wavefront exited the optic as was expected. These techniques are good at determining if an optic works, but does not fundamentally give spatial information about the index profile in the material, only the total effects the optic has on the light.

Effective media calculations utilize characterization techniques that give information about the ratio of different material types that are present and solves for the effective refractive index by utilizing an effective media equation and know refractive indices of the materials present. One indirect technique illustrating this approach as applied to polymeric GRIN materials utilizes µ-FTIR measurements in a polymer system. µ-FTIR was measured at various locations across the surface of the sample. By knowing the spectra for each polymer type used in the material, the relative amount of each type present at the measurement location was able to be determined. Since the refractive

indices of these polymers are well known, the effective refractive index at that location could be calculated. With a combination of cutting and polishing, the refractive index of the entire GRIN profile could be mapped out. The effective media technique can be highly precise, but is dependent on how accurately the volume fraction of each phase present is measured and the validity of the equation used for that particular multi-phase system. [62]

1.9   Goals of this work

The above sections highlight the key background, concepts and prior work related to the goals of this dissertation. In order to develop infrared transparent glass ceramic GRIN optics, new materials need to be developed and characterized as to their potential refractive index variation realized upon ceramization. The magnitude of the potential refractive index change possible must be studied and evaluated to determine how controllable the process is, and how repeatable it is based on the use of exploratory, small volume glass melts. Once it is determined that the material can produce changes in index upon ceramization, our motivation has been to fabricate actual GRIN structures which validate the material chemistry and physics assumptions we believe responsible for the index modification and assist us in understanding limitations. Such limitations not only include limitations to optical function, but more specifically the compositional space possible for exploitation of glass stability and subsequent partial conversion to glass ceramic, starting material quality, thermal processing protocol optimization, and availability of reliable metrology tools which can be used to quantify the outcome of the processing protocol. In order to spatially be able to measure the GRIN structure, new techniques need to be developed for this material to measure the refractive index

spatially. These steps form the basis of the present effort. A short summary of target

material attributes that frame our study are shown in Table 1-3. While not exhaustive, it

defines the key understanding we need to have of candidate infrared GRIN material and

the processes we will use to convert it to a glass ceramic suitable for potential use.

Table 1-3 Target material attributes of a MWIR transparent GRIN glass ceramic envisioned in this effort

Property	Attribute	Metric
Infrared transmission	Transmission within spectral window of use (defined for this study to be 3-12μm)	Low intrinsic absorption and scatter of base glass
		Low absorption of precipitated crystalline phase(s) (maintain 90% maximum transmission)
		Knowledge and control of crystal growth rate
	Transmission within the spectral range of laser writing sources	Definition of wavelength paired to mechanism desired: use of heat accumulation (fs), bandgap irradiation (CW) or use in the transmission regime (ns)
Glass homogeneity	Refractive index uniformity	Better than 10^{-3} to enable a change (Δn) to be measurable and to maintain high image quality
Glass crystallization behavior	Nucleation and growth rate behavior	I-U curve
Glass/glass ceramic optical quality	Index and dispersion behavior over wavelength regime of use of pre- and post-processed part; thermo-optic coefficient	Refractive index, n, dn/dλ, dn/dT
Metrology	Refractive Index	Quantifiable by Raman spectroscopy
Manufacturability	Post-processed glass ceramic can be fabricated into optical component shape using existing methods and tools	Mechanical hardness, toughness and chemical durability
	Resulting glass ceramic amenable to AR coating	Thermal stability under coating conditions

In this work, materials in the GeSe$_2$-As$_2$Se-PbSe system have been investigated for their ability to have index changes upon ceramization. Material selection has been carried out based on as-melted, bulk material attributes. Base material and post-processed (nucleated and grown) glass ceramics have been evaluated for changes associated with the glass chemistry, structure and physical properties accompanying the conversion of glass network constituents to a crystalline form. The resulting changes in optical properties, most notably transmission and refractive index, are measure and correlated with the mechanism(s) believed responsible for the change. Once formed, the optical composite's transmission has been measured to ensure that the resultant material is still applicable for use in optical systems.

Reported in the subsequent chapters are steps used to address the wanted material metrics listed in Table 1-3. Further investigation has been performed on a specific composition to be able to determine the controllability of the crystallization and to develop an indirect method to be able to determine the refractive index in a spatially selective way. Chapter 2 summarizes the sample fabrication and characterization techniques used in subsequent chapters. Following this, Chapter 3 highlights the choice of base glass compositions within the GAP-Se system and the protocols used to identify suitable furnace-based thermal processes for the creation of a glass ceramic. Chapter 4 extends these findings and reports on efforts to utilize laser irradiation to assist in the nucleation and/or growth of the secondary nanocrystalline phase with the goal of demonstrating spatial variation within a monolithic bulk part. Multiple laser exposure regime are discussed and a summary of the tradeoff of each is presented. Chapter 5 presents a novel and not previously demonstrated approach to create an index gradient

based on the destruction rather than the creation of the secondary crystallization phase(s) through the use of laser-induced vitrification. The potentials and limitations of this approach are presented for the first time, based upon infrared transparent glass ceramics. Lastly, chapter 6 reports demonstration of optical functionality realized based on the key findings of the prior material science and laser-material interaction studies. Here, a GRIN structure was created to verify that this material is able to produce GRIN structures. These structures were accomplished through laser-induced heating of a sub-bandgap or a bandgap laser. These structures were characterized for their optical functionalities, and confirmation of one of the structures was accomplished by creating a structural correlation with crystallization, and therefore index of the material.

2 EXPERIMENTAL

A brief overview of the experimental tools, methods, and techniques used in subsequent chapters are described for the rest of the work presented in this document. The sample preparation and fabrication methodologies, as well as material characterization and measurement protocols are included.

2.1 Glass melting

Bulk glasses were prepared using a standard melt/quench protocol for 40, 350, and 400 g melts to evaluate the role of melt size on starting material properties and their impact on conversion to a glass ceramic suitable for GRIN applications. Elemental starting materials, 99.999% (5N) pure were weighed and batched in a nitrogen atmosphere. They were then loaded into fused quartz tubes and sealed under vacuum in an ampule. Small (40 g) melts were prepared in 10 mm diameter tubes, whereas larger melts were prepared in 30 mm diameter tubes. Once sealed, the ampule was placed in a rocking furnace which was ramped at 2°C/min up to a melting temperature of 850°C and was left overnight while rocking. The sample was then cooled at 2°C per minute to a quench temperature of 650°C. The rocking was then stopped and the sealed ampule was removed from the furnace and quenched with forced air. The sample, while still in the ampule, was then annealed at 177°C for 2 hrs, and slowly cooled to room temperature.

2.2 Sample fabrication

After annealing, the glass rods were removed from the ampules and sliced into ~2 mm-thick disks using a Buehler Isomet low-speed saw, and were then ground by hand

with a Buehler EcoMet 250 Grinder-Polisher with grits of 320 and 600 to near flatness. Plano coupons were then either polished with a PR Hoffman double-sided lapping machine (PR-2) with a 5 μm alumina slurry or by hand using polishing pads with grits of 800 and 1200. The final polish was performed by hand with a 0.05 μm alumina slurry, resulting in a typical post-polished root mean square (RMS) surface roughness (measured over about a square mm) of 18±6 nm. In some cases, additional quartering of large (30 mm diameter) samples was performed with the slow speed saw equipped with a diamond-impregnated blade. If required, post-HT polishing of parts was performed by hand, and the starting grit size used was determined by the amount of material that needed to be removed in order to return the glass' surface to a good level of flatness and a good optical surface quality that is void of scratches and digs.

2.3   X-ray diffraction (XRD)

X-ray diffraction (XRD) was performed to confirm the amorphous nature of the starting material and to assess post-processing conversion of the glass to a glass ceramic. XRD analysis was carried out on a PANalytical Empyrean, basic X-ray diffraction system with 1.8 KW, $\lambda_{CuK\alpha}=0.15418$ nm, and 40 mA beam current. The 2Θ scan range covered was 9.9933° to 70.15386°, with a step size of 0.050134°. This translates to a typical acquisition of 1200 points per spectrum. Measurements were taken on bulk polished samples that were suspended above the sample holder with clay at room temperature (RT). Signatures from the mounting clay and sample holder were removed from patterns. A calibration curve to assess unknown, post-heat treatment volume fractions was prepared as a reference. For this purpose a known volume fraction of crystal phase of the most prevalent, highest index crystal phase, PbSe, was intimately

mixed with amorphous, 0 and 40 mol% PbSe glasses and then evaluated to see if there was any X-ray shielding from the Pb in the material on the crystal signal. It was found that there was a negligible amount of shielding that occurs in these materials for the amounts of Pb already present in the glass and the amounts of crystal that are formed. Known (measured from mixing) versus measured volume fractions for these two melts are shown below in Figure 2-1 From these data, known peak heights could be compared to that found in unknown, post-processed glass ceramics. The XRD system exhibits ~0.10° - 0.15° instrumental broadening of the peaks.
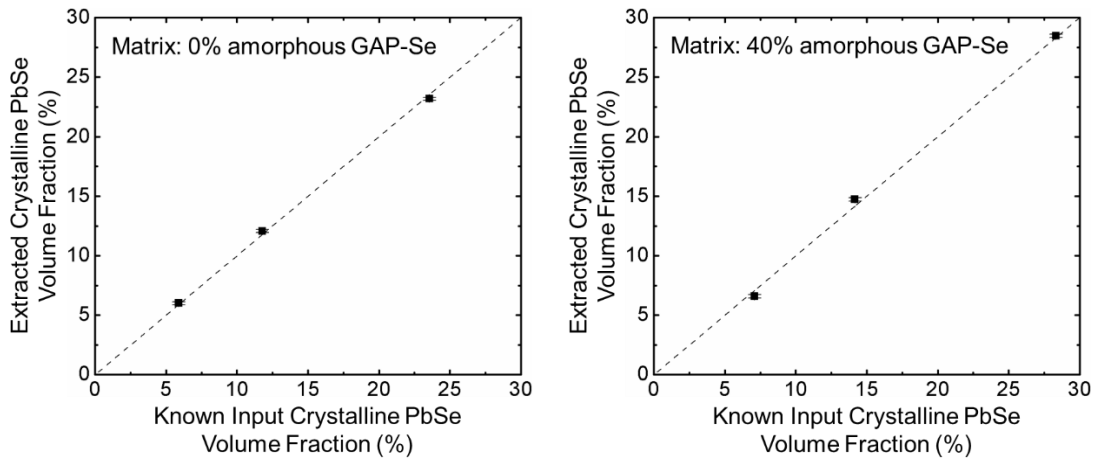
Figure 2-1 The known added amounts of crystalline PbSe is plotted against calculated amounts of PbSe using peak height data from measured XRD to see if there was X-ray shielding from the Pb in the surrounding glassy matrix. The dashed line is a 1:1 line, and error is contained within the size of the data points, unless shown.

2.4 Transmission electron microscopy (TEM)

A FEI Tecnai transmission electron microscope (TEM) was used to measure the size of precipitated crystals in the material for samples with crystal sizes less than 100 nm and was measured in the range of 80 – 200 kV. The spatial resolution of this system is 0.2 nm. Samples were ground into a powder, mixed with acetone, applied to a lacey carbon grid, and the solvent was evaporated leaving behind the sample power on the grid.

48

Images were analyzed to determine the average size of the crystalline particles visible. SAED was used with this system in order to obtain crystallographic information in order to identify precipitated crystals and has the same spatial resolution as the TEM. X-ray electron diffraction spectroscopy (XEDS) was also able to be performed with this system in order to obtain information on the composition of the material spatially in order to see changes in the composition of the two glassy phases present. This part of the system has a spatial resolution of 0.14 nm (when used at 80 kV) and a spectral resolution of 50 to 80 eV.

2.5   Scanning electron microscopy (SEM)

In order to measure the size of precipitated crystals for samples with crystal sizes greater than 100 nm where TEM was not necessary/required, a scanning electron microscope (SEM) was used. A Zeiss ULTRA-55 FEG SEM was used to measure treated bulk samples, which has 1nm resolution for the measurement voltage of 15kV that was used. Samples had carbon tape applied to them in order to reduce charge build-up. Images were analyzed to determine the average size of the crystalline particles visible. Additionally energy dispersive X-ray spectroscopy (EDS) was also performed with this machine to verify the total composition of base material with a spectral resolution of 50 to 80 eV.

2.6   Raman spectroscopy

Raman spectroscopy was measured with a Bruker Senterra microRaman system at room temperature, with a 785 nm excitation wavelength. An objective lens of 20x was used in conjunction with the setting of 1 mW of power and a total integration time of 2.25

min, using three co-additions of 45 sec each. The spot size of the beam with the objective used was measured using the knife edge technique. From this, the beam waist was determined to be approximately 2 μm. In order to confirm that the Raman measurement was not inducing any additional changes in the material, multiple measurements were taken at one location and no change in signal was observed. Measurements were taken on bulk, polished samples. If the sample surface was deformed after a HT, a light polish as discussed in section 2.2, was performed before a measurement was taken. Wavenumber error is ~2 cm^{-1} for the system.

2.7   UV-VIS/FTIR measurements

To cover the entire transmission range needed for these samples, both a CARY 500 UV-VIS spectrophotometer and a ThermoFisher Nicolet iS5 FTIR were used to quantify the base glass and post-processed glass ceramic's transmission, which includes contributions from absorption as well as scatter loss. These two instruments combined, cover the spectral range of 0.2-25 µm, with 0.9-15 µm being of interest to this study. The system was corrected for a baseline measurement, where the system is calibrated for 100% transmission with no sample in the aperture. Samples were attached to a ~2 mm circular aperture with double-sided tape, and the aperture with the sample attached was then placed into the spectrophotometer for the measurement. The FTIR used the same protocol, except that it used a 4 mm aperture.

From these data, the optical bandedge or scattering tail, depending on the samples morphology and/or microstructure, was measured for both the shortwave and longwave edge of the transmission window. As the true optical bandgap is difficult to accurately determine as one cannot accurately extract the bandedge from a Tauc plot for bulk

50

samples (thicknesses >10's of μm) [119] and the material itself does not have a periodic lattice structure, the short wave cut-off (SWCO) used for this study is defined as the wavelength where 90 % of the maximum transmission is observed. The transmission was not corrected for Fresnel loss or sample thickness in this study, as this correction only affects the maximum transmission and does not cause a wavelength shift in the relative value of the 90% mark. This transmission cut-off takes into account not only optical absorption, but transmission loss due to scatter as well from either phase separation or crystallization.

2.8 Refractive index measurements

Refractive index measurements were performed to assess the refractive index, dispersion, and dn/dT of the material in its base glass and glass ceramic forms. These measurements were performed using a Metricon 2010M system that was modified for use in the IR and is further described in [113,114]. As a brief overview of how the measurement works, a prism with a known refractive index is put into optical contact with a sample of unknown refractive index by the use of a pneumatic piston as shown in Figure 2-2. This mounting ensures intimate contact between the part and the prism and is suitable for use on bulk and thin film samples. The mounted sample/prism combination is then rotated on a rotation stage from an angle above the critical angle of total internal refraction to below it. This gives rise to a curve that is flat (the signal from the sample/prism interface is directly coupled into the detector), and then has an exponential decay in intensity, starting at the critical angle (part of the light is transmitted through the sample instead of reflecting). From knowing the angle at which this drop starts, the angle

of the reference prism, and the prism's known refractive index, the refractive index of the unknown sample can be determined.
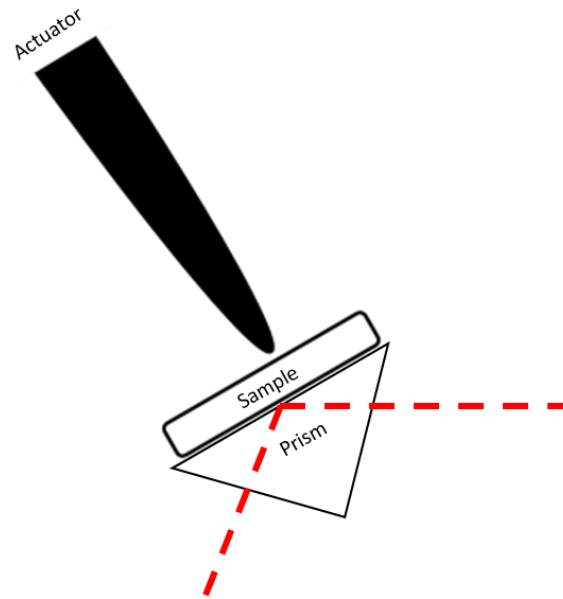
Figure 2-2 Schematic illustrating how the planar polished bulk glass/glass-ceramic sample is held against the prism using a pneumatic actuator with the dashed red line representing the laser beam path where one side is the laser source and the other side is the detector. Modified from [114].

In order to make this measurement, a sample must have two parallel faces, with at least one of them being optically flat, ideally having parallelism within 100 arc min and a surface roughness less than 50 nm RMS on both sides. If the sample possesses too much wedge it can slip out from the piston and damage the prism. These parallel faces need to be greater than 10 mm in length in at least one direction, 4 mm in the other, and no larger than 30 mm in either direction. These limitations are largely due to the ability to securely load and unload the sample, as well as make sure the sample is not too large, and therefore heavy, and potentially be able to slip out of the system. The thickness needs to be at least 1.5 mm, but below 3 mm. If the sample is too thin it could crack due to the

pneumatic actuators load, but if it is too thick it cannot fit into the system. Sample handling is easiest if the sample is approximately 10x10x2 mm.

Several modifications of the system and measurement technique have occurred since it was originally constructed and described in [113]. System modifications include the addition of three IR lasers to extend the spectral range of the system, the addition of new VIS/NIR sources, and additional prisms to broaden the refractive index range available to measurement of the (typically) high refractive index materials being examined. In the present effort base or post-heat treatment materials typically had refractive indices in the IR ranging from 2.9 to 3.5 which necessitates the use of multiple prisms. Additional sources in the IR were added including two distributed feedback laser quantum cascade laser diodes (QCL) (QD5250CM1 and QD7950CM1), which were purchased from Thorlabs, and were placed inside of C-tab laser mounts (LDMC20) and were controlled with an ITC4005QCL. These two lasers have wavelength ranges of 5.245-5.258 μm and 7.958-7.978 μm, respectively. An Access L4G CO_2 laser was also added, which has wavelength tuning from 9.24-10.717 μm, and is fan cooled. As these three additional sources are CW, and as the mercury cadmium tellurite detector needs a pulsed input source, a chopper wheel (MC2000 Optical Chopper with a 60 slot wheel) operating at 5KHz was added into the system. A schematic of the system highlighting all the IR lasers is shown in Figure 2-33, and a list of all wavelengths available are in Table 2-1.
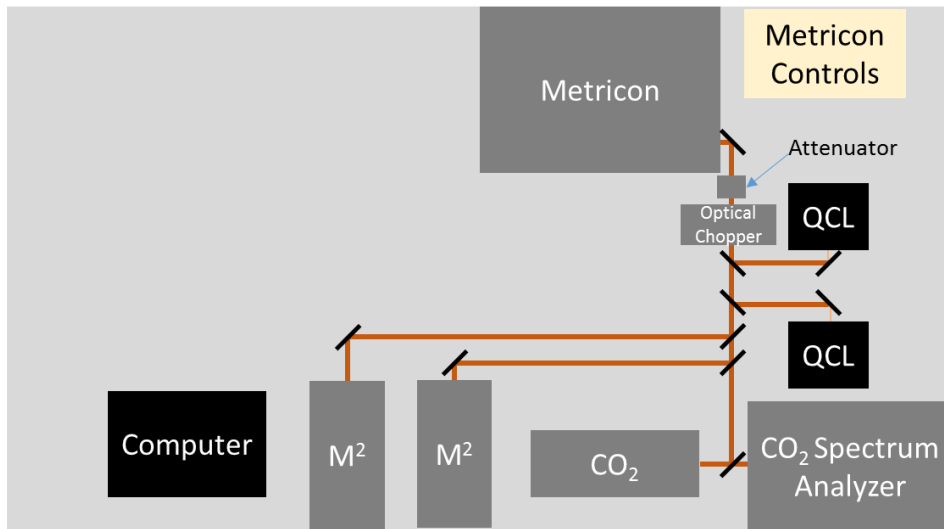
Figure 2-3 A schematic of the layout of the prism coupling system within the GPCL at UCF. The different IR lasers are shown, as well as the optional chopper (CW sources) and attenuator (higher power sources). The mirrors on the common beam path (vertical path on the right) are flip mirrors so that different laser sources can go into the system.

Table 2-1 The different laser sources for the prism coupler at UCF are shown, as well as their operating capabilities.

Type	Wavelength Range	Manufacturer	Model	CW/Pulsed	Typical index error
OPO	3.246-4.617 μm	M Squared	Firefly-IR-LP-B-BB-I	Pulsed	0.0005
OPO	1.485-1.885, 2.444-3.756 μm	M Squared	Firefly-IR-LP-A-BB-SI	Pulsed	0.0005
QCL	5.245-5.258 μm	Thorlabs	QD5250CM1	CW	0.001
QCL	7.958-7.978 μm	Thorlabs	QD7950CM1	CW	0.001
CO2	9-12 μm	Access	L4G	CW	0.0015
diode	635 nm	Thorlabs	CPS635S	CW	0.0005
diode	850 nm	Thorlabs	CPS850S	CW	0.0005
diode	980 nm	Thorlabs	CPS980S	CW	0.0005

Three visible lasers have been added to the system for use in determining certain material's broadband dispersion. In order to use these sources, the HeNe laser that is currently used by the system to angularly align itself must be removed. The laser diode is then fitted inside of an adapter and placed into the holder normally used by the HeNe. The beam must then be checked for alignment in case of a slight angular deviation from

the HeNe. The MCT detector and integrating sphere must also be removed, and are replaced by the Si detector that originally came with the Metricon system and the wires connected to the lock-in amplifier after the MCT detector must be detached and attached to the Si detector. Once this is performed, the system can be operated as normal.

Along with new lasers, additional prisms have also been acquired and their index ranges are shown in Figure 2-44. The GaP prism has an index range that overlaps the ZnSe index, and therefore can be calibrated the same way that the Ge prism is as described in [114]. The Si prism is not able to overlap this index range, but does partially overlap the range that the Ge prism can measure. This allows for cross-calibration with a sample that has its index measured by the Ge prism. Generally, this is performed with a sample in the index range of 2.95-3.04, and the sample is measured on the Ge prism the same day that it is used to calibrate the Si prism.
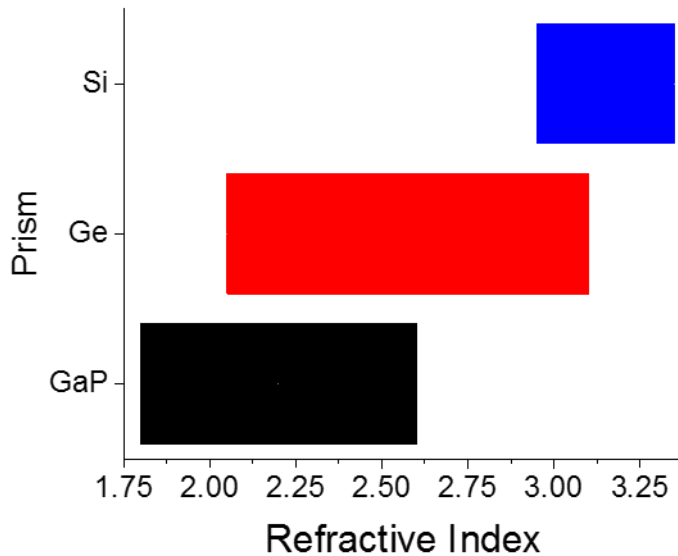
Figure 2-4 The approximate refractive index ranges for the prisms available in the prism coupler at UCF. The exact ranges vary depending on the temperature and wavelength used.

Calibration of the reference wavelength and reference material refractive index is carried out to ensure that no drift in experimental system has occurred. This includes measurement of a ZnSe reference to reference the prism index and an IRG24 ($Ge_{10}As_{40}Se_{50}$) glass witness sample to ensure that there are not significant measurement deviations from day to day.

One major modification in the measurement technique that was used in [113,114] is the definition used for determining the position of the "knee" or the drop in intensity that signals the onset of total internal reflection. In [113,114] the knee was determined by eye as to where the start in the drop of intensity begins. This technique leads to a shift in refractive index measurements between users measuring the same sample. In order to have multiple users be able to measure the same index for the same sample, the 4-point intersection option in the software of the system was used. For this option, the user defines four locations, two before the knee and two after the knee, where the first pair makes a straight line in the data before the knee and the second pair makes a straight line in the data after the knee as seen in Figure 2-5. The computer then solves for the intersection of these two lines and uses that location as the knee. Another added benefit besides repeatability across users is that this method allows one to make more accurate measurements on samples with low or noisy "knees".
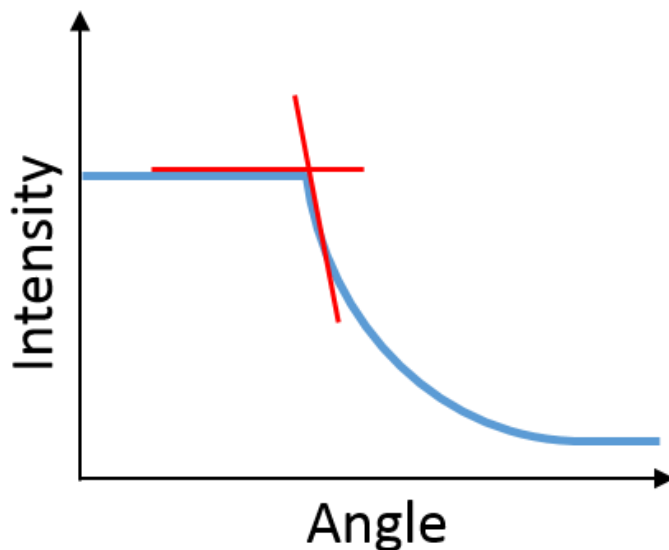
Figure 2-5 A representation of output data from the Metricon system illustrating the "knee", where a decrease in the signal occurs at the onset of total internal reflection. The strait part just before the knee and just after are used to define four points that the system then uses to calculate the intersection of the two lines formed by them. The intersection of these two lines is then used by the system to determine the refractive index.

The other change that was made in the measurement method is the calibration of the prism every day. This was done in order to correct for slight misalignments from day to day and to determine if there are long-time fluctuations of the measurements of the prism index. This has been performed for measurements taken over the past ~2 years. The difference between the average of the index measured over all time and the index measured on a given day for 4.515 μm for both the prism and a reference sample (also measured each time a measurement is taken) are plotted in Figure 2-6. Some slight long term fluctuations can be seen in the data, but overall the standard deviation for the prisms is more than that of the reference samples, which means this calibration technique does improve the measurement accuracy of the prism. The average standard deviation of calibration samples measured using a GaP prism across all the wavelengths and temperatures was found to be 0.0005 RIU, and the standard deviation of a reference used

with this prism was 0.0004 RIU. For the Ge samples the prism exhibited 0.0008 RIU

variation (standard deviation) and the reference was 0.0004 RIU. For the Si prism the

prism was 0.0011 RIU and the reference was 0.0005 RIU.
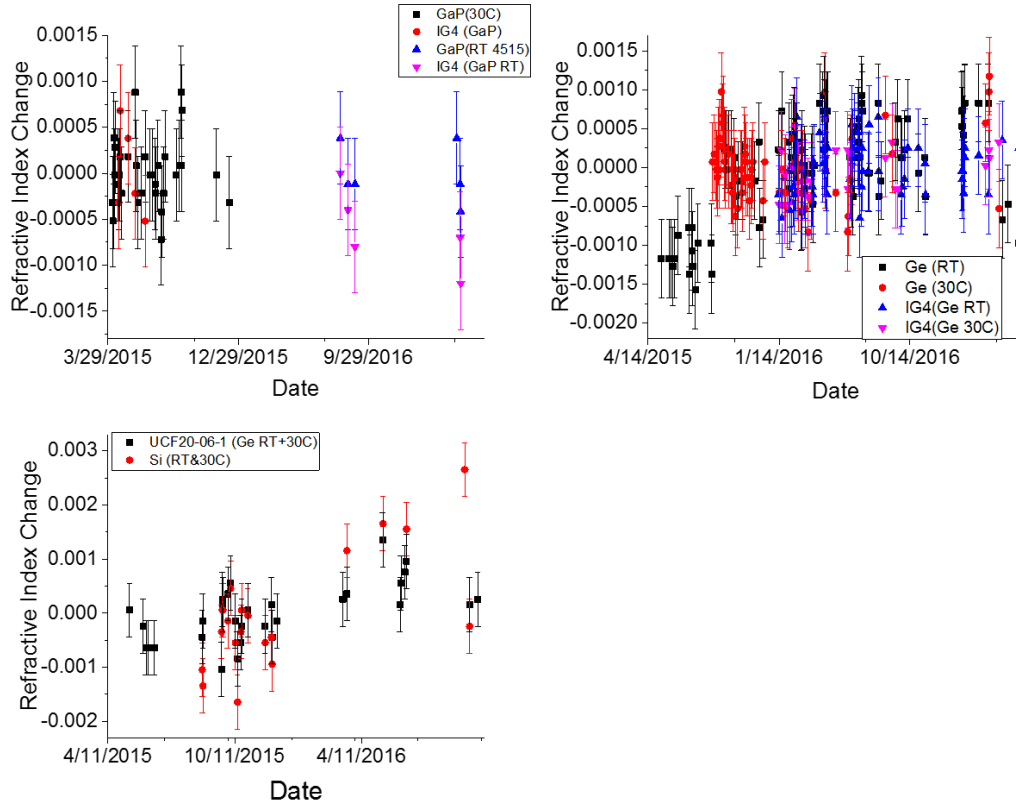
Figure 2-6 The relative change over time as defined as the difference between the measurement on a single day minus the average measurement for all times measured for GaP (A), Ge (B), and Si (C) for the prism and a standard reference (IG4 for GaP and Ge, and a 40 mol% PbSe sample for Si).

In order to measure the dispersion of candidate base glass and post-process glass

ceramics, measurements were taken across the infrared spectral region at wavelengths of

1.88, 3.3, 4.515, 7.968, 9.294, and 10.717 µm. These measurements were then used to fit

a 2-term Sellmeier equation. The dispersion measurements of the system were tested with

reference standards which are overlaid in Figure 2-7 below. There is good agreement

with literature values, though there tends to be higher deviations at longer wavelengths,

as these sources have a larger measurement error which appears to be intrinsic to the measurement system and has greater effect further into the IR. This error is not time-dependent, so it is not a problem with stability, but is still repeatable and can be slightly adjusted by adjusting the detector. This adjustment of the detector does not manifest changes in the spectrum at the lower wavelengths, and is worse at longer wavelengths. In order to calculate the MWIR Abbe# (υ_{MWIR}), the fitted Sellmeier was used to calculate the refractive index values at 3, 4, and 5 μm which were then used in Equation 8 to solve for υ_{MWIR}.

$$\upsilon = \frac{1 - \lambda_{4\mu m}}{\lambda_{3\mu m} - \lambda_{5\mu m}} \tag{8}$$
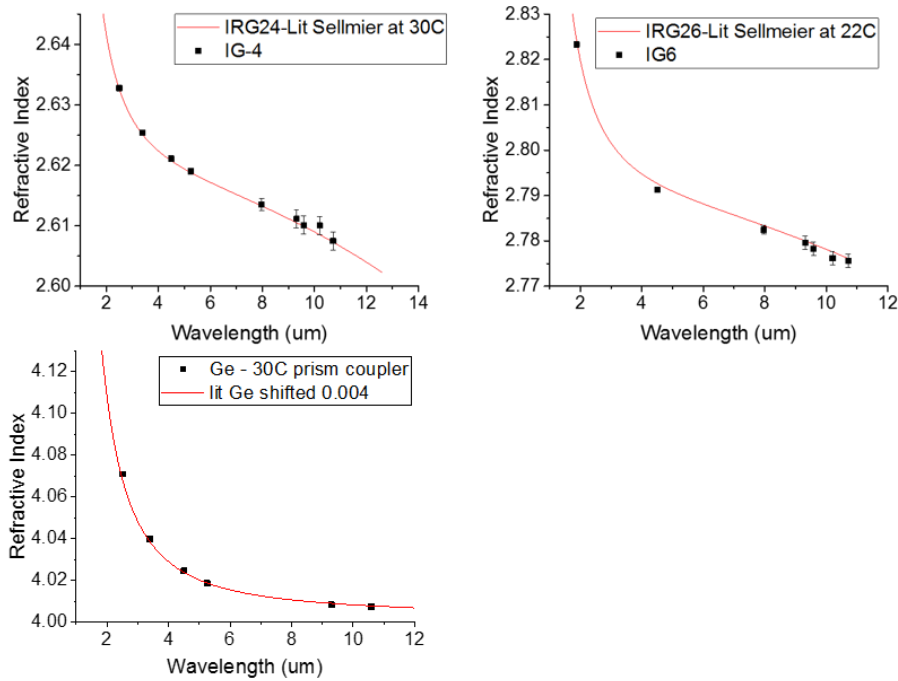
Figure 2-7 Index taken at 30°C, 10 scans per sample in one location. The measurements for wavelengths of 7.8-10.7 μm were taken at RT for IG6 and 6, and then corrected for temp using a dn/dT of 19.9E-6 for IG4 and none for IG6. Error is the standard deviation for multiple measurements of the same piece, and if not seen is within the data point. Using the known dn/dT of Si, the Sellmeier line was shifted ~0.0040 up from the literature RT value to 30°C and this was then used as our standard baseline.

The thermo-optic coefficient, change of refractive index with temperature or dn/dT, was measured at 4.515 µm at 30, 50, 70, and 90°C, measuring the sample from 30 to 90°C, and then back down from 90 to 30°C. This was done in order to ensure there was not any relaxation of the glass at 90°C that would alter the index upon cooling from the higher temperature [114]. A best-fit line of the data was used to calculate the dn/dT. The error for this calculation is generally 10 ppm as calculated in [114]. Additional characterization of dn/dT of commercially available ChG was used to cross-check the reliability of this protocol and is described in Appendix A. This commercial glass has its own published thermo-optic dn/dT values, measured with a commercial analysis method that does not employ an identical protocol [120] was used.

2.9   Density

Density of the parent glass and resulting glass ceramic was measured with an AE Adams PGW Balance using the Archimedes principle with an immersion fluid of deionized water at 22°C. By measuring the weight of the sample both in air and in water, the density can be calculated using Equation 9, where ρ_{water} is the density of water used, m_{sub} is the weight of the sample in water, and m_{dry} is the weight of the sample in air. Error for the sample sizes used in this study is on the order of 0.002-0.09g/cm^3.

$$\rho_{sample} = \frac{m_{dry}\rho_{water}}{m_{dry}-m_{sub}} \tag{9}$$

2.10   Thermal conductivity and heat capacity

Thermal conductivity and heat capacity were measured on a Thermtest TPS 2200 with two 30 mm diameter, 2 mm thick samples. It is expected that these thermal properties, which are important for both ceramization with a furnace as well as with a

laser, will vary as a function of glass composition. The two plano samples are

sandwiched around a probe and light force is applied to the stack to ensure good physical

contact between the surfaces. The probe then uses conductive heating to heat the samples.

It then measures the temperature decay, as it permeates into the volume of the sample.

The system calculates the thermal conductivity of the sample and the heat capacity per

unit volume. This can then be converted into specific heat capacity by dividing by the

density of the material. The system is able to carry out the measurements at different

temperatures in order to determine the temperature dependence of these properties. Error

for the sample material and size used in this study was on the order of 0.002-0.004

W/(m•K) for the thermal conductivity and 0.002-0.03 J/(g•K) for the heat capacity.

Where the reported error is the standard deviation of 5 measurements on the same

sample.

2.11   Coefficient of thermal expansion

The CTE was measured with a TA Instruments TMA 2940 thermo-mechanical

analyzer on a 15 x 2 x 2 mm rod. This measurement tracks the change in length of the rod

while the sample is slowly heated at a rate of 3°C/min, which is the standard operating

procedure for ChG. The linear coefficient of thermal expansion can then be solved by

determining the change of length in the rod with respect to its initial length ($\Delta L/L$) over

the temperature range used prior to Tg, and is shown in Equation 10 below where α is the

CTE, L is the length, ΔL is the total change in length for a given temperature change and

ΔT is the temperature change. Measurements are made from room temperature to

nominally 90% of the value of the glass' transition temperature (T_g). Temperature error in

the system is ~2°C.

$$\alpha = \frac{1}{L}\frac{\Delta L}{\Delta T} \tag{10}$$

2.12 White light interferometry

White light interferometry (WLI) was performed with a Zygo New View model 8300 to measure surface profiles of different samples for either surface roughness, flatness or post processed topography. This system uses interferometry to measure the phase shift that occurs from the path length change from different heights of the sample, and is able to measure surface height variations on the sub-micron scale, while the resolution of features in the X-Y plane is dependent on the objective lens used. Large area measurements were performed by stitching multiple measurements together through the software on the instrument to determine changes in surface topography across a modified region. A minimum overlap of 15% was used in this process. Surface RMS values were performed by taking measurements at multiple locations and then averaging the values together. By taking the RMS of several individual locations instead of over an entire stitched region, the RMS roughness is isolated from any overall tilt or wedge of the larger surface profile. The surface topography repeatability of the system is listed as 0.12 nm.

2.13 Thermal modeling

Simulations of laser-induced heating were performed with COMSOL Multiphysics using the Heat Transfer in Solids module, following methodology described in [121]. The geometry of the simulated sample was either a disk or a quarter of a disk in order to match the simulations with the experimental conditions used. The disk geometry utilized an axially symmetric model to cut down on computational time and was a disk that was 2

mm thick with a 15 mm radius. For the quarter disk a 3D geometry was used, and a quarter of a 15 mm radius disk that was 2 mm thick was created.

The material inputs needed for the modeling include values for sample density, thermal conductivity, and heat capacity. The input data used were from measurements performed on materials prepared in our labs using the sample attributes and measurement protocols of samples used in the study. The boundary conditions used for the sample were Heat Flux on all the outer boundaries and were set to convective heat flux. The inputs for this boundary condition were the external temperature and a heat transfer coefficient. The external temperature was set to the experimental temperature conditions that would be used while the irradiation was occurring from either a heat cell or a furnace. This external temperature was also set as the starting temperature for the sample. The heat transfer coefficient is not a well-defined parameter for most materials, and values between 0 and 100 W/(m^2•K) have been used, so a value of 50 W/(m^2•K) was used in these simulations.

The heat source for the sample was set to either a surface or volumetric heat source based on the absorption value for the wavelength and intensity of the laser used [122]. Equation 11 shows the surface heat equation used, where P is the power of the laser, R is the reflection coefficient, w_0 is the beam waist, and r is the spatial parameter for the axially symmetric model. A reflection coefficient of 0.26 was used for both of the wavelengths used and was assumed to not change with temperature.

$$Q_{in} = P(1 - R)\left(\frac{2}{w_0^2}\right)e^{-\left(\frac{2r^2}{w_0^2}\right)}$$
(11)

This equation was approximated for a volumetric source by adding an exponential decay term with the absorption coefficient of the material at that wavelength. This regime

was also a pulsed regime, so a Gaussian exponential was also added in the time domain for the pulse duration used. Additionally for the quarter slice a linear shift in the heat equation was applied in order to center it on the sample, and a circular step function was added in order to clip the edges of the beam to account for the aperture used in the experiment.

LiveLink for Matlab was utilized for running batch simulations that varied material parameters for the CW study. For each combination of parameters used in the simulations a new model was created that still retained the same geometry and physics. This was performed instead of a parameter sweep as there were multiple parameters that were swept, and it ensured that each parameter change was implemented correctly. The temperature for each time step at the center of the irradiation and the edge of the sample were saved for each combination of parameters used. This data could then be imported back into Matlab to determine how the different parameters affected the maximum temperature reached in the sample and the variation in temperature from the center of the sample to the edge.

2.14   Laser facilities used

A Spectra-Physics Millennia VS laser emitting at 532 nm (CW) was used for some irradiations. The collimated output beam diameter of this laser is ~2 mm, with average powers up to 5 W. The beam was expanded to larger beam diameters using a telescope comprised of two plano-convex lenses with focal lengths of 250 and 750 mm. The lenses were placed slightly out of focus from each other to achieve multiple beam waists that were still close to collimation at the location of where the irradiations would be occurring. Fluencies and intensities used can be found in Table 2-2.

A Lee Laser LEP-Y6TQ/30 laser was used for some irradiations. This system generates 20 ns pulses at a RR of 10 Hz at a wavelength of 1064 nm and an average power of 1.8 W (post aperture). The beam waist was expanded with a telescope lens to ~3 cm. This beam then went through an aperture of 11.5 mm. The resultant output from this system is a nearly flat-top profile. Simulations of this laser used an added aperture to the Gaussian beam to account for the beam not having a true flat-top profile. Fluencies and intensities used can be found in Table 2-2.

A 110 fs pulse duration, 1.3 μm source was made up of a Kapteyn Murnane Laboratories (KML) TS Ti:sapphire laser pumped by a Spectra-Physics Millennia VS to seed a Spectra-Physics Spitfire femtosecond laser system. The Spitfire is a regenerative amplifier pumped with a Spectra-Physics Empower laser. The Spitfire output then went through a Coherent OPERA optical parametric amplifier (OPA) and the signal output was utilized. The output wavelength was checked with an Ocean Optics NIR256-2.5 spectrometer to ensure the correct wavelength was chosen. The beam was then focused with a 25 mm-lens, and was used in conjunction with a Newport Universal controller (ESP300) and 3D stage for structured irradiations. Fluencies and intensities used can be found in Table 2-2.

A 1030 nm, 350 fs pulse duration Amplitude Satsuma fiber laser system was also used for irradiations. This output of this system was then guided through a 5x lens, and an Aerotech A3200 3D air stage was used to translate the sample in all three directions. A Si camera was used in order to ensure that the laser was focused on the sample surface and to ensure that the sample was perpendicular to the laser direction. Fluencies and intensities used can be found in Table 2-2.

Table 2-2 Laser parameters used in this study.

Source	λ (µm)	Average Power (W)	Beam diameter (cm)	Pulse duration	Repetition rate	Intensity (W/cm^2)	Fluence (J/cm^2)
Millennia	0.532	0.89-2.448	1-1.2	N/A	N/A	0.57-1.08	N/A
Lee-Laser	1.064	1.8	1.15 (quasi-flat-top)	20ns	10 Hz	0.43	0.043
KML/ Spitfire/ OPERA	1.3	0.046	0.01-0.043	110fs	1 kHz	18-365	0.018-0.365
Amplitude Satsuma	1.03	0.0128	0.003-0.004	350 ns	1 MHz	1324-2876	1.323-2.876

3 DEVELOPMENT OF INFRARED GLASS CERAMICS

This chapter reviews the physical and optical properties of the starting base glass and the evolution of property changes upon thermally induced nucleation and growth. Glasses in the $(GeSe_2\text{-}3As_2Se_3)_{1-x}PbSe_x$ tie-line were created and evaluated for their ability to ceramize and form glass ceramics. Compositions were evaluated from x=0 to 40 in increments of 5. These compositions had their pre- and post-structural and optical properties measured including XRD, refractive index, and transmission in order to determine the effect of crystal growth on the resulting composite. One composition, 40 mol% PbSe, was further investigated as it had promising characteristics for use in MWIR GRIN optics. The effect of different nucleation and growth conditions on this composition were studied in order to determine how they affected the post-HT properties including XRD, refractive index, transmission, and Raman Spectroscopy. Raman spectroscopy was also evaluated to see if it could give information about the refractive index of the material post-ceramization in order to have a more spatially selective method of index measurement to be able to evaluate any potential GRIN structures.

3.1 Pb-series HT experiments – towards glass ceramics

In order to create IR glass ceramic GRIN elements, new glass compositions were developed and their ability to form glass ceramics needed to be investigated. These glasses needed to be created, have their base material and optical properties measured, and then their post-HT optical and material properties measured in order to detect any changes upon HT. This section overviews the experimental methods needed for this effort.

Bulk glasses with compositions of $(GeSe_2\text{-}3As_2Se_3)_{1-x}PbSe_x$ with x=0 to 40 in increments of 5 were created in 40g batches in 10 mm inner diameter quartz tubes using melt/quench methods described in section 2.1. After batching and annealing, the rods were fabricated into slices. These were then ground and polished with the double-sided lapping machine and final hand polish described in section 2.2. Four samples of each composition were fabricated and characterized for their base glass properties including XRD, refractive index, and transmission. Mie scattering calculations were also performed in order to see if the LLPS could be seen to be the dominating factor for the SWCO of the transmission. Three of these samples were subsequently HT with a nucleation (N) HT, and then had their properties re-measured including the transmission and refractive index. These three then had a growth (G) HT performed, and their properties were re-measured including XRD, refractive index, and transmission. Simulations of the SWCO were performed with Mie scattering theory in order to confirm that the SWCO is from induced scattering from crystal growth in the material. The details of these calculations and the determination of the quantities used in them can be found in section 2.14.

Heat treatments were performed in a ThermoScientific 48000 muffle furnace in air atmosphere. The temperature of the furnace was verified with a K-type thermocouple that was left inside the furnace during the HT and was in contact with the refractory brick shelf that samples were placed on. The three samples of each composition were HT at the same time, and were placed on the refractory brick around the thermocouple.

In order to determine what N and G HT temperatures should be used, the I-U curves for the 20 and 40 mol% PbSe, compiled in [39], were evaluated and are shown in Figure 1-6. These two compositions showed that there is likely an increase in the needed

nucleation and growth temperatures with a decrease in the amount of PbSe in the sample. In order to systematically determine which temperature values should be used, yet still likely remain within either the nucleation-only or growth-only regime of each composition, the N temperature was set to the glass transition temperature of each composition and the G temperature was set to the peak of the first crystallization peak as determined by DSC for each composition. The N temperature is seen to be on the lower end of the nucleation region, but would remain below any potential growth in the material. The G temperature was set to be far into the crystallization regime in order to create a maximum potential amount of growth in the material, and therefore the maximum amount of change possible in the material properties upon ceramization. The N step was performed for one hour, and the G step was performed for 30 min for all samples.

XRD was performed on one base (no HT) and one N+G sample for each composition using the protocol described in section 2.3. The measurement on the base sample was to ensure that no crystallites had formed upon quenching of the melt. The measurement of the N+G sample was to determine if, and what kind of crystal phases formed upon HT. Crystal phases that were previously identified in [39] for 20 and 40 mol% PbSe samples using SAED were considered in the analysis of the XRD patterns. Volume fractions for each crystal phase present were determined based off of the intensity of their respective peaks, with no needed correction factor for shielding from the Pb in the remaining glassy matrix as described in section 2.3. This was then used to calculate an effective refractive index for the glass using the equation in section 1.5 above, where the index of each

crystal type is the known refractive index from literature [123-125] and the measured volume fraction of each phase was determined by XRD.

Refractive index measurements were performed using the prism coupler described in section 2.8. Refractive index measurements were performed at 30°C on the four base samples, the three N samples, and the three N+G samples at a wavelength of 4.515µm for all of the compositions. The reported value was the average of all the measurements of each composition, and the error is the standard deviation of them. For the base samples one measurement was taken per sample, and for the HT samples the index was measured on both the top and the bottom of each sample. Dispersion was calculated on 0, 10, 20, 30, and 40 mol% PbSe for the base and N+G samples using the technique described in section 2.8. The mid-wave dispersion, as quantified by the Abbe number of the glass, was also calculated using 3, 4, and 5µm as the input wavelengths as described in section 2.82.8. The thermo-optic (dn/dT) measurements were performed at 4.515µm on 20 and 40 mol% PbSe samples using the technique described in section 2.8.

The transmission spectra for the base, N, and N+G samples were measured using the techniques and equipment described in section 2.7 to measure the whole spectral range of 1-25µm. The SWCO was tracked to see the effect of induced scattering from crystal growth that could limit applications of the material in NIR applications. The LWIR bandedge, long wave cut-off (LWCO), was tracked to see if there was any change from induced absorption from any crystallite species that might grow. The SWCO/LWCO used here was 90% of the maximum transmission measured, which is described more in detail in section 2.7.

In order to confirm that any induced scatter was from the crystal growth, the size of the induced crystals were measured with either a TEM or SEM depending on the resolution needed for the 10, 20, 30, and 40 mol% PbSe HT samples, and is described in more detail in sections 2.4 and 2.5.

From the crystal sizes measured with TEM/SEM and their volume fractions measured through XRD, the short-wave band edge of the glass ceramic could be modeled and compared to the measured FTIR. These simulations were performed using Mie scattering theory with an extinction coefficient calculated for the induced crystals, and is described further in section 2.14. With these tools defined, they will be applied to the base and HT material in order to determine the changes induced from furnace-induced ceramization.

3.2 Pb-series base glass properties

The characterization of the base glasses were first measured in order to confirm that the base glass was indeed amorphous, and to determine the baseline for any material property changes realized post-HT. The samples had their XRD, refractive index, dispersion, dn/dT, and transmission measured. As discussed and shown in the 'target attribute' table shown at the end of chapter 1, any resulting glass ceramics suitable for use as an optical component should, post-HT, maintain its transparency through the MWIR and have a change in the refractive index greater than 0.02, but more ideally closer to 0.1. Again, the sign of this Δn in the case of this study employing Pb-crystallites as a candidate precipitating phase would likely be positive.

The starting base glass, as discussed in 2.1, has morphological variation in the form of LLPS across the composition space used in this study. The transition from a region of homogeneous glass to phase separated glass occurs at approximately 10 mol% PbSe, the

71

transition of a Pb-rich droplet phase to a region exhibiting spinodal decomposition occurs around 25 mol% PbSe, the transition from spinodal to a Pb-deficient droplet phase occurs around 35 mol% PbSe with the glass returning to a homogeneous, non-phase separated morphology beyond approximately 45 mol% PbSe. These transitions of morphology clearly impact transitions in physical properties as reported in detail, in [40]. Additionally, as will be shown in this study, such morphology changes, specifically the Pb-content associated with the respective phases, as will be shown to indeed influence the type and size of forming crystalline phases in the post-heat treated, glass ceramics.

The base glass XRD confirmed that the starting material was X-ray amorphous, and therefore any crystal growth observed in our glass ceramic could be attributed to the HT itself. The parent glass' XRD pattern for the 40 mol% PbSe showed two amorphous humps that did not change significantly with changes in the composition.

The measured base glass' refractive index for this series of glasses is plotted in Figure 3-1. Measure refractive index at a wavelength of 4.515µm versus mol% PbSe is shown and a systematic increase in refractive index as can be seen that tracks with an increase in the amount of Pb in the glass. This is likely due to the increase in the highly polarizable Pb atoms in the matrix, and does not appear to be affected by the change in the morphology (whether the Pb is in the droplets or matrix) of the glass. This finding could be due to the probe beam of the index measurement (2-3 mm) averaging over a large enough region of the glass that it averages over both glassy phases in the phase separated medium.
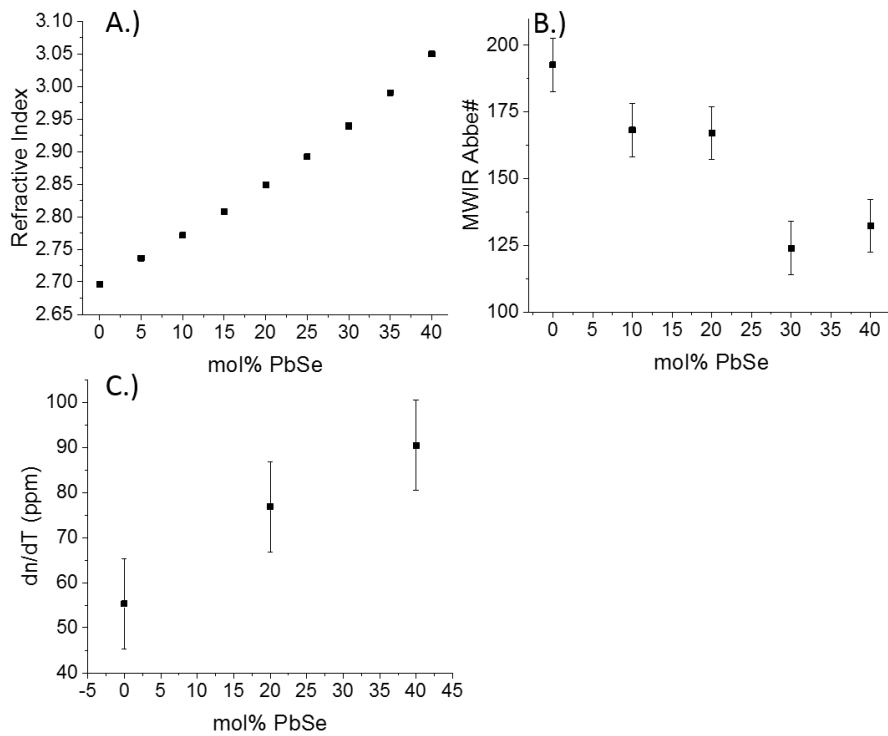
Figure 3-1 The refractive index (A), MWIR Abbe# calculated using refractive index values at 3, 4, and 5μm (B), and dn/dT calculated using index measurements at 30, 50, 70, and 90°C are shown versus composition for the base glass. Modified from [41]

As shown in Figure 3-1 B, the MWIR Abbe number for both the base and grown material appears to have a minimum point around 30 mol% PbSe, which is where microscopic analysis of glass morphology shows that spinodal decomposition occurs. This region of spinodal decomposition has the smallest change in composition between the two glassy phases present in the material. This small change in composition of the two phases means that the material lacks a significantly Pb-poor phase. As the dispersion is higher in the compositions with a significantly Pb-poor phase, and the composition without a Pb-poor phase has the lowest dispersion, a higher concentration of Pb in the material could cause a lower dispersion. Reciprocally, as the Pb-rich phase has a decrease in the amount of As, it could be that the region of higher As is what causes the increase in

the dispersion, as commercially available IRG26 ($As_{40}Se_{60}$) is more dispersive than IRG24 ($Ge_{10}As_{40}Se_{50}$) or IRG22 ($Ge_{33}As_{12}Se_{55}$) [114].

The change in refractive index with temperature, dn/dT, was measured for the three base glasses of interest, and is plotted in Figure 3-1. An increase is seen in the base glass as the mol% of PbSe is increased. If one can assume that the two glassy phases are similar in structure to Ge-As-Se glasses where the Pb-atoms act similarly to highly coordinate Ge atoms, (they can both exhibit 4-fold coordination), then the trend observed here is consistent with that observed in [114] for additions of a 4-fold coordinated species. In this prior studies, glasses with As-Se ratios near 1:2 with Ge addition exhibited an increase in the dn/dT also.

Infrared spectroscopy (FTIR spectra) of the base glasses are shown in Figure 3-4, and shows the transmission of the base glasses through the infrared as well as the scatter tail for several of the compositions that had transmission edges far enough into the IR for the Nicolet to be able to measure them. Noted on the spectra is the multi-phonon edge (the LWCO) that is indicative to the materials used. SWCO as defined in section 2.7 was calculated for each glass and is shown in Figure 3-4. From the refractive index data one would expect to see a steady increase in this SWCO if there was no scatter in it, which is only evident at low and high mol% Pb-values, and with an increase in the middle amounts of PbSe. This increase in the SWCO is from induced scatter from the LLPS in the glass. The peak of this region is around 25 mol% PbSe, which is where the glass transitions into spinodal decomposition and has larger phase separated regions. The bandgap decreases again as the Pb-rich phase starts to become the majority phase around 30 mol% PbSe.

The base glass was able to be characterized for its XRD, refractive index, dispersion, thermo-optic coefficient, and its transmission spectra. The XRD was able to determine that the base glass was indeed amorphous and therefore any subsequent crystallization will be from any HTs that were performed. The refractive index showed a nearly linear dependence on the Pb-content in the material at $\lambda=4.515\mu m$, the dispersion showed a minimum around 30mol% PbSe, and the thermo-optic coefficient showed an increase with the amount of Pb in the glass. The SWCO of the transmission was seen to be dominated by scatter losses through the middle amounts of PbSe due to the increased phase separation size in this composition space. Now that the base glass properties have been determined, the post-HT properties can be evaluated in order to determine the effect of the composition on the resulting composite material.

3.3 Pb-series glass-ceramic characterization

As noted previously, the goal of this effort aims to utilize the base glasses discussed above to prepare composite glass ceramic materials where the extent of crystallization results in a variable refractive index as well as other physical properties. Hence, XRD was used as an important tool to quantify the modification made to the base glass upon heat treatment. The HT XRD showed crystalline growth for compositions above 5 mol% PbSe, and the calculated volume fractions of each phase present are seen in Figure 3-2 and in Table 3-1. As the 5 mol% PbSe composition is not phase separated, there likely was not a high enough concentration of Pb in the glass to sufficiently decrease the glass stability for crystallization to occur.

75
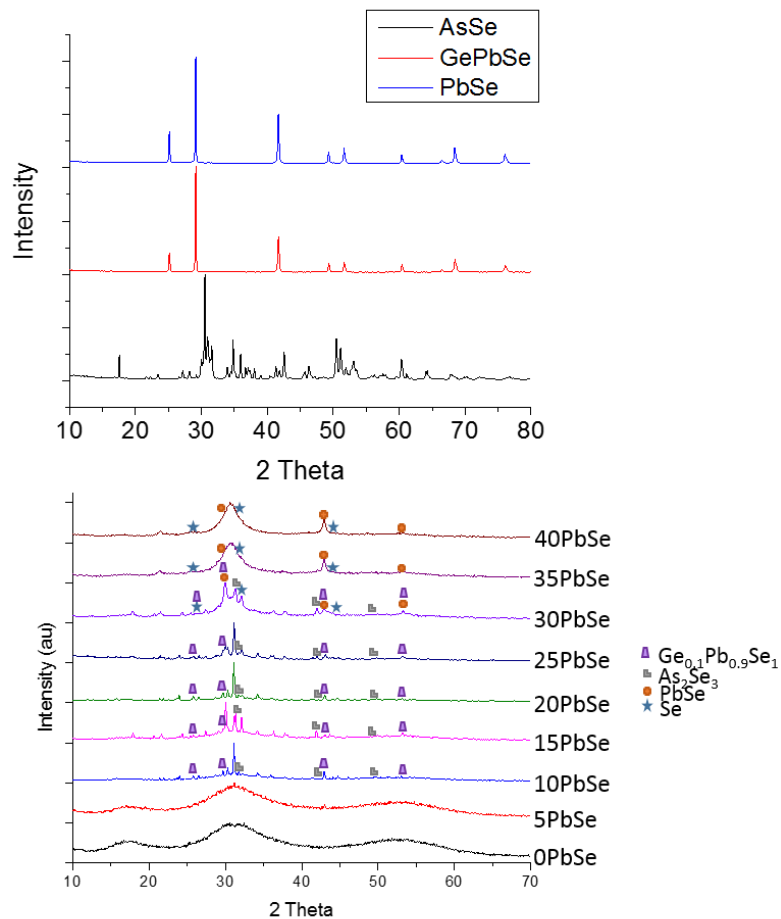
Figure 3-2 XRD of the crystallographic phases that were identified in the glass ceramics are shown on the top. XRD of the two-step HT (N+G) samples for the compositional series for PbSe content of 5-40 mol% PbSe are shown on the bottom. The $x = 0$ mol% PbSe pattern was added as a reference for the base glass, Pb-free GeAsSe network as it was not subjected to HT since it did not exhibit crystallization features (T_x) in the DSC. Crystal phase identities for peaks shown are indicated. [41]

In the XRD patterns for 10 to 30 mol% PbSe many crystal peaks are visible and each pattern is unique. The observed crystal phases in these compositions are As_2Se_3 and $Ge_{0.1}Pb_{0.9}Se_1$, and their volume fractions and respective ratios present in the material are seen in Table 3-1. $Ge_{0.1}Pb_{0.9}Se_1$ is able to exist as an independent crystal phase, with a unique XRD pattern and lattice parameter for SAED identification. These volume fractions were extracted from the XRD pattern using the method described in section 2.3.

76

This change in the pattern is likely due to the change in the ratio of $Ge_{0.1}Pb_{0.9}Se_1$ to As_2Se_3 throughout this compositional space. As the amount of Pb in the melt increases the amount of $Ge_{0.1}Pb_{0.9}Se_1$ that is formed also increases. This is likely due to the higher amount of Pb present in the droplet phase causing more of the Pb-rich phase to crystallize. The change in the ratio of the two crystal phases is likely due to the large changes in the composition in the Pb-rich droplets with changes in the mol% of PbSe added into the glass. At 30 mol% PbSe, where spinodal decomposition starts to occur, transitions are seen in the crystal phases that form and the amorphous background starts to be visible in the XRD pattern. The observed crystal patterns for these compositions are PbSe, Se, and As_2Se_3, and their relative fractions are also seen in Table 3-1. For the 35 and 40 mol% PbSe samples a similar pattern is observed with nearly identical ratios of precipitated crystal types, with only a change in the total amount of crystallization seen. As the compositions below 35 mol% PbSe have the minority phase that is Pb-rich, small changes in the amount of PbSe added into the melt has a large effect on the Pb-concentration in this phase as seen in [39,40], which affected the ratios of the crystal types that formed. On the other hand, 35 and 40mol% PbSe have a Pb-rich majority (matrix) phase, where small additions of PbSe into the melt has a much smaller effect on the Pb concentration in the Pb-rich phase, causing little change in the ratios of the crystal phases that formed. This means that the concentration of Pb in the individual glassy phases of the LLPS has a large impact on the final crystal phases formed upon HT, even for crystal phases that do not directly contain Pb in them.

The identification of the crystal phases present and their respective volume fractions (total crystal compared to the remaining glass, as well as relative fractions of each phase

type) were then used to estimate the refractive index for each composition of the N+G

material, which are plotted in Figure 3-3. The total volume fraction of crystals observed

by XRD is shown in the last column of Table 3-1, where there is a relatively constant

volume fraction through 30mol% PbSe, and then there is a jump for both the 35 and

40mol% PbSe. This could be due to the major phase being Pb-rich and therefore there is

a greater volume of glass that is able to crystallize.

Table 3-1 The volume fraction (V_f) of each crystal type as determined by XRD is listed for the different compositions (mol% PbSe) glasses. Additionally the total V_f of crystals present was calculated. [41]

Mol % PbSe	V_f $Ge_{0.1}Pb_{0.9}Se$	V_f As_2Se_3	V_f PbSe	V_f Se	Total V_f	% of crystal type ($Ge_{0.1}Pb_{0.9}Se$: As_2Se_3:PbSe:Se)			
0	0	0	0	0	0	0	0	0	0
5	0	0	0	0	0	0	0	0	0
10	0.0326	0.1682	0	0	0.2008	16	84	0	0
15	0.0422	0.1235	0	0	0.1657	25	75	0	0
20	0.0544	0.1336	0	0	0.1880	29	71	0	0
25	0.0576	0.1131	0	0	0.1706	34	66	0	0
30	0	0.1168	0.0594	0.0292	0.2053	0	57	29	14
35	0	0.1346	0.0952	0.0337	0.2635	0	51	36	13
40	0	0.1407	0.1045	0.0352	0.2804	0	50	37	13

After determining the crystal phases and volume fractions that were formed, the

refractive index was measured in order to see if the changes in the refractive index were

due to crystallization in the glass. Upon nucleation there was a negative change in the

refractive index of all the compositions, with a greater change observed with lower

amounts of PbSe. Along with the base glass, the refractive index of the nucleated glass

does not appear to be affected by the change in the glass morphology across

compositions. Since no crystallization is observed after nucleation, this drop in index is

likely due to relaxation in the glass. It has been noted in other studies that a drop in index

can occur in the Ge-As-Se ternary upon a sub-T_g HT, where the lower As-containing glasses have a greater drop [114]. If these glasses behave similarly, the lower Pb-containing glasses have a larger amount of As, and could therefore be slightly less of a 3D-structure which would allow them to have a greater change in their refractive index.

Upon crystallization there are again three regimes of property variation, as was previously observed with the XRD, in the optical property trends shown as a function of PbSe content. These regions are again delineated by color to depict and correspond with the regions of transition in morphology discussed previously. Below 10 mol% PbSe there again is no observed change from the nucleation state after growth, as no crystallization occurred as evident by XRD. From 10-30 mol% PbSe there is relatively little change in the final refractive index, and an overall trend is not evident. The dip in the 15 mol% PbSe composition could be due to its unusually low volume fraction of crystal as compared to the other glasses. The exact cause of this is unknown, but there may have been an error in the HTs performed. Except for the 15 mol% PbSe sample, all these compositions had similar total volume fractions of crystals, with the As_2Se_3 staying relatively constant and a slight increase in the $Ge_{0.1}Pb_{0.9}Se_1$ as the amount of Pb was increased in the glass. At 30 mol% PbSe there is a change in the crystal types present, but the amount of PbSe crystal that formed was similar to the 25 mol% PbSe composition, and also additionally had Se crystals that formed which have a refractive index similar to As_2Se_3. For 35 and 40 mol% PbSe there is a larger increase in the refractive index that continues to increase with increasing Pb content, which is likely due to the increase in the volume fraction of crystals that formed in the glass, specifically the increase in the amount of the Pb-containing high index phase of PbSe.

The measured and calculated (using volume fractions from XRD) refractive indices of the N+G samples were compared to evaluate the quality of the different effective index approximations that were stated in section 1.5 in Equations 3-5. The different approximations were tested in order to determine which more closely matched the measured data. These data are plotted together in Figure 3-3, and the Gladstone-Dale calculations tracked the best with the measured data. There is a slight over-estimate of the refractive index though. This is possibly due to the refractive index of the base glass being set to the base glass refractive index, which neglects the change in index after the nucleation or any subsequent index change from a change in composition of the remaining glassy phase after crystallization. As the Gladstone-Dale approximation fit the data the best, it will be used in subsequent sections.
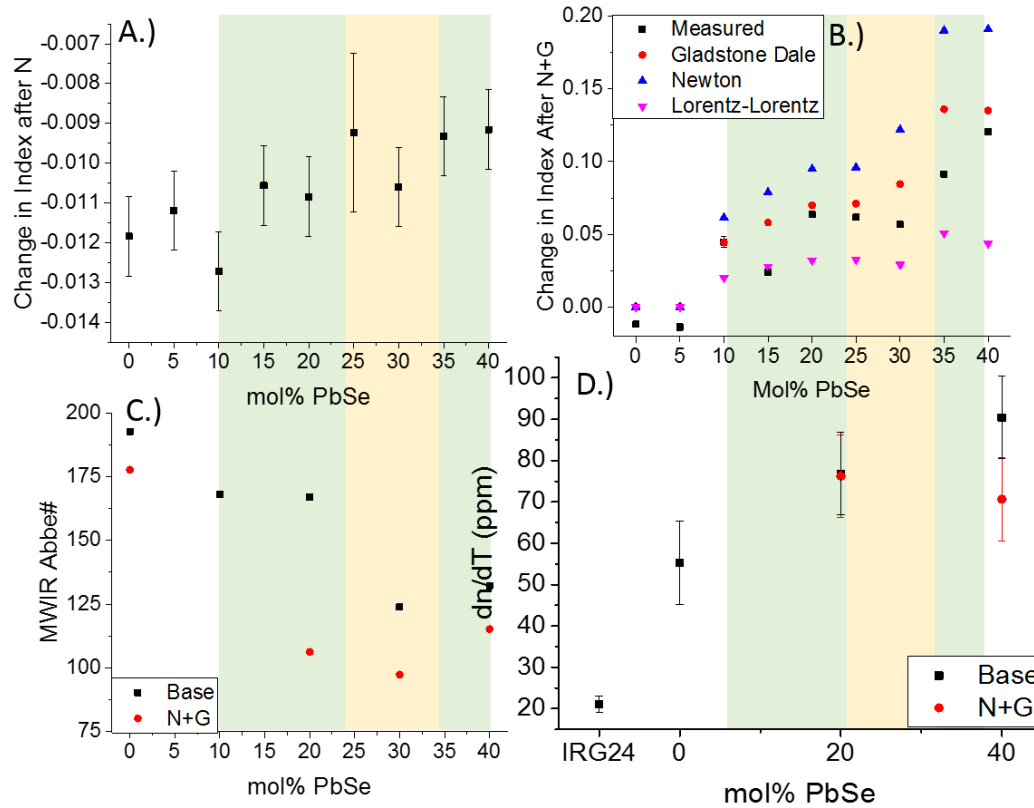
Figure 3-3 The measured refractive index of glass as a function of PbSe content following nucleation (A), and following nucleation and growth (B) as compared to the parent glass; shown for comparison is the refractive index as calculated from the type and volume fraction of crystal present as determined by XRD for three different effective index approximations. (C). The calculated MWIR Abbe# for base glasses and those following nucleation and growth are plotted for select compositions. (D) measured dn/dT for base and post-HT'd glass ceramics are shown, as well as for IRG24 (reference). The colored regions depict compositional regimes where transitions in morphology are observed. Modified from [41]

The MWIR Abbe# for both the base and grown material appears to have a minimum

around 30 mol% PbSe, where spinodal decomposition occurs. The similar shape of the

curve post-HT indicated that the driving factor for the shape is likely from the Pb-poor

phase in the glass as this phase is less effected post-ceramization. As there are no

significant absorption features that are seen in the transmission spectra post-HT, the

change in dispersion is likely not from induced absorption features in the glass.

Upon ceramization there is little change in the dn/dT of the 20 mol% PbSe, while the 40 mol% PbSe sees a decrease in the dn/dT. This decrease is likely due to the crystal phases having a lower dn/dT than the base glass (or the crystal phases formed in the 20 mol% PbSe glasses), causing the composite to have an overall decrease in the dn/dT. It could also be due to more of the Pb-containing crystal precipitating out of the glassy matrix in the 40% glass, and therefore causing the remaining glassy matrix to have a depleted (lower) Pb-content more similar to the 0 mol% PbSe composition.

After nucleation there is a negligible change in the SWCO, which would be expected as no crystallization was seen in the XRD. Additionally, this also indicates that the phase separation does not significantly change in size or composition after nucleation as the scattering did not change.
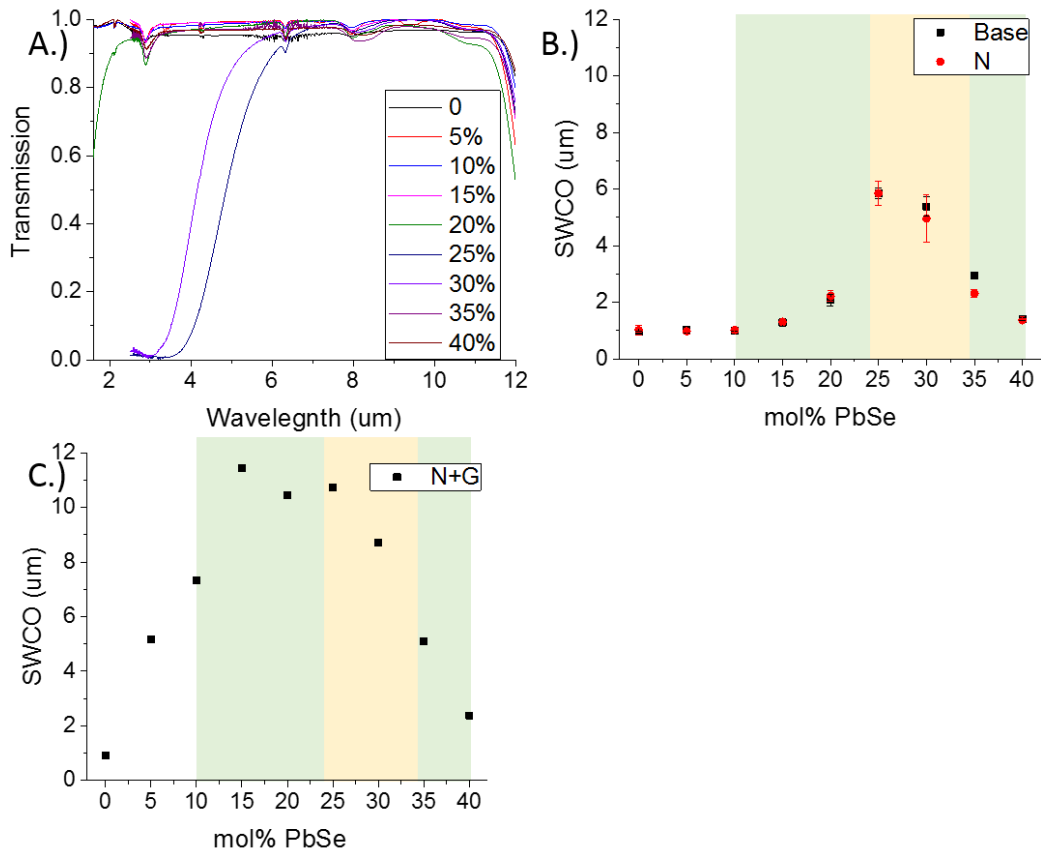
Figure 3-4 Representative transmission spectra of the base glass are plotted in (A) for all compositions. The SWCO (position of spectra in μm) for base and nucleated samples (B) and nucleated and grown (N+G) samples (C) are shown. The SWCO was defined as 90% of the maximum transmission measured. Spectra were not corrected for dispersion or thickness. [41]

After growth, there is a significant shift in the SWCO for all the compositions, and in

Figure 3-5 a representative sample is shown with their base and N+G transmission

spectra normalized to 1, and then the spectral range was cut-off at 13μm. As the amount

of PbSe increased up to 15mol% PbSe there is an increase in the scatter tail of the

material. A plateau is then seen from 15-25 mol% PbSe, and then there is a decrease after

25 mol%. The transition between 25 and 30 mol% PbSe is also the transition from

$Ge_{0.1}Pb_{0.9}Se_1$ to PbSe and Se, which could contribute to this change in the trend. What is

interesting is the large change in 5 mol% PbSe despite the lack of crystallization seen in

the XRD, or change in its refractive index.
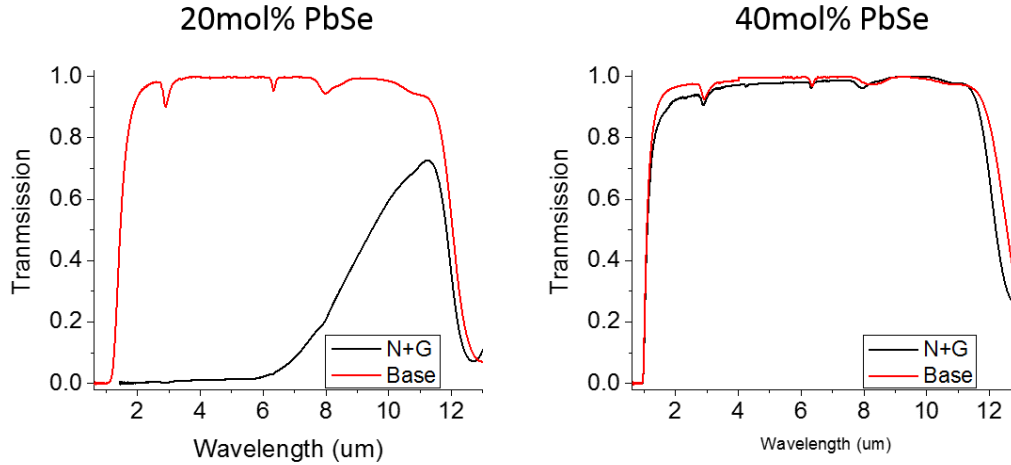
Figure 3-5 The transmission curves of the base (red) and the post-heat treated (N+G) samples (black) is shown for the 20 and 40 mol% PbSe samples. The maximum transmission point in the data was normalized to 1 and then was cut-off at 13μm. Modified from [41]

The LWCO did not shift significantly upon N or N+G as seen below in Figure 3-6,

which also depicts the entire transparency window of the glasses. 15-20 mol% PbSe can

be seen to be nearly opaque after the N+G, and then the glass ceramics become more

transparent at both high and low Pb concentrations. Some shift in the LWCO is seen for

10, 20, and 25 mol% PbSe, which is due to the large amount of scattering present in these

materials causing the scatter tail to start to affect the signal in the LWIR.
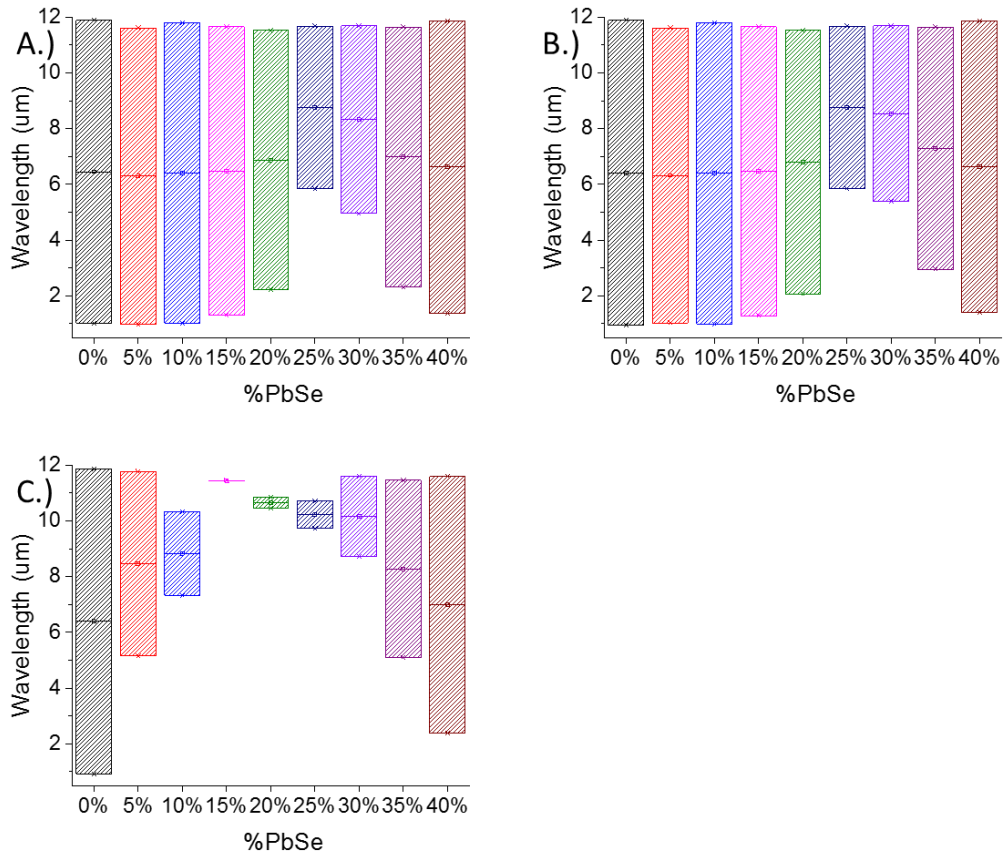
Figure 3-6 The full transmission window is plotted for base (A), nucleated (B), and N+G (C) samples as a function of PbSe content (mol%) The bar chart is meant to illustrate how the transmission window changes as a function of thermal treatment.

The size of the crystals precipitated was also investigated in order to determine if this was a dominating factor for the changes in transmission, as the total volume fraction of crystallite species determined by XRD does not trend with the SWCO. This means the number density of crystals is also likely changing, as both the size and number density contribute to the volume fraction present. SEM or TEM, depending on the crystal size, was used to measure the short and long axis of the crystals observed and is shown in Table 3-2. It was also noted that the crystal structures observed are agglomerates of the individual crystal types observed with XRD. In the 10 and 20 mol% PbSe, highly anisotropic crystals were observed. These large crystals are likely the reason for the large

shift in the SWCO. For the 30 and 40mol% PbSe samples, the crystals were still quite large, but were much more regularly shaped.

Through the HT of these GAP-Se glasses, glasses above 5 mol% PbSe were able to crystallize, and the ratios of formed crystals changed up to 35 mol% and then remained constant for the 40 mol% sample as seen in the XRD. This change in crystal type occurred as the microstructure tended towards a Pb-rich matrix, and the transition into the Pb-rich matrix also was where the crystal phases changed to different types. This also tracked well with the refractive index, which saw small changes in the refractive index for up to 30 mol% PbSe, and then a jump is seen for both the 35 and 40 mol% PbSe samples. The SWCO showed the largest change from 15-30 mol% PbSe. Below this point there was not much crystallization occurring, and above it the crystal type changes to one that is less scattering.

As was stated in 3.2, the ideal candidate for an IR glass ceramic GRIN material would have transparency maintained throughout the MWIR and LWIR, and have an index change of at least 0.02, but preferably closer to 0.1. From the materials discussed in this section, the 40mol% PbSe was able to best maintain the transparency while still having a change in the refractive index in the material, and also had the largest change in its refractive index post-HT.

3.4   40 mol% PbSe HT series experiment

The most promising composition based on the prior post-heat treatment property modification analysis, magnitude of the index change, and low scatter, was the 40 mol% PbSe composition. As shown, this composition had the most change in refractive index upon heat treatment, and still retained its transmission for use in the MWIR. Further

characterization was performed on this composition in order to investigate the nucleation and growth processes to see if they were controllable and could potentially be extended towards structures possessing spatial variation of these properties. Additionally, in order to develop a spatially selective way to be able to measure the refractive index of a GRIN structure of this material, Raman spectroscopy was investigated to see if it gave information on the crystallization state, and therefore the refractive index, of the material upon ceramization.

To extend our findings beyond small melts which could contain larger compositional variation within our 40 g melts, the melt size was scaled up to 400g batches in [39], and these larger batches were used for further characterization. This 400g batch was melted the same way as those in section 2.1, with the inner diameter of the tubes being 30mm instead of 10mm as used in the previous section. These boules were again cut into 2mm thick slices, and were ground and polished by hand as described in section 2.2.

The base glass properties for this glass were first measured and characterized in order to set a base line as compared to prior melt (40g) data and to assess any changes that would occur after the HT steps were performed. Thermal properties were measured for later use with laser-induced heating. Thermal conductivity and heat capacity were measured as described in section 2.10. These measurements were performed at 25, 50, 100, and 190°C in order to determine how the thermal properties evolved at higher temperatures. Density was measured using the technique described in section 2.9, with an immersion fluid of deionized water at 22°C. The coefficient of thermal expansion was measured with the technique described in section 2.11. As the heat capacity measurement requires the density of the material, and density cannot be measured at 190°C with the

techniques used in our lab, a correction to the density was made using the CTE. This correction utilized the thermal expansion curve of the material through 190°C, as this temperature was below any weight loss in the material. The correction is shown in Equation 12 for below the softening point. For temperatures above the softening point, a second term is added into the exponential. This effectively breaks up the temperature range in two, with each region having their respective linear CTE, as the CTE changes to a secondary value above the softening point of the glass.

$$\rho_2 = \frac{\rho_1}{e^{3*CTE*\left(T_f - T_i\right)}} \tag{12}$$

XRD was also measured on the base glass in order to ensure that it was amorphous using the technique described in section 2.3. Refractive index measurements were only performed at 4.515μm and 30°C using the prism coupling technique in section 2.8. The homogeneity of the index was measured for one slice of the melt. The sample was divided into a 5x5 grid, neglecting the corners due to the sample being round. A refractive index measurement was then taken inside each of these squares, which were approximately 6mm in size as seen in Figure 3-7.
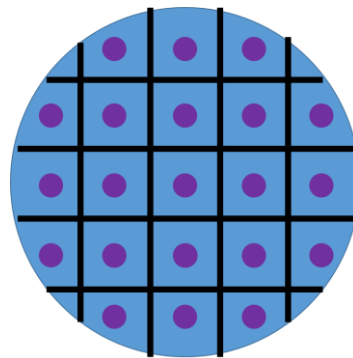
Figure 3-7 A diagram of the measurement points made for optical (refractive index) homogeneity on the base glass sample. The black lines are the grids where measurements were taken inside of, and are depicted as the purple dots. The actual measurements lay within the squares, but were usually not centered.

Transmission was also measured on the base glass in order to determine if there was any change from the small melts that were investigated in section 3.2. These measurements were made using the same techniques described in section 2.7 Raman spectroscopy was measured on the samples with the technique described in section 2.6.

HTs were performed with various nucleation and growth conditions in order to obtain different crystallization states to see the evolution of refractive index increase and to be able to determine how the structure, as measured by Raman spectroscopy, was changing. These HT were performed in the same furnace as the one described in section 3.1. The nucleation and growth temperatures were chosen based off of the IU curves in Figure 1-6. Three different nucleation conditions were used including no nucleation step, 190, and 200°C for 2 hours. These different nucleation HT were performed on separate slices, and were on the lower end of the nucleation curve in order to ensure that no growth would be occurring, as the growth-like curve shifts to lower temperatures upon nucleation [39,126]. These four slices were then quartered, and one quarter of each slice was then HT'd at a specific growth temperature. Four different growth HT temperatures were chosen, one for each of the quarters of the slices. The temperatures chosen for this HT were 200, 210, 220, and 230°C for 30 min. These temperatures cover from below the growth region of the material up into the start of the growth region of un-nucleated samples. Samples were lightly polished after HT if significant deformation was observed using the protocol described in section 2.2.

Post- heat treatment characterization was only performed on N+G samples. XRD was measured using the same equipment and parameters as described in section 2.3. The measured XRD patterns were used to validate whether crystallization occurred, and to

determine if the crystal phases that formed and their amounts varied with HT conditions. Additionally the intensities of the crystal peaks (corroborated with the calibration experiment) were again used as in section 3.3 to determine the volume fractions of the crystals present, which again were used to estimate the effective index of the material.

Refractive index was measured with the same conditions as were used on the base sample. This measured refractive index was then compared to the computed value from the XRD data in order to determine whether the index change was from crystallization occurring in the glass. The Raman spectra was also measured for the HT samples and used the same technique as was used on the base glass. Changes in the Raman spectra were then quantized for each HT condition. This change was then compared to the refractive index of the samples to be able to validate whether Raman measurements could be used as an indirect method to measure the refractive index of this glass ceramic by showing the structural changes seen in the Raman spectra were indeed from crystallization.

Apart from these measurements, transmission was also measured in order to determine if the transparency of the glass remained after ceramization, and if the different nucleation conditions effected the final glass transparency. These measurements were performed as described in section 2.7. Additionally the compilation of base glass properties are tabulated in a spec sheet in APPENDIX B. These data were then compared to the post-HT properties of the glass ceramic composite, as discussed in section 3.5. With these tools defined, they will be applied to HT material in order to evaluate the effect of the HT conditions on the formed crystalline phase(s).

3.5   40 mol% PbSe HT series: material characterization

The 40 mol% PbSe composition was further characterized for its ability to form a glass ceramic with different levels of ceramization. The HT material was characterized with XRD, refractive index, Raman spectroscopy, and transmission. Raman spectroscopy was also investigated for its ability to be able to predict the refractive index of samples with different amounts of ceramization. The base glass for the larger batch size used in these experiments was first characterized to make sure that the larger batch size did not significantly affect the material properties pre-HT, and therefore the post-HT crystal phases formed.

The base glass thermal properties needed for simulations are shown in Table 3-3 at different temperatures. The density was only measured at RT, but was corrected for by the coefficient of thermal expansion for higher temperatures using the TMA trace seen in Figure 3-8. The glass transition temperature as measured through this technique was 186°C. The linear coefficient for thermal expansion was calculated to be 19 ppm/°C below the glass transition range, and 46 ppm/°C above. As a reminder, Tg as determined by TMA is typically lower than that obtained by DSC due to the much larger sample size and inherent thermal lag (grams of glass as a glass rod in a TMA versus miligrams of glass powder in a DSC).
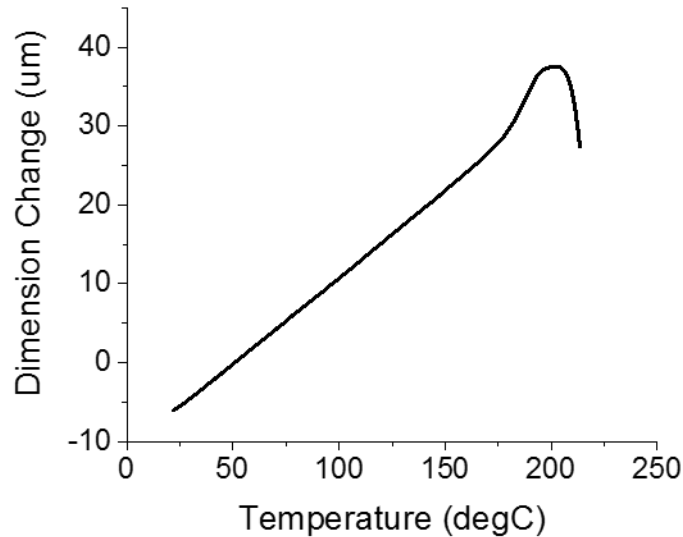
Figure 3-8 The output of the TMA showing the dimension change with temperature for a 40 mol% PbSe base glass sample and region of linear thermal expansion.

With an increase in the external temperature, an increase was seen in the thermal conductivity. Density on the other hand had a steady decrease, which would be expected from the knowledge that the sample expanded upon heating. The specific heat stayed relatively constant with an increase in the external temperature.

Table 3-2 The thermal properties of the base glass from just over room temperature to up to 190°C are shown. The density at temperature was calculated with a correction factor from the measure CTE. The error for the thermal conductivity and heat capacity are the standard deviation of 5 measurements. [39,126]

Temperature (°C)	k (W/(m•K))	C_P (J/g•K)	ρ (g/cm^3)
25	0.239 ± 0.003	0.229 ± 0.006	5.48
50	0.249 ± 0.002	0.228 ± 0.002	5.47
100	0.263 ± 0.002	0.238 ± 0.008	5.46
190	0.309 ± 0.004	0.232 ± 0.029	5.43

The XRD of the base glass exhibited two amorphous humps as seen in Figure 3-9, as was seen for the 40g batch in section 3.2, and again showed no signs of crystallization. The base glass refractive index homogeneity is shown in Figure 3-9, and the average

92

index was measured to be 3.0460 ± 0.0005, with the standard deviation of all the measurement locations found to be below the error of the measurement. The transmission curve is in Figure 3-9, and shows a SWCO slightly red-shifted from the 40g batch in section 3.2, but overall has a low scatter tail from the phase separation. This red-shift of the scatter tail would be expected based upon the slower cooling rate for the larger batch, which would be expected to be able to form larger phase separation.

The base glass Raman spectrum is seen in Figure 3-9, and exhibits a relatively sharp peak around 200 cm^{-1}, and a broad peak around 246 cm^{-1}. The first peak at 200 cm^{-1} can be associated with $GeSe_{4/2}$ units [40,114,127]. The second, broader peak is made up of several smaller ones including 225 and 240 cm^{-1} for $AsSe_{3/2}$ and 250 cm^{-1} for Se-Se [40,114,127]. The overall spectrum resembles that of Pb-free Ge-As-Se with As-Se values past stoichiometry of $As_{40}Se_{60}$ with additions of Ge, except that the $GeSe_{4/2}$ peak at 200cm^{-1} is slightly low [114,127]. Since Ge and Pb are both 4-fold coordinated, these two elements could be interchanged for each other. As the Pb-Se bands are not able to be seen in Raman, the decrease in the $GeSe_{4/2}$ band from these other glasses could be from Pb replacing Ge bonds in a four-fold coordinated manner, forming $PbSe_{4/2}$ units.
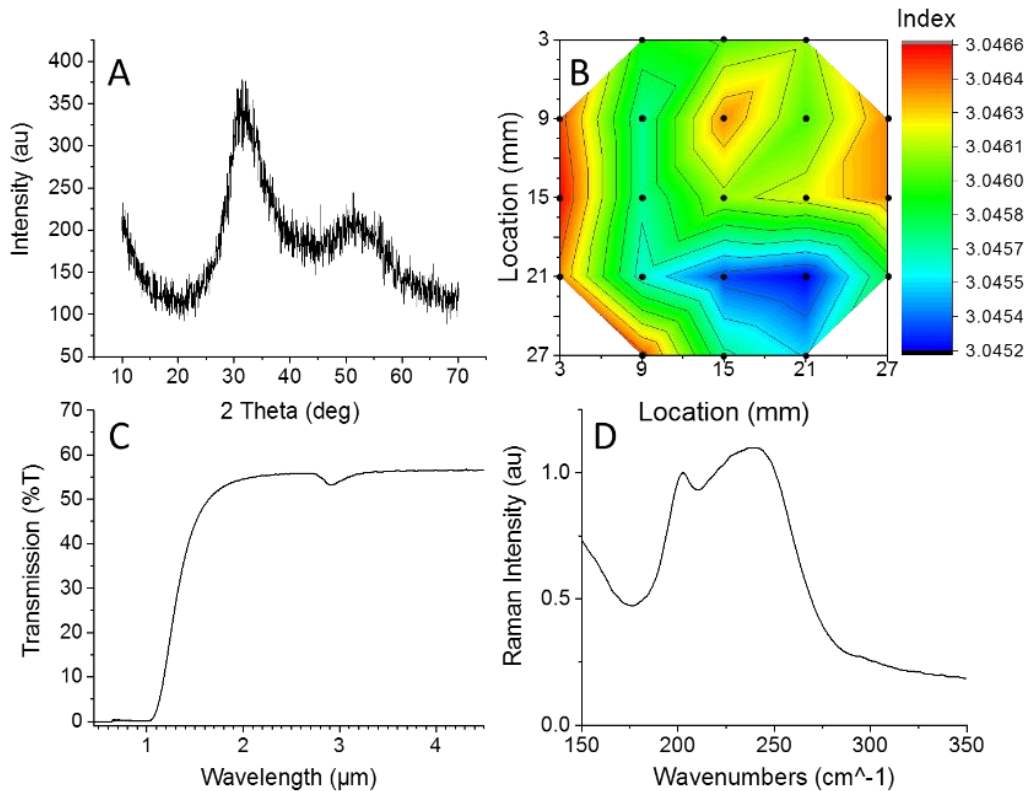
Figure 3-9 The XRD (A), refractive index homogeneity map at 4.515μm (measurement error is ±0.0005) (B), visible – short-wave infrared (SWIR) transmission (t = 2 mm), not corrected for Fresnel loss) (C), and Raman spectrum (D) excitation wavelength λ=532nm for base 40mol% PbSe glass. [39,126]

As the base glass has been thoroughly characterized, the post-HT material changes could also be measured and analyzed. This was first done with XRD in order to measure the degree of crystallization of the post-N+G samples and to determine if there was a temperature dependence on the crystal phases that would form. The XRD pattern for the 190°C nucleation temperature plus the various G temperatures is shown in Figure 3-10, and is a representative plot of what was seen with the other nucleation temperatures. For higher G temperatures there is an increase in the total f_v (peak height intensity), but there is little change in the relative volume fractions of the crystal types to each other. The lack of change in the crystal types and volume fraction ratios indicates that there is not a temperature dependence on the crystal phases that are forming, and that they all form

concurrently. The crystals that were identified were the same as those seen in section 3.3 and [39], and were As_2Se_3, PbSe, and Se. The crystal peaks seen and their respective crystal phases are 22° (Se), 31-33° (PbSe, As_2Se_3, Se), 44° (PbSe), and 53° (As_2Se_3). The volume fractions for the various HT samples is in Table 3-4.
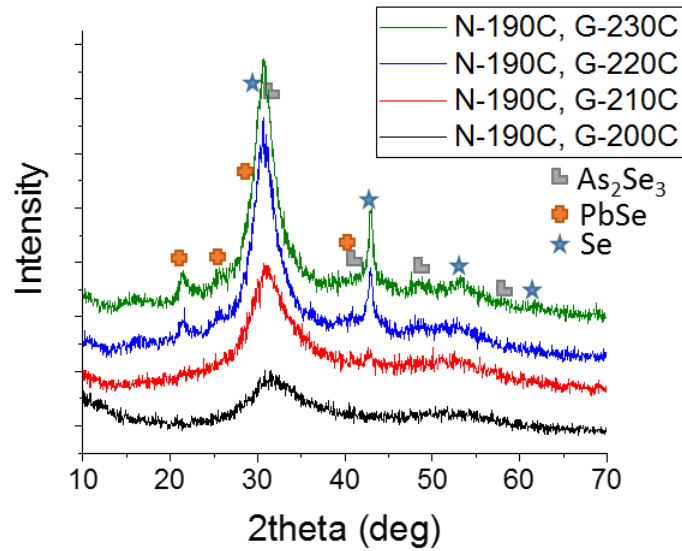
Figure 3-10 XRD for the 190°C nucleation plus different growth temperatures is shown as a representative plot for the other HT conditions used. The identified crystals in the patterns are labeled with the legend on the right. [39,126]

Table 3-3 The volume fractions (Vx) of crystals for each of the nucleation and growth conditions shown in Figure 3-10, with their calculated total volume fraction and relative ratio between the constituent phases.

Nucleation	Growth	As$_2$Se$_3$	PbSe	Se	Total	Ratio
No-Nucleation	G-200°C	0	0.1	0.1	0.2	0:50:50
	G-210°C	3.4	2.3	0.6	6.3	54:37:10
	G-220°C	8.5	6.3	1.8	16.6	51:38:11
	G-230°C	11.1	8.8	2.6	22.5	49:39:12
N-190°C	G-200°C	0.6	0.5	0.6	1.7	35:29:35
	G-210°C	7	4.9	1.5	13.4	52:37:11
	G-220°C	10.7	7.7	2.3	20.7	52:37:11
	G-230°C	14.2	10.5	3	27.7	51:38:11
N-200°C	G-200°C	0.3	0.1	0.1	0.5	60:20:20
	G-210°C	3.1	2.5	0.7	6.3	49:40:11
	G-220°C	9.3	7.2	.2	16.7	56:43:1
	G-230°C	13.1	9.5	2.6	25.2	52:38:10

The refractive index of the HT samples was measured after N+G and is plotted in Figure 3-11 for the various N conditions. For all nucleation temperatures there is an increase in the index with an increase in the G temperature, which follows with the increase in crystallization seen in the XRD. Additionally there is a shift of the refractive index curves for each nucleation condition to lower G temperatures for higher N temperatures. This relation is consistent with the IU curves in Figure 1-6, where there is an increase in the nucleation rate from 190 to 200°C. There is also the trend that there is a slow initial increase in the refractive index at low temperatures, an increase at mid temperatures, and then a leveling off again at high temperatures. This would be indicative of a slow turn on into the growth regime of the material for low temperatures, and then a maximum possible conversion at high temperatures.
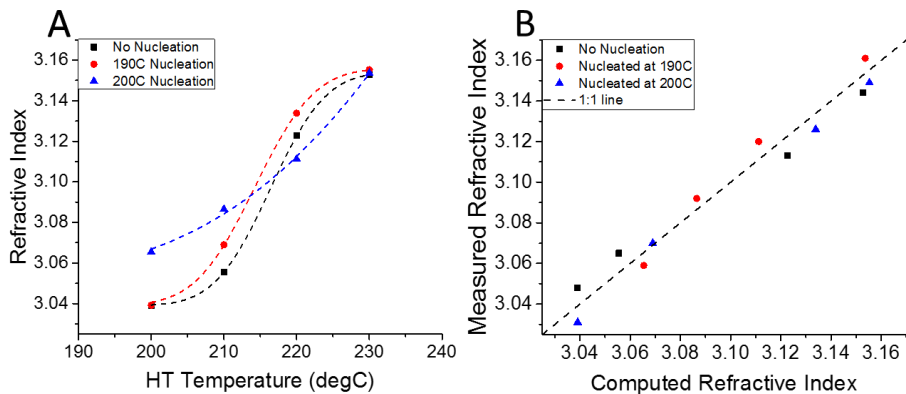
Figure 3-11 (A) The measured refractive index at 4.515μm is shown for the different nucleation temperatures against the growth HT temperature. The dashed line is a guide to the eye. (B) The measured refractive index is plotted against the calculated index from XRD data with the dashed line being the 1:1 ratio of the two values. [39,126]

The computed refractive index using the volume fractions of each crystal found in the

XRD using the Gladstone-Dale approximation, with known refractive index values of

those crystals, is plotted in Figure 3-11 against the measured refractive index. The dashed

line is a 1:1 line, and the data lies along this line for the various nucleation and growth

HT. This shows that the change in refractive index is indeed from the crystallization

occurring in the glass to form a glass ceramic and is independent of N or G temperatures

used.
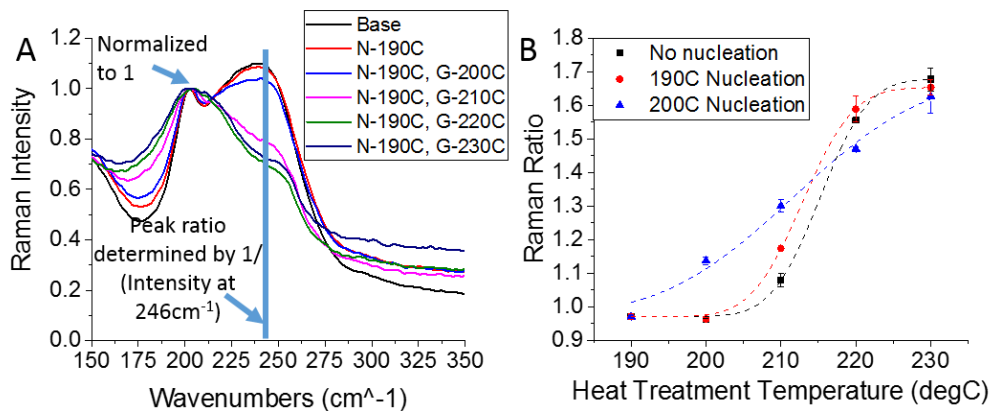
Figure 3-12 (A) Representative Raman evolution from base glass (black) for varying growth temperatures (all samples experienced 190°C nucleation HT). The quantitative Raman ratio is calculated by taking 1/intensity at 246 cm^{-1}. (B) The calculated Raman ratio for the different nucleation temperatures are plotted against the growth HT temperature. The dashed line is a guide to the eye. [39,126]

The evolution of the Raman spectrum for the different G temperatures with a 190°C N step is plotted as a representative sample in Figure 3-12. After N+G there is a systematic decrease in the broad peak at 246 cm^{-1} as the G temperature is increased. As can be seen, no crystalline peaks are able to be observed in the Raman spectra. PbSe is known to have peaks at 143 and 243 cm^{-1}, and As$_2$Se$_3$ has multiple peaks between 145 and 273 cm^{-1}, both of which are not seen. Since crystals were observed in these samples with the XRD measurements, it may be that the crystals have too small of a volume fraction or too small of a scattering cross-section to be able to be observed above the glassy background in the Raman measurement.

In order to qualitatively see the changes in the Raman spectra, the peak at 200 cm^{-1} was normalized to 1. In order to quantify the changes seen in the Raman spectra, a ratio was created, where the peak intensity at 200 cm^{-1} was divided by the intensity at 246 cm^{-1}. This ratio was then plotted for the different nucleation temperatures in Figure 3-12.

As the peak around 246 cm^{-1} contains numerous bands related to various As-Se vibrations, the decrease in this peak is associated with conversion of As-Se bonds in the glassy matrix to the crystalline form as As_2Se_3, which was one of the identified crystal phases formed. The other vibration in this band is a Se-Se peak, where Se was also a crystal phase identified in the XRD which would also decrease. The remaining crystalline phase seen in XRD was PbSe, and the Ge-Se$_{4/2}$ nor any of the As_2Se_3 peaks would be affected by the formation of this crystal phase. The overall trend in this plot is very similar to the one for the refractive index. Once again there appears to be a slow turn on, and a maximum Raman ratio value possible for the glasses. There again is a shift of the trace to lower G temperatures for higher N temperatures. This again would likely be due to an increase in the nucleation as shown in the I-U curves in Figure 1-6.

This Raman ratio can then be used to solve for the local G temperature seen in a sample if the N treatment is one of those used here. This can be performed by measuring the Raman ratio locally on the sample, and then using the appropriate Raman ratio versus HT plot for the N condition used to solve for the G temperature seen locally. Inversely if a spatially varying nucleation temperature was used, and one knows what the G temperature was, then the variances in the nucleation temperature could be solved for. As a gradient N or G temperature would create a GRIN in these material, this characterization technique could be used to verify what the thermal profile was that created the GRIN in the sample through measuring the Raman on various cross-sections through the sample.

In order to see if the Raman spectrum could yield valid quantitative information on the refractive index of the post-heat treated material, the Raman ratio was plotted against

the measured refractive index of the glass ceramic in Figure 3-13. There is a nearly linear

trend between the two measurements, which gives a high correlation between them and

shows that the Raman can be used to spatially determine the refractive index of a sample

of this material. There is a slight deviation at higher temperatures, which could be due to

the leveling out of the Raman change and a decrease in the Raman signal intensity for

high G conditions. This decrease in the signal yields more error in the calculated ratio,

and with the small changes seen in the ratio between high G temperatures the accuracy of

the ratio calculation could be affected by this additional noise. As the refractive index

was shown to be from the crystallization in the material, the Raman spectrum therefore is

able to give information on the amount of crystallization that has occurred in this material

upon HT with high spatial resolution compared to standard absolute index measurement

techniques.
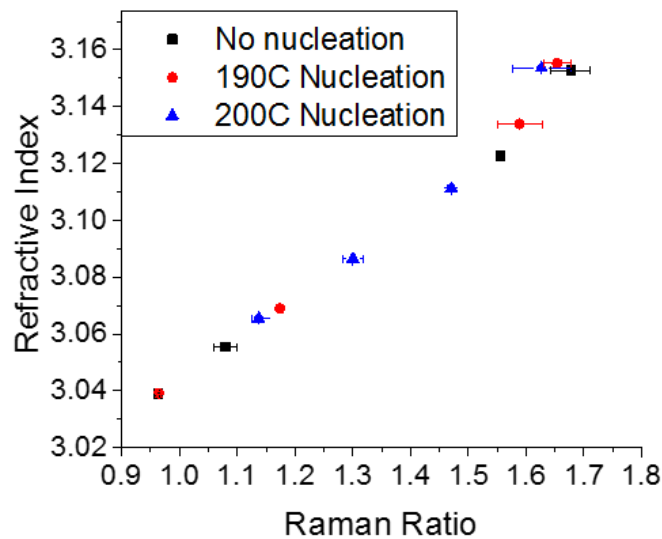
Figure 3-13 The measured refractive index at 4.515μm is plotted against the Raman ratio for the respective N+G heat treatment that was performed. [39,126]

Transmission was also measured for the different samples in order to verify that after

the HT performed, the samples would still be able to be used for MWIR optical systems.

The SWCO, as measured as the 90% of the max transmission, is plotted against the G temperature with each color representing a different nucleation temperature in Figure 3-14. As the growth temperature increased, the SWCO also increased. This tracks well with the increase in the total volume fraction of crystals present in the material. The sample without a nucleation HT at the highest growth temperature had the lowest volume fraction of crystals, yet the highest SWCO. One can surmise that there was less nucleation in this sample, and that the crystals that grew ended up being much larger in size, causing an increase in scatter. This shows that the nucleation was able to create a higher volume fraction of smaller crystals which allowed the composite to maintain its transmission SWCO. At the lowest HT temperature the un-nucleated sample did not contain any As_2Se_3, while the nucleated samples did. The un-nucleated sample also had the lowest SWCO, which would be from the lack of highly scattering As_2Se_3. For the middle two HTs, the transmission and crystal volume fractions were all very similar to each other. Even with the increased scatter from the un-nucleated sample, all of these samples would still be applicable for use in MWIR optics. With a maximum index change of ~0.12 RIU, these materials can produce GRIN profiles with a high index change while still maintaining their transparency.
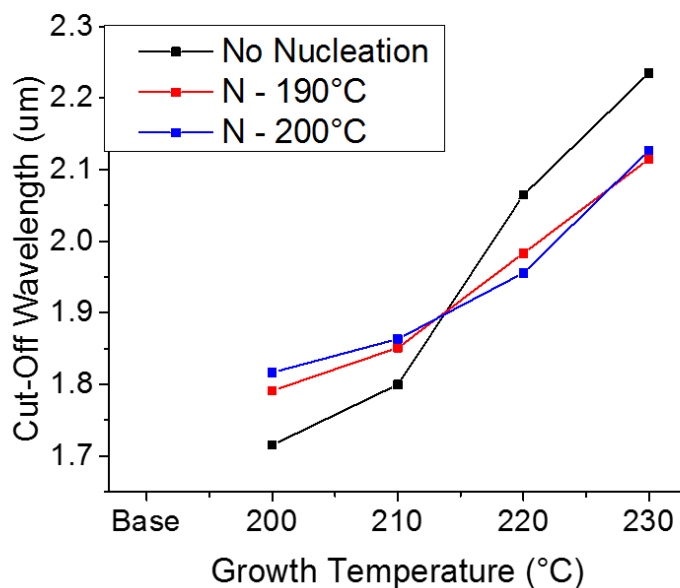
Figure 3-14 The transmission SWCO as defined by the 90% of the maximum transmission is plotted for the different nucleation conditions against the growth HT temperatures, and error is within the measurement point.

This section highlights the impact of the fixed HT protocol (N and G time and temperatures) used for this single, 40 mol% PbSe glass composition. While the attributes of the post-processed glass ceramic vary, they are defined by the base glass composition and morphology. The degree of crystallization in this material was able to be tied to the refractive index, which was then able to be tied to the Raman spectrum. This showed that the refractive index changes were from the crystallization, and therefore the Raman spectrum, and was also tied to the crystallization processes occurring. These relations allow for the use of the Raman spectrum to measure the refractive index in the material, as this allows for a spatially selective way to measure the refractive index.

3.6   Conclusions

Glasses with compositions of $(GeSe_2-3As_2Se_3)_{1-x}PbSe_x$ with x=0 to 40 in increments

of 5 mol% were evaluated for their ability to form glass ceramic upon HT. The formation

of various crystallized phases (phase type and quantity) as identified via XRD was related

to the optical composite's refractive index, which showed that the refractive index change

was solely due to the heat treatment-induced crystallization. The change in the

transmission was also tracked to determine if the crystallization in the material still

maintained its transparency, and therefore application in the MWIR. In many of the

property measurements the composition within the Pb-series examined, changes in trends

tended to occur around the 30 mol% PbSe composition. This composition also sits at the

morphological change boundary where the matrix/dominant phase in the phase separated

glass matrix becomes Pb-rich. This is also the point where the change in precipitated

crystalline phases occurs.

Of the multiple glass compositions examined, the 40 mol% PbSe material exhibits the

greatest potential for use in MWIR optics as related to the desirable attributes as

quantified in Table 1-3. This material showed the highest potential index change of the

glasses examined following this fixed, two step, nucleation plus growth (N+G) heat

treatment protocol used, and maintained its transparency in the MWIR. In this study,

crystal phase formation, as quantified by XRD, was correlated to refractive index, which

was subsequently correlated to the Raman spectrum with a metric defined by the Raman

ratio. This correlation in analysis allows us to tie the Raman spectrum and refractive

index directly to the amount of crystallization that occurred in the samples as a result of

the heat treatment protocol, and allows for a conversion of the Raman spectrum into a

'refractive index space' in order to have a spatially selective way to measure and

quantify, refractive index and its change with conversion from glass to glass ceramic. The maximum index change observed as a result of the fixed, two-step N+G protocol was +0.12 RIU, and the MWIR transparency was maintained.

Now that the ceramization of the material via conventional thermal processing is understood, and a spatially selective way of measuring the refractive index was able to be developed with Raman spectroscopy, index patterning can be performed and the resultant material can be characterized for its refractive index profile as well as other material properties.

4   LASER-ASSISTED CRYSTALLIZATION

Chapter 3 demonstrated the power of thermal treatment on inducing controlled crystallization in a phase separated infrared transparent glass. While the attributes of the starting material were complicated by the LLPS present in the base material, the two step nucleation and growth protocol used resulted in changes creating an infrared transparent glass ceramic. This work showed that the 40 mol% PbSe could be controllably crystallized through a two-step thermal treatment using the selected criterion noted earlier for defining the temperature and time of heat treatment, and this treatment imparted changes in physical and optical properties in the optical nanocomposite.

The ability of the material to be able to be crystallized in a *spatially controllable* manner would allow us to induce a tailorable GRIN structure. This section highlights the use of laser exposure on this base glass material replacing either the N or G of the process previously demonstrated with a furnace-based thermal treatment. In order to be able to spatially control the refractive index in the material, a laser was used to modify the nucleation or crystallization state of the material. It was assumed in this section that the Raman ratio that was developed in section 3.3 is still applicable to the laser treated samples, as the Raman measurements were shown to be indicative of the crystallization state, and not just a specific combination of N+G HT that was performed.

Three different types of laser sources were used including a CW, 532 nm laser, a ns pulsed 1.064 μm laser, a fs pulsed 1.3μm laser, and a fs pulsed 1030nm laser. The first two lasers were used to induce crystallization in the material, while the third was used to induce nucleation in the material. This chapter reviews the effects of these different laser irradiation regimes, their unique attributes and drawbacks as applied to the GAP-Se

material, and specifically how each can be applied to our candidate 40 mol% PbSe composition. We then report how laser exposure can be used towards our goal of spatially selective crystallization for an optical glass ceramic and present results from these experiments.

4.1 CW laser growth

The first set of experiments aimed at using a laser as a spatially varying heat source throughout the material in order to have different growth rates spatially in order to spatially have different volume fractions of crystallization. This HT was achieved with an above bandgap energy, CW laser. The laser conditions needed to create a specific profile was determined through simulations, and were then experimentally performed on 40 mol% PbSe glass. The heating profile was created with a Gaussian laser beam that was above the bandgap energy of the material, which created a varying surface heat source, and therefore a varying thermal profile throughout the volume of the sample. This sample was characterized with Raman spectroscopy post-irradiation. This Raman map across the sample could then be used to solve for the thermal profile that the sample saw, as well as the estimated refractive index profile of the sample. These were then compared to the simulated profile to see how closely the simulation matched the experiment.

4.1.1 532 nm laser exposure modeling

Simulations of the laser-induced heating were performed with COMSOL Multiphysics in order to determine the irradiation conditions that would be needed to create a specific GRIN profile in a sample with a high index region in the top center of the sample that then tapered off to the base refractive index at the edges and back of the sample. Measured material property values of this composition were used in the

106

calculations. This profile was desired as it resembles the index profile for a flat lens, it could be created with a Gaussian laser beam that is above the bandgap energy of the sample, and it allows for a slowly varying index profile across the sample to aid in characterization. This index profile translates to a needed temperature profile of 230°C at the center of the irradiated region for high crystal growth, transitioning to around 190°C at the edges in order to have no crystal growth.

The base model used in the simulations is described in section 2.13, and utilized a surface heat source that was time-invariant. In order to determine what power level and beam waist were needed, these two parameters were varied in the simulation using Livelink for Matlab. This enabled the simulations to be performed in batches as well as allowing for easy export to and processing of the simulated data in Matlab as described in section 2.13.

It was determined that the heat profile would not be wide enough to create the wanted GRIN profile with the limited maximum power of the laser that was to be used in experiments while achieving a maximum temperature of 230°C with the sample at room temperature. By analyzing several of the simulated profiles, it was determined that performing the irradiation at an elevated background temperature might be able to alleviate this issue. Simulations were then performed in order to see if a profile with a peak temperature of ~40-50°C and temperature spread of ~30-40°C from the center to edge could be created within the power output of the laser used. From this maximum temperature and temperature spread, coupled with an external temperature of 190°C, the wanted profile could be created. This elevated temperature was deemed acceptable since it was the same as the nucleation condition to be used in the experiments.
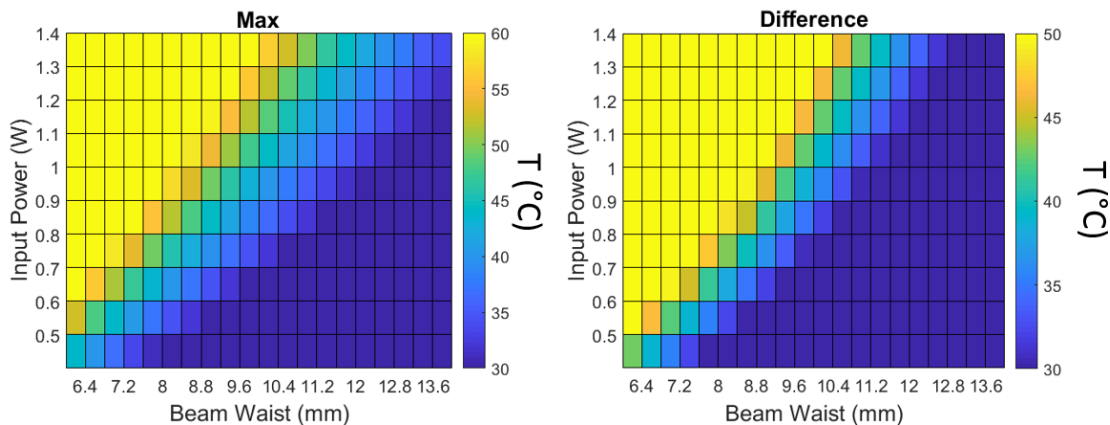
Figure 4-1 Output data from COMSOL simulations was used for (A) plotting the temperature change from the center of the sample to the edge and (B) estimating the maximum temperature seen in the middle of the sample for different input powers and beam waists. Pure yellow or dark blue are indicative of values above or below the temperature scale seen for each image as the scale was reduced to show additional contrast in the regions of interest.

Figure 4-1 shows the results of these simulations where the maximum temperature

reached is plotted for different input laser powers and beam waists. The difference

between the maximum and minimum temperature seen in the model was also plotted for

the same. The regions of deep yellow or blue are above or below the ranges wanted

respectively, and the transition region between these two were the conditions of interest.

In order to create this external temperature of 190°C, the irradiation was planned to occur

through the outlet vent at the top of a box muffle furnace as depicted in Figure 4-2 below.

The green profile on top of the "laser beam" is a reference to the Gaussian profile of the

laser used. With this tool defined, and needed experimental conditions known, they were

then used on a pre-nucleated sample in order to spatially vary the ceramization in the

material. The resulting sample was then characterized with Raman spectroscopy.
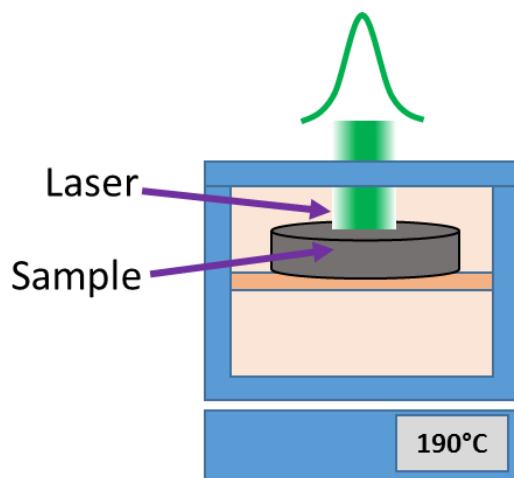
Figure 4-2 The experimental set-up used for the laser irradiation experiments in the furnace. The sample was placed on a refractory brick inside the furnace set to 190°C, and the Gaussian laser beam was sent through the outlet vent at the top, perpendicular to the sample surface. Note furnace is not drawn to scale.

4.1.2   532 nm laser exposure experiment

A pre-nucleated sample was then able to be irradiated with the experimental

conditions that were determined through the simulations. Samples for this experiment

were from a 350g batch that was prepared as described in section 2.1 with the 30mm

diameter tubes. The irradiations were performed on full 30mm diameter, 2mm thick

slices. The slices were pre-nucleated for 2hrs at 190°C, and then were irradiated for

30min in an external temperature of 190°C for the growth step. These times were the

same as those used in section 3.1, so that the Raman to index relation that was found

would be valid for this experiment as well. The base glass of this sized melt and the one

in section 3.1 were checked with EDS using a Zeiss ULTRA-55 FEG SEM to rule out

variances between the starting materials between the two batches, and were seen to have

the same starting compositions.

The irradiation was performed with the 532nm laser described in section 2.14 that

was expanded to a larger beam waist, and was directed into the outlet vent at the top of

the muffle furnace used in experiments in section 3.1 in order to create the external temperature of 190°C. The reported average powers were measured after the last mirror, just before the inlet vent of the furnace. The different irradiation conditions that were performed are summarized below in Table 4-1 and the laser intensities used were from 0.57- 1.08 W/cm^2. Some of the conditions were repeated in order to assess repeatability in the material. Characterization of all samples can be found in section 6.1, with only one of the 0.89W and 10 mm beam waist samples characterized here with Raman spectroscopy.

Table 4-1 The different experimental conditions for the CW, 532nm laser used are shown.

Power (W)	Beam waist (mm)	Sample temperature (°C)
0.89	10	190
0.89	10	190
0.89	12	190
1.113	10	190
1.113	12	190
1.113	12	190
1.340	12	190
1.558	10	190
2.003	10	190
2.003	10	200
2.23	10	200
2.448	10	200

This sample was sliced through the center of the irradiated region in order to evaluate the Raman spectra of the cross-section. After cutting and lightly polishing the sample, Raman spectra were measured in a grid along this x-z plane with a spacing of 1mm in the x-direction, and 0.25mm in the z-direction as depicted in Figure 4-3. This Raman map

across the sample could then be used to determine the temperature profile from the

irradiation as well as the GRIN profile using data from section 3.5.
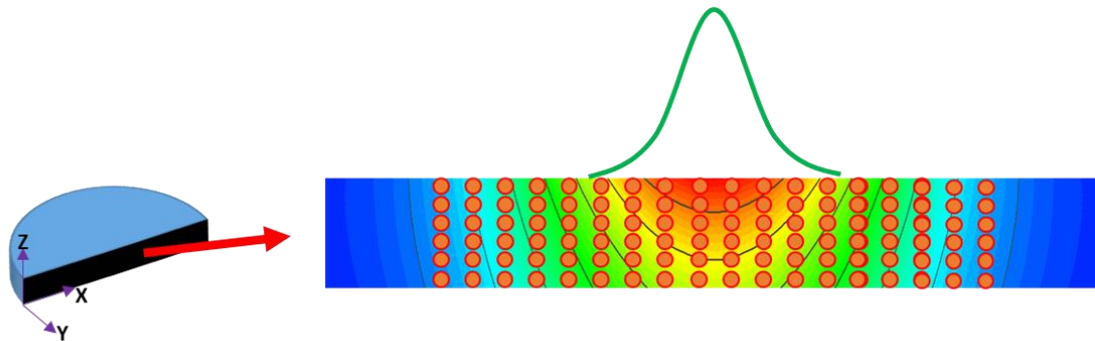
Figure 4-3 The left depicts the slice that was cut in half, and the face that the Raman was measured on is expanded on the right. A representative thermal map was added to this surface, where red is high temperatures, and blue is low. The red circles represent the locations where the Raman was measured at, and the green Gaussian profile depicts the incident laser source. Note the images are not to scale. [39,126]

The Raman measurements were then converted into the Raman ratio as described in

in section 3.5. These Raman ratios could then be compared with the ratios measured in

section 3.5 for the 190°C nucleation condition as a function of temperature to convert the

change in Raman to the temperature that would have caused that conversion. This

temperature map could then be compared to the simulated temperature profile from

section 4.1.1. The refractive index map was created using a similar method, but instead of

using the Raman ratio versus HT, the Raman ratio to index relation as determined in

section 3.5 was used. The temperature profile from the simulation was also converted

into index by using the refractive index versus HT data for the 190°C data from section

3.5. These two temperature maps were then compared to each other by spatially

subtracting the temperature at each pixel of the experimental data from that of the

simulated data to determine how well the two matched. With these tools defined, they

will be applied to pre-nucleated samples which will be subsequently characterized with Raman spectroscopy to map out the resulting refractive index profile.

4.1.3   532nm laser exposure characterization

Raman spectroscopy was used to characterize one of the 0.89W, 10mm beam waist samples in order to determine the GRIN profile throughout the sample. This sample was cross-sectioned and Raman spectra were measured along this cross-section that were then converted into a temperature scale using the Raman ratio versus G temperature profile for the 190°C N condition and later to a refractive index profile. The temperature profile as determined through the Raman measurements is shown in Figure 4-4 along with the simulated temperature profile. Both of the profiles show the highest temperature in the center, going out to low temperature at the edges, which was the desired profile. The simulated profile has a broader heat distribution both radially and axially, but exhibits a lower peak temperature. Overall the two profiles show decent correlation, which means that to a first order the simulations and their inputs were reasonably accurate. A possible source of error is that the Raman ratio versus G temperature plot was created with samples from a different glass melt, and if there were variations in the starting morphology of these melts there could have been slightly different amounts of crystallization. As the compositions of the batches were measured there were not any compositional changes between them. This does not rule out any changes in the base micro-structure. Another possible source of error would be that the sample was not cut exactly in the middle of the irradiated region, which would cause the measured irradiated region to be smaller and have a lower peak temperature than the exact center of the irradiation. Lastly there could have been error in the boundary conditions used for the

simulations, as the heat transfer coefficient for the convective flux boundary condition

was not able to be measured directly for this material.
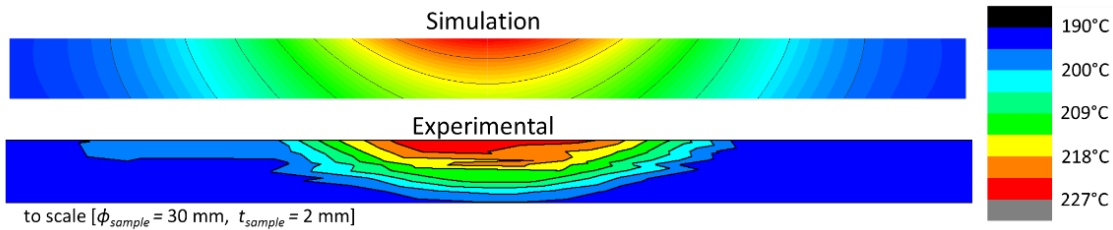
Figure 4-4 The simulated temperature profile is plotted (top), as well as the experimental Raman map that was converted into temperature through the Raman ratio versus temperature curve (bottom). [39,126]

The same Raman data was also converted to refractive index by the Raman ratio

versus index plot, and the simulated temperature was converted to refractive index

through the refractive index versus G temperature plot for the 190°C N and are shown in

Figure 4-5. Both profiles are much more similar horizontally than for the temperature

plots, though the values decrease more rapidly for the experimental sample. In the Z-

direction, the simulation goes much deeper, but again has a more gradual decrease. Also

plotted is a difference map, where the two profiles were spatially subtracted from each

other (simulated-experimental), to show the difference in the refractive index spatially.

This shows in a more quantitative manner that the experimental peak index is larger than

the simulated, and the simulated profile extends further into the sample. The possible

sources of error mentioned above for the temperature maps are also possible sources of

error for these refractive index profile maps.
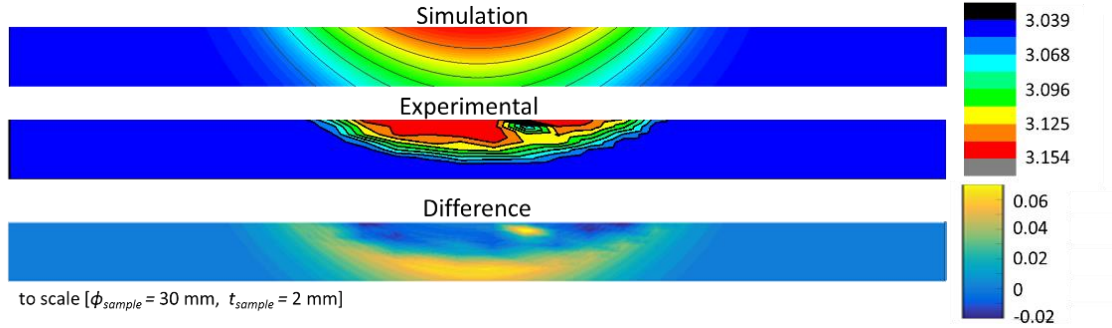
Figure 4-5 The simulated temperature profile was converted to index through the temperature versus index correlation on top. The experimental Raman map into temperature through the Raman ratio versus index curve in the middle. The simulated profile minus the experimental profile were then spatially subtracted (bottom). [39,126]

The thermal profile used in this section was successful in being able to form a GRIN in the material. One issue with this technique is that the laser is not transparent to the material, so only certain thermal profiles could be obtained with this laser, and these profiles are controlled by heat diffusion in the material. Also long processing times are needed, on the order of 30min, to grow the crystals. In order to reduce the time needed, and to potentially be able to modify the material in a more controllable manner in the bulk, the use of a ns pulsed laser source was investigated.

4.2   Nanosecond laser-induced growth

A pulsed laser source was then investigated in order to see if it could have a lower processing time to form a GRIN, to have the ability to potentially modify into the bulk of the material, and to have modifications that are not dominated by thermal diffusion. This greater control of the irradiation would allow for more potential refractive index profiles in the material. The effect of a nano-second laser on the 40mol% PbSe composition was investigated. The initial mechanism explored was laser-induced crystallization on the

base glass. The irradiation was then subsequently probed with Raman spectroscopy to confirm any crystallization in the material.

Pertinent to the discussion of pulsed laser sources is the non-linear index and absorption, which has been measured by collaborators at Singapore University of Technology and Design (SUDT). The n_2 was measured to be 1.24E-05 $\pm$ 3.54E-06 cm^2/GW. The a_4, the non-linear multi-photon absorption coefficient, was found to be 1.15E-02 $\pm$ 5.31E-3 cm^5/GW^3.

4.2.1   Nanosecond laser-induced growth experimental

An exposure was performed on a 40mol% PbSe sample that was a quarter of a 30mm diameter slice. This sample was placed inside an external heat cell that was set to 180°C. The slice was then irradiated for 7 min with the 1064 nm laser source described in section 2.14. The laser beam was expanded to ~3 cm using a telescope lens and then went through a 11.5mm diameter aperture to create an approximately flat-top beam. An average power of 1.8W post aperture, which has a fluence of 0.006J/cm^2 (0.43W/cm^2), was used. Raman of this sample was then taken across the sample surface with a spacing of ~2mm as described in section 2.6, except that an objective lens of 10x was used with a dwell time of 6min (six co-additions of 60s) instead of the 20x lens for 2min 15s. The top surface of the sample was then polished and the Raman was re-taken. The Raman was then also taken of the back surface of the sample. These multiple layers were measured in order to develop Raman maps at various depths in order to determine how the irradiation affected the material throughout the sample. Thermal modeling of the system was also performed with COMSOL Multiphysics in order to see if laser-induced heating occurred, and could be compared to the furnace only HT samples described in section 3.5. Due to

the low repetition rate compared to the pulse duration, one pulse was modeled for the length of the pulse and for the length of time between pulses using the same base model described in section 2.13 with a time-dependent, volumetric heat source. The heating seen for the single pulse was then multiplied by the number of pulses that hit the sample during the exposure time used in the experiment. This was done as any temperature increase seen between the first pulse and the start of the second pulse would be similar for all the pulses, except for a potential steady-state temperature reached, and could be used as a first approximation of the amount of heating in the sample. This model used a spatially varying volumetric heat source, which had a term for the absorption present in the material, and the value for this was calculated from the transmission curve of Figure 3-9, and was determined to be 14.9 ± 0.2 cm^{-1}. With these tools defined, they will be applied to a base glass sample in order to determine the effects of the post-irradiated sample on the ceramization of the material.

4.2.2   Nano-second laser-induced growth characterization

The post-irradiated sample was evaluated with Raman spectroscopy to map the ceramization state throughout the sample. After the 1064nm sample was irradiated the Raman spectra was taken at various locations across the surface of the sample. This surface was then polished down and another map was taken. A third Raman map was also created on the bottom of the sample. A depiction of the removal process that was performed is seen in Figure 4-6. The Raman spectra from these maps was able to be classified into four main categories as seen in Figure 4-6 and include, melted (black), unmodified (red), normal crystallization (blue), and high crystallization (green). In previous experiments the melted and high crystallization signatures had not been

116

observed. Under a visible microscope the material in the middle appeared to have melted, which is where this classification came from. The melted region did have a spectra that resembles Raman spectra for base compositions with lower Pb-contents [40]. Right outside of this melted region the higher crystallization spectra was observed. This region appeared to be crystallized, and had a much sharper peak at 200cm^{-1} and comparatively lower signal around 246 cm^{-1}. This decrease could be due to species migration into the "melted" region causing higher values around 246 cm^{-1} for the melted region. It also could be that more As_2Se_3 was able to crystalize, as the remaining peaks appear to be related to Ge-Se and Se-Se units [84]. The melted area and the crystallization region immediately around it did not have Raman spectra that had been seen before, and therefore the refractive index for that specific location is unknown.
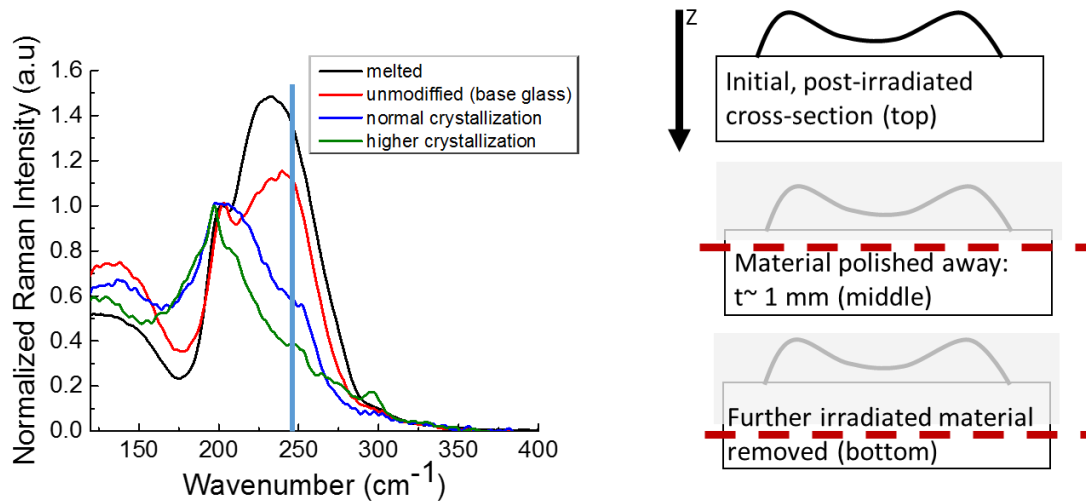
Figure 4-6 The four different characteristic Raman spectra seen in the experiment on shown on the right, with the blue line being the wavenumber that is used for the Raman ratio. The right depicts the technique used to determine the index profile through polishing the sample.

These Raman ratio maps for the different depth levels are shown below in Figure 4-7, and could not be converted into temperature or refractive index as some of the signals did

not match ones seen for furnace HTs. The dots seen on the pictures of the sample

correlate to the locations where Raman was measured, and are divided up into 4 colors

for the four observed characteristic spectra, red – re-melted, orange – high crystallization,

yellow – normal crystallization, and green – base. The Raman ratio of the re-melted

region is actually lower than that of the base glass, and is the reason for the dip seen in

the middle of the top Raman map. Other than the melted region, a similar profile pattern

to the CW irradiated sample in section 4.1.3 was seen where the sample had a bowl

shaped Raman ratio profile going through the depth of the sample. Thermal modeling of

the system concluded that there would be a negligible temperature change with the given

laser conditions, and is likely therefore largely a photonic effect.
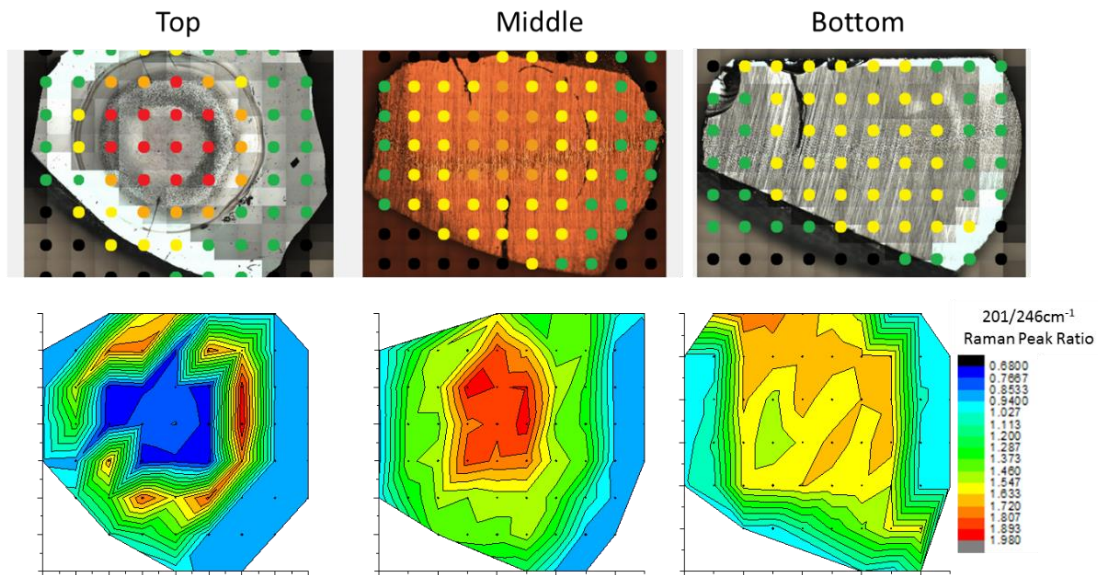
Figure 4-7 The circles in the top pictures show the locations where that Raman spectra were taken. The coloring refers to the characteristic spectra that was seen at that location, with red = melting, orange = high crystallization, yellow = normal crystallization, and green = base glass. The bottom graphs show the mapped Raman ratios that were measured. Data could not be correlated to temperature or index as some of the Raman spectra did not resemble those from furnace HT.

This laser source was able to modify the material throughout the bulk of the material, but appeared to have a similar effect to the CW laser that was used. This laser source was not in a highly transparent region of the material, so a laser source further into the transparent region was wanted. Also as the simulations showed that little heating was involved in the material it was thought that a fs source may be able to better induce a temperature change, and would also keep any induced HAZ to a minimum in the material eliminating any potential heat diffusion effects around the irradiation.

4.3   Femto-second laser-induced nucleation

In order to have more spatial control of the crystallization in the glass, a fs source that is further into the transparency region of the material was used. This source was used to modify the nucleation state of the material. This sample could then have a G HT, in order to grow crystals only where nucleation sites were grown with the. The effect of a femto-second laser on the 40mol% PbSe composition was investigated. The initial mechanism explored was laser-induced nucleation on the base glass. The irradiation was then subsequently HT and probed with Raman spectroscopy to confirm any induced nucleation in the material.

4.3.1   Femto-second laser-induced nucleation experimental

The fs irradiation was used in order to have more spatial control of the irradiated region with less HAZ, and to be able to use a laser source that is further into the transparency region of the material in order to have spatial control within the bulk of the material. Polished 30mm diameter samples were used to nucleate bulk 40 mol% PbSe samples. These samples were batched as described in section 2.1, but were polished commercially by Sydor Optics with a similar RMS roughness and a greater degree of

119

surface flatness (less wedge) to those polished at the University of Central Florida. The fs, 1.3 μm laser as described in section 2.14 was used in these experiments. This wavelength is in the middle of the SWCO of the glass where the absorption coefficient was measured to be 0.37 cm $^{-1}$. The pulse duration of the system was 110fs, and the average power used was 52mW. A lens was placed in the beam path to focus the laser down to 10.7 μm. This focus was then placed spatially above the sample, and was moved closer or further away during irradiations in order to have different irradiances at the surface of the material as depicted in Figure 4-8.
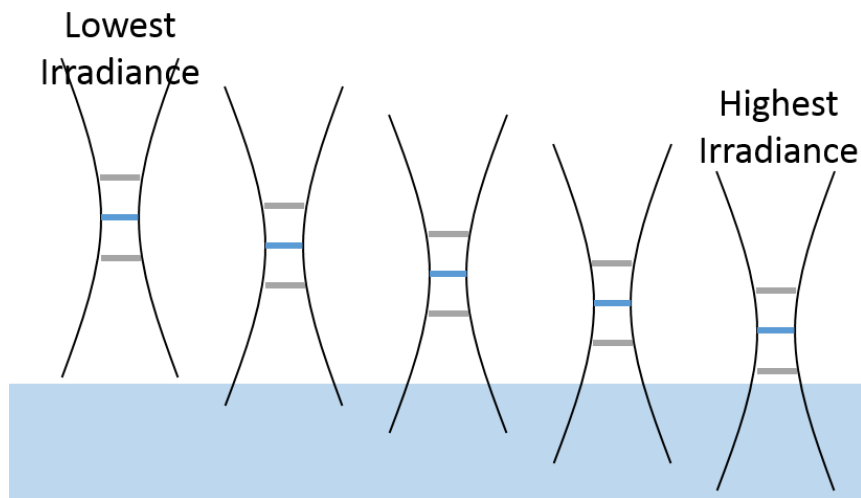
Figure 4-8 Minimum beam waist was generally 3-5mm above the surface. Beam waist was always above the sample and the beam waist at the sample surface was 0.2-0.3mm

Rectangles of a single irradiation condition were made in a snake-like pattern on the sample surface. The pitch between lines and the speed of the write could be modified, and for the reported experiment a pitch of 0.01mm and a writing speed of 1mm/s were used. The distance of the focus above the sample ranged from 1.6-7.2mm, which lead to beam waists of 0.1-0.43mm and fluences ranging from 0.018-0.365J/cm^2 (18-365 W/cm^2).

The Raman spectra of the irradiated regions were measured post-irradiation to ensure that no modifications occurred from the laser alone. The sample was then HT for 220°C for 30min in order to have growth only in the regions that were nucleated by the laser, but no change would occur in the regions without any pre-nucleation. The Raman spectra was then measured again post HT to see if modification could be observed from crystal growth, which would indicate that nucleation had occurred in the material. With these tools defined, they will be applied to base glass that will then be post-HT in order to determine the changes in the number density of nucleation sites in the material from the irradiation.

4.3.2 Femto-second nucleation characterization

The samples were characterized after their HT to determine if any modifications in the number density of nucleation sites, and therefore final crystallization state occurred in the irradiated regions. These changes were determined through Raman spectroscopy of post-irradiation and post-irradiation plus G HT. Irradiations were divided into six different sets, where 6-12 individual irradiance conditions (distance from the focus to the sample surface) were written into the samples. The differences in the irradiance levels within each set were relatively low, and then larger jumps in the irradiance level occurred between the sets. The regime that was wanted for laser-induced nucleation would be little to no surface modification (with possibly slight expansion of the material), and then upon a G HT the Raman spectra would change indicating crystal growth as seen in section 3.5 for thermal HTs.

The post-irradiated regions were first investigated with the visible microscope available on the Raman spectroscopy system. A stitch of the entire irradiation region is

shown in Figure 4-9. Ablation was observed for the highest power set, slight modification

for sets 2-3, and then set 4 dipped below the irradiation level for no surface

ablation/modification. The surface profile of the sample was investigated with the white

light interferometer described in section 2.12. The only change in height seen in these

samples was from the ablation/surface modification (ripples) and the maximum amount

of surface modification seen was less than 0.5um, except for set 1, where trenches were

drilled into the sample.
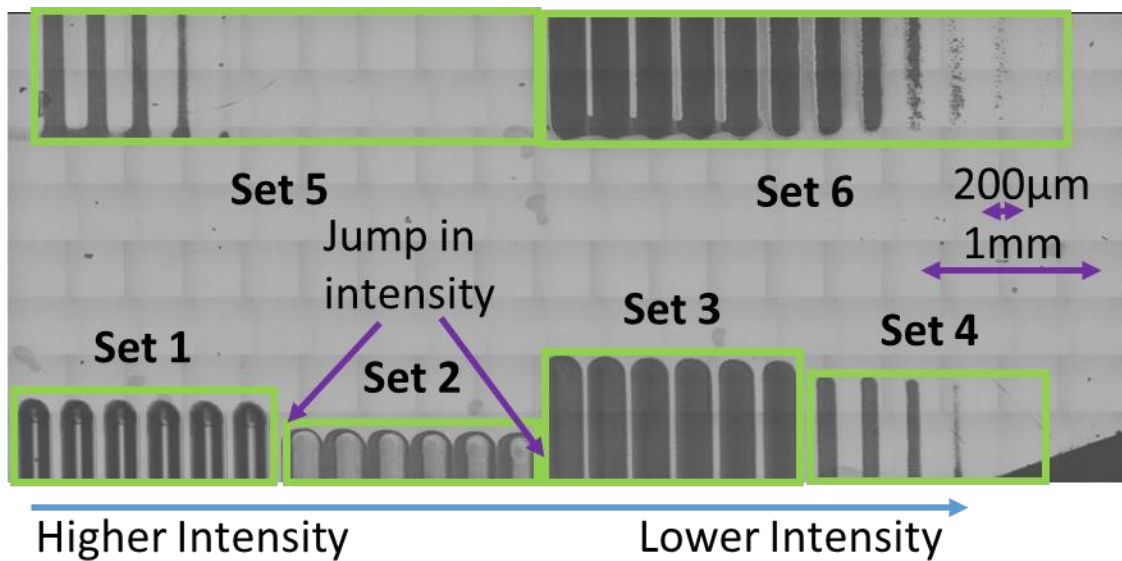
Figure 4-9 The irradiated regions with the 1.3 μm, fs laser are shown. The irradiations were split into 6 sets with jumps in the irradiance between each set, and going from high intensity on the left to lower intensity on the right.

Higher magnification images of sets 1-5 are shown below in Figure 4-10. Image A

shows a trench from set1, where there is a clearly defined edge to the trench and a very

small HAZ. Image B is from set 2, and shows non-uniform modification across the

modified region, with more structured modifications (lines) in the darker regions. Image

C shows a uniform change across the modified region, with line-like structures appearing

perpendicular to the laser writing direction. Image D also shows a uniform change across

122

the modified region, with line-like structures. The direction of these lines though changes spatially, with the edges and center of the irradiated areas having perpendicular directions (edges parallel, center perpendicular to the writing direction). Image E again does not have uniformly modified regions, and the edges of the modified region are not well defined. Small protrusions from the main modified region show signs of the beginning of these line-like structures, or micro-gratings, and their direction is parallel to the laser writing direction.
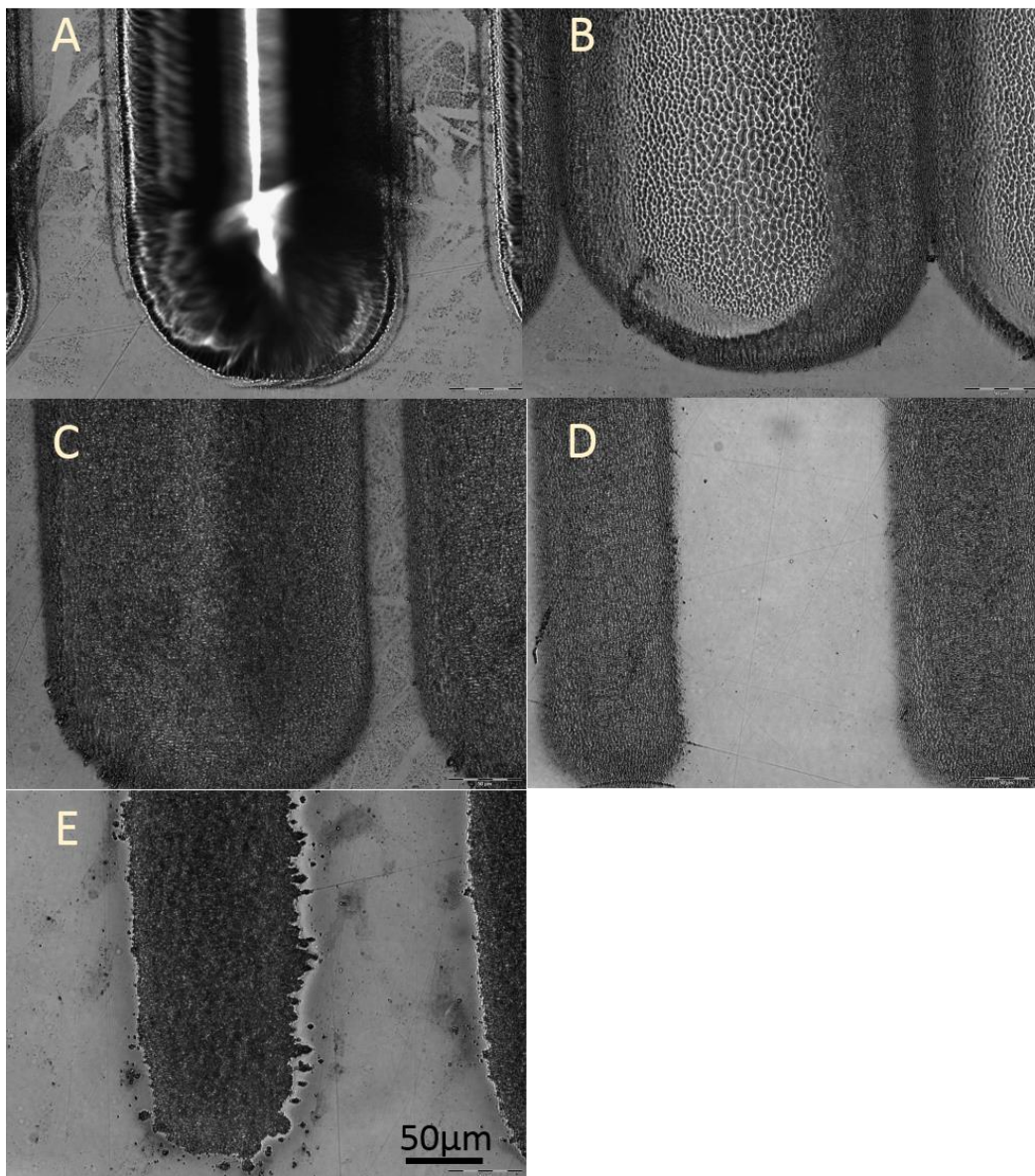
Figure 4-10 White light images for one of the irradiated rectangles for set 1 (A), set 2 (B), set 3 (C), set 4 (D), and set 5 (E).

Raman Spectroscopy was performed post-irradiation, and confirmed that there was no measureable change in the spectrum from the base glass. After the growth HT the Raman was re-measured. The only set that exhibited a change in the Raman was set 2. The Raman spectra for these locations post irradiation, and post irradiation plus HT are seen in Figure 4-11. The fluence range for laser irradiation for this set was 0.044-0.056 J/cm^2

(44-56 W/cm^2), and was the 2nd highest intensity set. This was unexpected, as it was assumed that the sample would only nucleate in regions where no obvious surface damage/modification would occur.
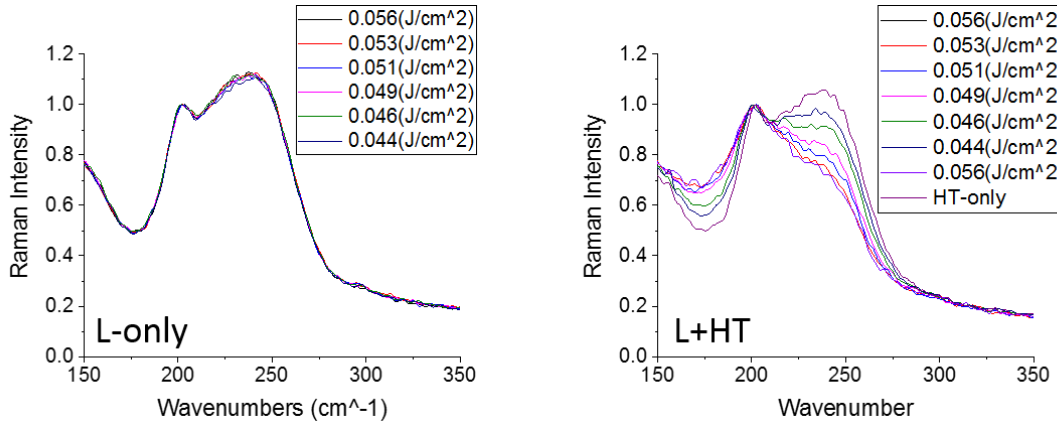
Figure 4-11 The Raman spectra is plotted for set 2 for both the laser-only condition (left) and laser + furnace growth (right).

A systematic decrease in the Raman peak intensity around 246 cm^{-1} was seen with an increase in the average intensity of the laser beam. In in section 3.5 this decrease in the Raman spectra at 246 cm^{-1} was determined to come from the crystallization of the material, which means that there was an increase in the amount of nucleation with the increase in the average intensity. The material also appears to be very photosensitive, as a small change in the fluence causes changes in the nucleation state of the material. As the modified region was non-uniform, an investigation into the spatial variation of the spectra across this area was performed. This is depicted in Figure 4-12, where the green lines are the lines where the laser wrote along the sample, and the colored dots are the locations where the Raman spectrum was taken. The Raman spectra were then used to calculate the Raman ratio as described in section 3.5, and are plotted in the lower portion of the Figure, where the different points correspond to the locations where Raman was taken in the image above them. The region with the largest change in the Raman ratio was in the

darker portion where the center of the irradiation was. The lighter region to the left of this

saw much less irradiation, which is why less change is seen in the material.
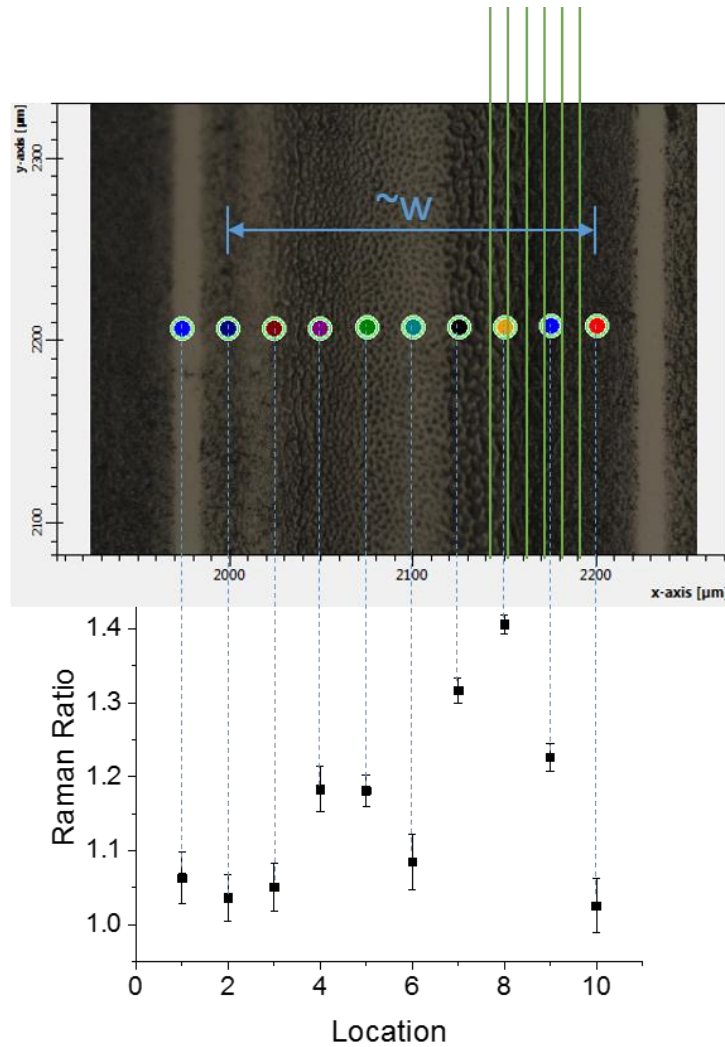
Figure 4-12 The green lines in the top image show where the laser was swept across the sample, with the beam waist depicted with the blue arrow. Raman was taken at the circular location, and the Raman ratios were calculated and are shown in the graph at the bottom.

The asymmetry of this modification was concerning as one would expect that this

additional modification zone should extend on both sides of the laser written area. This

non-uniformity was also seen in other irradiations that were performed. Also a two-lobed

structure was able to be seen in some additional irradiations with the idler output from the

OPO at 2μm that occurs concurrently with the 1.3μm output. Additionally the irradiances

for the onset of modifications did not track from day to day as can be seen in Figure 4-13

where the Raman ratios for irradiations from two different days are shown. Within a

single day though multiple irradiations tracked well with each other, which indicated

either the material is very sensitive, is non-uniform, or the laser profile is not repeatable

from day to day. As repeatable material response is needed in order to fully develop

GRIN optics, a secondary approach was investigated.
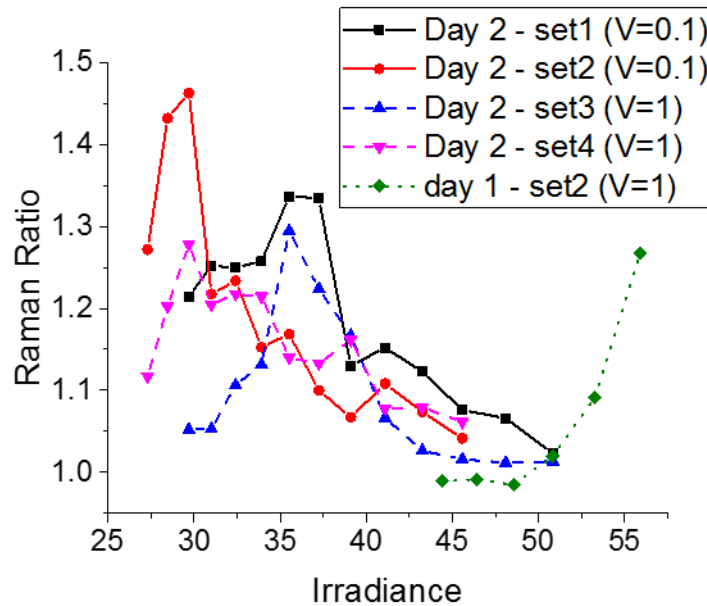
Figure 4-13 The Raman ratios were plotted for several different irradiation conditions on two different days.

The post-irradiated regions did not show a change in the crystallization without a

subsequent G HT, which means that the crystallization seen after the HT was solely due

to the HT that occurred, and there was no growth in the irradiated regions from the

irradiation. This showed spatial control of the crystallization state, and therefore

refractive index within the material. With the inconsistencies seen from day to day and

the non-Gaussian laser beam profile, a different approach and laser source was

investigated. This fs, MHz laser source was more suited to do the inverse process of laser assisted crystallization where a pre-cerammed material was re-vitrified into a glassy state, as it has the necessary conditions in order to have high heat accumulation in the material, which would take the temperature high above the nucleation and growth temperatures seen thus far.

4.4   Conclusions

The goal of being able to pattern GRIN structures in the material by spatially modifying the nucleation or growth in the material was investigated. The effect of irradiation on 40 mol% PbSe was investigated so that Raman results could be compared with data collected in section 3.5 on samples subjected to two step, furnace based, nucleation and growth thermal protocols. The first set of experiments looked into using the irradiation as a spatially varying, surface heat source for crystal growth. A gradient in index (aka, a GRIN structure) was created using a 532 nm, CW laser source to create a gradient temperature profile across the sample. Simulations were able to be performed in order to determine which experimental conditions should be used for the irradiations. Several samples were irradiated with slightly different irradiation conditions, which are later evaluated in section 6.1. One sample was further evaluated here, and was characterized with Raman spectroscopy. Varying amounts of crystallization were seen in this sample, with a decrease in the extent of crystallization from the center to the edge. From this data an expected temperature profile was able to be calculated and compared to the simulated temperature profile. Both of these temperature profiles were then converted into index profiles, which were then able to be compared as well. Both the temperature and index profiles were similar, and show a good first effort towards thermal modeling

for this method of heating, and that a spatially varying heat source could create a spatially varying degree of crystallization.

Next a pulsed source was used in order to see if it could be used to create index profiles that were less diffusion dependent. Initial work with a ns, 1.064μm laser source was performed on this composition in a growth-only regime. This sample was then evaluated with Raman spectroscopy to determine the GRIN profile in the sample using the relation determined in section 3.5. The sample was then polished along the axis of the input laser, to allow for a more full 3D measurement of the refractive index by performing Raman measurements at different depths inside of the sample. Simulations were also performed in order to determine if any laser-induced heating was likely occurring in the sample.

The ns, 1.064μm laser exposure was able to crystallize the sample and produce a GRIN that was able to be partially mapped out with Raman spectroscopy. The sample saw melting in the center of the irradiated region, with induced crystallization transitioning to only base glass around it. The melted area and the crystallization region immediately around it did not have Raman spectra that had been seen before, therefore the refractive index for that specific location is unknown. The melted region though resembles Raman spectra for base compositions with lower Pb-contents, or even higher amounts of As_2Se_3. This experiment showed the limitations of the Raman to index relation for spectra that are not able to be achieved through furnace HT. Further characterization of such spectra would need to be accomplished through μ-XRD or TEM. This sample showed a similar profile to the surface heat source with the CW laser, so a fs laser with a shorter pulse duration and longer wavelength was investigated next.

Lastly, a fs, 1.3μm source was then used on the same composition in order to determine if a heat accumulation effect would be able to be created, and if this would allow for laser-induced nucleation in this glass composition. The laser was focused above the sample surface, and then brought closer to the surface in order to vary the irradiance level of the beam on the surface without changing the laser output power. The samples were then investigated with Raman spectroscopy to ensure that no changes were occurring in the sample as a result of the irradiation alone. A subsequent growth HT, which was slightly below a temperature where spontaneous growth occurs in the material, was performed and the Raman spectra was then re-measured in the irradiated regions to see if growth had occurred, and therefore nucleation was induced by the laser.

The 1.3μm fs laser source was able to cause changes in the nucleation state, but the results were not reproducible from day to day and were accompanied by unwanted surface modifications. It was determined that nucleation of a sample with this laser would not be controllably accomplished, and that the laser did not have a Gaussian profile. An alternative laser source was assessed for its use in irradiations, and would likely cause high heat accumulation with its fs, MHz pulses. One result from this work demonstrated an interesting new idea for creating a GRIN material beyond the crystallization strategy investigated to this point. The potential for this source to be able to re-vitrifying a pre-cerammed sample by locally melting the crystallization already present in the material was investigated in order to have a better control of resulting GRIN profiles in the material. This strategy is investigated in the next chapter.

5   LASER-INDUCED VITRIFICATION

The experiments and results up to this point have shown how the use of thermal treatments with a furnace in combination with, or without exposure from lasers of varying pulse durations, can convert a fully amorphous starting material to a glass ceramic. Such induced crystallization to form a multi-phase glass ceramic that retains its transparency within the MWIR has been shown to be possible either following a homogeneous treatment (within a monolithic bulk sample) or across spatially defined regions within a single sample where variations in the extent of nucleation, growth and the resulting crystallization can be tailored through localized heating.

As a result of these studies and some of the limitations highlighted in Chapter 4 that were related to the choice of laser conditions and the lack of repeatability of material modification, an alternative strategy was identified to create a spatially varying amorphous/crystallized material that exhibits a transition in properties related to the transition between these two states. Specifically, we have investigated an approach converse to the laser-assisted crystallization technique that starts with a glass ceramic and selectively re-amorphizes it. We employ this approach to realize a gradient in properties and hence, refractive index, starting with a higher index composite converting to a lower index glass.

This strategy involves starting with a glass ceramic, and then creates an index modification by reversing the crystallization through melting of the precipitated crystals. Here the melting can be spatially controlled through the use of a laser beam, which is where the term laser-induced vitrification was coined. This re-amorphization results in the laser-modified region possessing a lower refractive index than the surrounding

131

material, instead of the previous gradient imparted through growing crystalline phases within a glassy material.

As discussed in section 1.6, heat accumulation which could be used to heat our glass ceramic, could be achieved using a laser that has fs length pulses at MHz repetition rates. As the temperatures needed for nucleation and growth of the $(GeSe_2\text{-}3As_2Se_3)_{60}PbSe_{40}$ composition used in section 3.4 have a narrow, well defined temperature range (~ 190-200°C for nucleation and 200-230°C for growth as determined by I-U curves), and timescales (for furnace heat treatment) on the order of 30-120 min for nucleation and 10-30min for growth, heat accumulation by fs irradiation may not easily thermally nucleate or grow crystals. A non-thermal effect, such as that seen using the ns, 1064nm laser (discussed in section 4.2.2), may be sufficient to impart the requisite energy dose as determined by post irradiation Raman spectra that showed crystal growth.

While the above paragraph discusses issues of the heat source in terms of time and temperature to create crystallization, a means to re-amorphize or remove crystallization employs localized changes in the previously partially crystallized material either by erasure of the pre-existing nucleation or growth that already exists in a glass ceramic sample. With knowledge of the melting temperatures of the crystallites in the glass ceramic and the absorption values of the material (glass in its parent form, modified glass with crystallization species depleted, and crystalline phases) at the laser wavelength of use, then the laser conditions that are needed to be used should be able to be calculated. This modeling though will not be utilized in this work as it was past the scope of this dissertation. This approach, to use a laser to locally induce a spatially varying index change/structured pattern via re-amorphization or controlled melting of a glass ceramic is

to the best of our knowledge, a novel and unreported technique. We have coined the name laser-induced vitrification (LIV) to describe the process whereby a region is returned to its vitrified or glassy state from a prior glass ceramic form. This chapter discusses the preliminary efforts to understand and utilize this technique on 40 mol% PbSe glass ceramic starting material.

An initial overview of the LIV process is first presented in this chapter. Two different fs lasers were evaluated for their potential to convert the glass ceramic back in to a fully glassy state in the material. For these studies, simulations were not performed, so the irradiation conditions that were needed to melt the crystals were experimentally determined. It was also assumed that all of the crystalline phases were able to be re-melted (or reduced). While this was confirmed visually through electron microscopy, we also utilized Raman spectroscopy to specifically track the evolution of the initially present As_2Se_3 phase.

In our efforts, LIV was used to produce an array of locations where we modified the number density of nucleation sites realized through a thermally induced pre-nucleation HT of 40 mol% PbSe material. Here, we used the 1.3μm laser (110 fs and 1 KHz) which was focused with a 25 mm lens to obtain fluences up to 0.144 J/cm^2 (144 W/cm^2) with the aim to erase the previously nucleated features. These samples were then had a furnace HT after exposure, which resulted in a measurable change to the Raman spectrum. This exposure and analysis protocol is similar to that used previously as described in section 2.14. The Raman spectrum of this sample was measured before and after a growth HT in order to determine if the nucleation state of the material was modified, as evident by the

change in the 246 cm^{-1} band and modification was quantified by calculating the Raman ratio of the modified region as defined in section 3.5.

With a change in the nucleation state confirmed through Raman spectroscopy, experiments were then performed with a separate 1 MHz, 1.03μm laser with 850fs pulses as described in section 2.14 to attempt to fully erase the crystallization in a sample of 40 mol% PbSe glass ceramic which had undergone a two-step HT (N+G) protocol of 190°C for 2hrs plus 220°C for 30min. This experiment irradiated a region of the glass ceramic, and the post exposure sample was evaluated once again using Raman spectroscopy to compare and quantify pre- and post-exposure Raman signatures, to allow for calculation of the change in the Raman ratio in the modified regions. As discussed previously, this tool allows for the quantification of changes from the glass ceramic state back towards the original Raman spectra as was seen for the parent base glass. Since the material is a partially crystallized glass ceramic realized from a known parent glass, the 'target' glassy state spectra is known. The comparison thus allows an estimate of conversion towards the glassy state enabling us to relate exposure conditions to the extent of re-amorphization. While Raman is a powerful tool providing excellent discrimination between crystal and glassy phases if the crystals are Raman active, a secondary tool can provide further validation. While we had hoped to use μ-XRD data for this purpose, it was unavailable for our use. Thus electron microscopy was used as a more qualitative indication of conversion of all of the crystalline states. The outcome of our experiments to demonstrate the possibility of LIV and the general aspects of its application to our 40 mol% PbSe glass ceramic are discussed in subsequent sections following a brief background on related approaches in literature to LIV.

5.1   <u>Background</u>

Laser-induced vitrification, or more specifically, the use of a laser in the melting, processing, or modification of a glass or glass ceramic, can mean different things depending on its specific application and goal. Examining the literature on this topic, there are several processes that are similar to what is being done in the present study, but are still fundamentally different from that attempted in the re-amorphization study on optical glass ceramics.

A review of prior efforts shows that the laser-induced melting of raw materials in order to create glasses has been explored. This processes is typically used in composition spaces where either the refractory nature of the raw materials or excessive melting temperatures and choices of crucibles prevents the complete melting of starting materials, thus the glass would not be able to be formed otherwise. This process is sometimes called 'container-less melting' and has sometimes employed levitation to suspend the melt during irradiation [128]. Laser melting of glass has also been used with additive manufacturing methods, where glass powders are locally melted in order to build up a final part [129]. Laser marking by vitrification has also been performed, where marks are made on non-optical components by locally melting the material [130]. Laser surface vitrification, where a thin surface layer of metal is melted in order to create a surface layer with different material properties than the rest of the bulk, has also been studied [131,132]. Most similar to what we are proposing are phase change materials (PCMs), where under an applied field (either from a voltage source or a laser) the material switches from a fully amorphous to a fully crystalline state. While studied extensively over the past several years, infrared PCMs generally are formed in thin film geometries [133]. Our work on the other hand, does not aim to create a change in phase that is

switchable, rather, we aim to tune the degree of the crystalline phase locally in a spatially controlled way to impart a variation in the crystalline volume fraction (from the maximum post HT'd starting state, to zero). Additionally, we aim to be able to do this in our glass ceramic, in either bulk or film form.

In the context of the present effort and as noted above, we have employed LIV to partially amorphize a previously crystallized composite material (40 mol% PbSe glass ceramic). Here, we use the laser to locally elevate the temperature within the laser exposed region, to return the exposed area to a glassy, crystallite-free state. As the laser has a non-zero absorption in the glass ceramic, exposure results in a local increase in the temperature of the glass ceramic up to or above the melting temperature of any crystals already present in the material. These melting points as measured with a DSC for the composite, are shown in Table 5-1 below for the individual crystal phases which could be used to estimate the necessary laser irradiation dose to realize necessary specific heating levels through simulations. If the temperature range of the DSC scan is increased above any exothermic crystallization peaks, an endothermic peak (dip in the data) can be seen, which relates to the melting of the specific crystalline species present in the material. The actual melting temperature of the crystals within the glass matrix would likely be slightly lower as they are surrounded (fluxed) by the already softened glass. Laser heating above these melting temperatures followed by rapid cooling (quenching) would locally modify the local area's thermal history resulting in a modified, re-amorphized glass. This process, while specific to our multi-component glass ceramic, is not dissimilar to the re-amorphization process that takes place in commercial Ge-Sb-Te (GST) phase change materials found in DVDs.

136

Initial studies on our glass ceramic have shown that by using a fs laser with a MHz RR, this can be accomplished on a local scale that would allow for a 2-tone index pattern to be realized on the μm scale. This localized melting could be used similarly to LIC, and is depicted in Figure 5-1 below in order to create patterned index profiles. For the material used here, the irradiated area created a negative refractive index change (as the glass has a lower index than the glass ceramic), which is the opposite of the patterning used in the earlier chapters of this document.

Table 5-1 The melting temperatures for the crystalline species found in the 40 mol% PbSe glass ceramic are shown in the middle column.

Crystal Species	Melting temperature (°C)
PbSe	1,078
As2Se3	680
Se	221
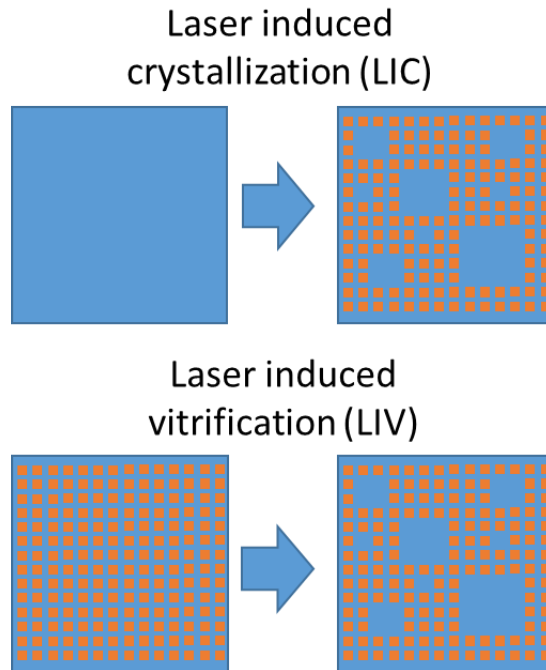
Figure 5-1 Comparison of laser-assisted modification strategies used in this work. LIC, as seen on the top takes a base, or pre-nucleated, sample and then selectively grows crystals in certain locations. The reverse of this process, LIV, takes a pre-cerammed sample and then selectively re-vitrifies exposed regions in the glass ceramic back to a glass.

This process has several benefits and shortfalls as compared to LIC. One benefit of

the technique is that there are a wider range of temperature conditions that will still allow

for LIV to occur, which causes the irradiation conditions to not be quite as stringent and

allows for more misalignments in the system and/or long term power variations or shot to

shot noise in the laser source used. Additionally, not as much fore-knowledge or

experimentation is needed when switching to new materials, as finding a melting

condition can be easier than trying to find a specific temperature range for nucleation or

growth as each composition has its own unique kinetics for crystallization.

5.2   Laser-induced removal of nucleation – experimental

The first effort towards LIV used the fs, 1.3μm laser discussed in section 4.3 to try to locally reduce the number of crystal nuclei sites in a pre-nucleated sample. In order to validate the change in the nucleation the sample could then have a growth HT performed to see if there was preferential growth in the regions that were not irradiated. As melting conditions were able to be found for the base 40 mol% PbSe glass during irradiation with this laser, it was thought that causing the surface to melt and then quickly cool might quench the material without nucleation sites in the irradiated region if the temperature was high enough. Also since the bulk 30 mm diameter samples were more phase separated than the 10 mm diameter samples, and the films are completely amorphous, there was a potential in this composition to also reduce the amount of phase separation already present in the base glass if the quench rate after melting was sufficiently high.

The sample used for this effort was a piece of a 400g, 30mm diameter, 40mol% PbSe glass as was used in section 4.3, where the samples were commercially polished. The sample then went through a nucleation step using the same muffle furnace as in section 3.1 at 195°C for 2hrs. The sample was then irradiated with the 1.3μm laser used in section 4.3 with the same rectangle pattern used before with a pitch between the lines of 0.01mm, and 6 lines were written for each irradiation condition. The focus of the laser started 7.7mm below the surface and was moved up to 2.3mm above the surface in steps of 0.2 mm. A total of 36 different irradiance values were tested and the fluences seen by the sample were 0.085 to 0.144 J/cm^2 (85-144 W/cm^2), which were chosen so that they would cross from below to above the ablation threshold of the material. This was done to subject the material to temperatures sufficient to dissociate the nuclei already present in the material (believed to be on the order of several atoms in size), while trying to stay

below the ablation threshold of the material. Raman spectroscopy was performed on the samples to confirm that the nucleation HT and laser irradiation did not result in crystallization in the sample.

A growth HT was then performed on the specimen at 230°C for 10min. The short HT time was used in order to inhibit additional nucleation (230°C is outside of the regime of a measurable nucleation rate) or spontaneous random growth in regions with less nucleation. Raman spectra of the samples was acquired post-HT, and were used to quantify the pre-/post Raman ratios for each modified location as described in section 3.4. Visible images were also obtained from the Raman spectrometer to be able to visually see what kind of microstructural modifications were occurring. White light interferometry was used to measure the surface profiles of the modified region. With these tools defined, they were used to evaluate both the pre-nucleated glass following irradiation to ensure there was no growth from the irradiation alone and in post-HTd samples to determine the changes in the number density of nucleation sites in the material from the irradiation evidenced by different final crystallization states.

5.3 <u>Laser-induced removal of nucleation – analysis</u>

A 1.3μm laser source was used in order to modify the amount of nucleation present in the material. With an additional G HT after irradiation an index modification would be obtained in the regions with altered nucleation. This change could be measured using Raman spectroscopy to determine the resulting amount of crystallization present locally in the glass.

The first characterization of the material post-irradiation was with a visible microscope on the Raman system, which was used to image the irradiated regions and is

140

shown in Figure 5-2. This was done to see which irradiation conditions caused unwanted

surface ablation. The modifications ranged from almost no discernable change up to

ablation trenches, which occurred when the sample focus was closest to the surface of the

sample.
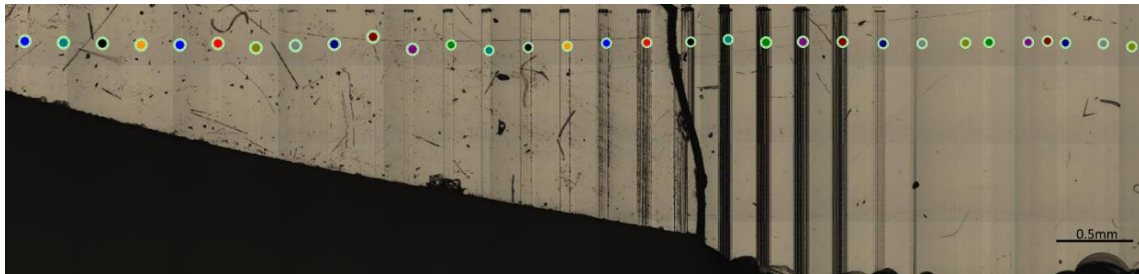
Figure 5-2 White light images were taken post HT+laser+HT. Raman spectra were
taken at each of the circles.

Raman spectroscopy was performed at each of the circles in Figure 5-2 for both the N

+ laser and N + laser + G conditions. No changes were observed after the irradiation

before the post-HT. The spectra for the N + laser + G regions were used to calculate the

Raman ratio for each location as seen in Figure 5-3. The Raman ratio region from ~1-

1.05 is what is normally seen for base samples of this material, and above ~1.6 is

normally what is seen for a fully grown sample. These regions are depicted in the figure

in green. The ratios found for the irradiated locations fell in between these two endpoints,

and have a gentle transition between a partial growth spectra to a base glass spectra. This

shows that as the fluence was changed from 0.114 to 0.085 J/cm^2 (85-114 W/cm^2), the

amount of nucleation present in the material was reduced, which caused less growth

during the G step as compared to a non-irradiated region. As there was still thermal

growth after the irradiation, there is high confidence that the Raman ratios found in this

experiment can be directly compared to those found in section 3.5.
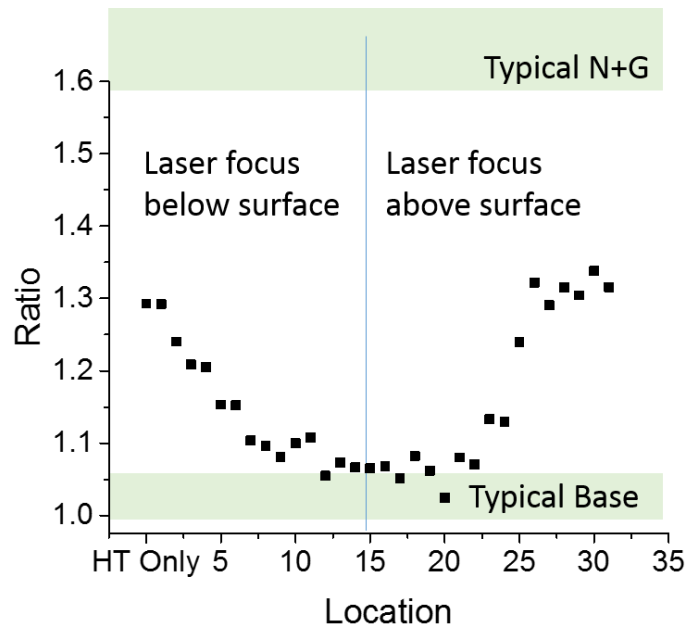
Figure 5-3 The Raman ratio is shown for each location that was HT+L+HT and was seen to have visible modifications so that it was identified. The ratio values that are normally seen in a base 40 mol% PbSe sample and a high N+G sample are shown in green for comparison.

An alteration in the nucleation state in the material was able to be seen in a pre-nucleated 40mol% PbSe sample after laser irradiation. A decrease in the number density of nucleation sites was able to be observed through lower growth seen after a post-irradiation + G HT than in areas where the pre-nucleation was still present in the material. This showed that LIV of nucleation was likely able to be achieved. The LIV process could potentially be used to erase ceramization already present in a glass ceramic. This process would have the added benefit of not needing a post-irradiation HT that would potentially necessitate post-HT processing through polishing or further forming of the optic.

5.4   Laser-induced removal of growth – experimental

This approach was extended to use laser exposure to reduce the crystal growth already present in a material. Here, a two-step HTd glass ceramic sample was exposed with the objective to locally melt the crystalline phases present by employing a focused laser. As with the previous section on LIV the post-irradiated samples were able to have their crystallization state measured through Raman spectroscopy. Additional characterization with WLI and visible microscopy was also performed in order to determine if there were any changes in the surface topography or any surface damage from the irradiation. Lastly TEM and SAED were used to confirm changes in the degree of crystallization of the material post-irradiation.

One limitation observed in the prior effort to reduce nucleation present in the samples is that the maximum amount of index change between nucleated and un-nucleated material post-HT is very small as compared to the refractive index variation between base and fully grown material as seen in Figure 5-4. Here, the horizontal light blue line at the bottom of the figure represents the base glass' index as measured at $\lambda = 4.5\mu m$ (3.039), and the refractive index change with two different nucleation temperatures for the indicated growth temperatures are seen. As discussed in chapter 3, a larger shift is seen in the amount of growth at a specific growth temperature for samples with more nucleation. If different regions of a sample have different amounts of nucleation, after the whole sample is grown the change in refractive index seen is based on how much more growth is induced in that region. A method that would ensure a greater possible index change would be a change in the amount of growth seen in the material. By achieving this with

LIV, it also eliminates any needed polishing after irradiation to remove sample deformation from a post-irradiation HT.
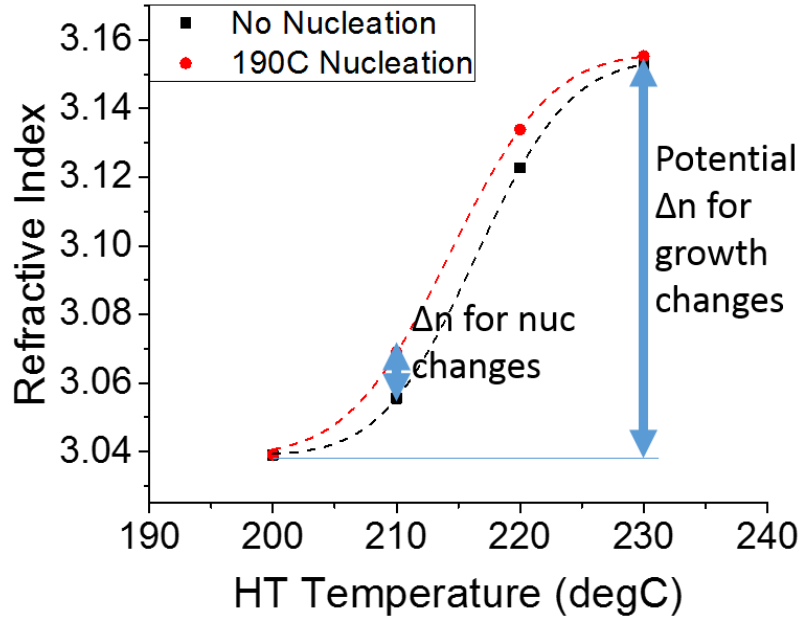
Figure 5-4 The maximum allowable change in refractive index with multiple nucleation states with the same G HT, and the potential index change between a fully grown and fully glassy state (as indicated by the lower blue line) for a 40mol% PbSe sample measured at λ=4.515μm.

Using DSC data which indicates the endotherms for crystalline species in the 40 mol% PbSe glass are below the 1% weight loss point, the glass should theoretically be able to be heated to a high enough temperature, and then be quickly cooled in order to return it to the glassy state without changing the glass composition. These temperatures are listed in Table 5-1.

This study used the 1.03 μm laser source described in section 2.14. The location of the focus with respect to the sample surface was determined by focusing the back reflection of the beam into a camera and the sample was translated axially along the beam until the smallest diameter beam was seen on the camera which would correlate to the

laser focus being in the plane of the sample surface. This was performed at different locations across the part in order to have the sample flat (perpendicular to the laser axis) so that all locations in the irradiation would have the same fluence.

The first set of exposures were rectangles similar to those described in section 4.3, but with the focus inside of the surface instead of above it. The sample was a piece of a 30mm diameter from one of the 400g melts of 40 mol% PbSe that was commercially polished as described in section 4.3. The sample was pre-HT at 250°C for 17.5hrs. The pitch between the 10 lines written for each condition was 0.01mm with a write speed of 1mm/s. The total length of the line was 3mm. The step in the z-direction was 0.01 between the different rectangles. Seventeen of these rectangles were created spanning irradiances of 9.65E-4 - 2.876E-3 J/cm^2 (965-2876 W/cm^2). These rectangles were used to determine which fluences would be able to produce LIV in the melt. This could be verified by having the Raman spectrum return back to that of the base glass. We believe that this change in the Raman signature would indicate that there is a change in the crystallization state as seen in section 3.5, and additional confirmation will still need to occur with μ-XRD.

Post irradiation, these locations had their Raman spectra taken, as described in section 2.6, for multiple points within the irradiated region in order to assess whether the LIV evenly changed the starting glass ceramic back into the base glass. The Raman ratio for each point was then calculated as described in section 3.5. White light interferometry as described in section 2.12 was also performed in order to determine if any expansion or contraction was seen in the material from the exposure.

A second set of exposures were also performed with the same laser using a different write geometry. In previous attempts with both the laser used in this section and the 1.3μm laser used in the erasure of nucleation, there did not appear to be any modification into the bulk of the material as both of these lasers have significant absorption in the material. In order to try to alleviate this problem, a different irradiation pattern was used with the hopes of having more of the laser intensity, and therefore heat, penetrate down into the bulk of the material as there was not access to an ~100fs, ~1MHz RR laser at longer wavelengths. As the sample was converted back to the base glass the SWCO should shift to lower wavelengths, so as the laser focus moved from in the bulk up the surface of the material the surface of the material could vitrify and potentially allow more light to penetrate into the bulk of the material as the focus was moved back further into the sample.

This pattern of arrayed columns is depicted in Figure 5-5, where the red line is the location of the focus through the sample, and the blue arrows depict the direction the focus is moving. This pattern forms a series of pillars that are connected in the bulk of the material. The focus is first placed 1 mm further into the sample than would normally create surface modification and it is translated in the same plane to the location where a pillar will be placed. The beam was then brought 1mm closer to the surface and then was brought back down 1mm to the starting height. The focus was then translated to the location of the next pillar and the cycle was repeated. The pitch between the different pillars was 0.01mm, and a total of 20 by 20 pillars were made. This protocol was employed to allow for heat to further penetrate into the material as described in the paragraph above.
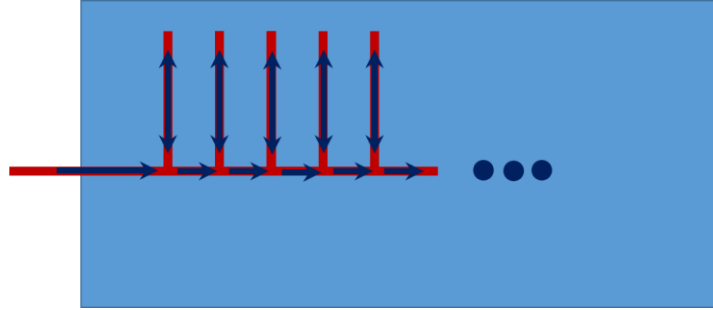
Figure 5-5 The geometry used for 1030nm, MHz irradiations is shown. The red line if the focus of the beam, and the blue arrows depict the direction of travel. A series of irradiated "pillars" is made in the material though this technique, and are used to try to achieve modifications in the bulk.

Post-irradiation, the Raman spectrum was taken of the irradiated surface. A scratch was then induced in the irradiated region, and the Raman was taken in the scratch to determine if there was modification into the bulk of the material (sub-surface). The sample was then scratched again and the Raman was re-taken in order to see if the further depth still had modification. A secondary irradiation region, where the focus was slightly closer to the surface, was also scratched, and the same process was used to determine if there was modification into the bulk. White light interferometry was also taken in order to see what the depth of the scratch was in order to estimate the depth of the modification, and to see if there was any expansion of the material. Lastly, TEM/SAED was taken on a larger, yet similarly irradiated region in order to determine if the degree of crystallization was modified as a function of depth post-irradiation. With these tools defined, they will be applied to a pre-N+G glass ceramic that will then be characterized to determine the changes in the amount of crystallization present in the material from the irradiation.

5.5   Laser-induced removal of growth – analysis

Samples were irradiated with the intention of changing the degree of crystallization present in the material though LIV. This change in crystallization was able to be

characterized with Raman spectroscopy. We believe that this change in the Raman signature would indicate that there is a change in the crystallization state as seen in section 3.5, and additional confirmation will still need to occur with μ-XRD. Confirmation of a change in the degree of crystallization was able to be achieved with TEM/SAED. Additionally visible microscopy and WLI were used to determine if any physical modifications were observed on the sample surface including expansion or damage due to the irradiation.

The visible microscope on the Raman system was first used to characterize the initial test rectangles to determine which irradiation conditions stayed below the ablation threshold. From this it was seen that the conditions spanned from no-modification to what looked like possible melting of the glass, where a slight discoloration as can be seen in the right of Figure 5-6. The green circles in this image are the locations that Raman was later taken on the sample. Using the New View and WLI of the samples to probe the post-exposed sample, a slight expansion of the material was seen for most of the conditions, except for the highest power ones which saw a slight decrease in height from ablation. The slight increase in height would be indicative of slight photo-expansion. As this could also create a change in the refractive index, the Raman spectrum of the glass was also investigated to ensure that the shape of the Raman spectrum returned back to that of the base glass, and therefore an index change from the change in the crystallization state would be produced. If the irradiated region also saw a decrease in the density to below that of the base glass, the material could then create an even larger change in the refractive index.
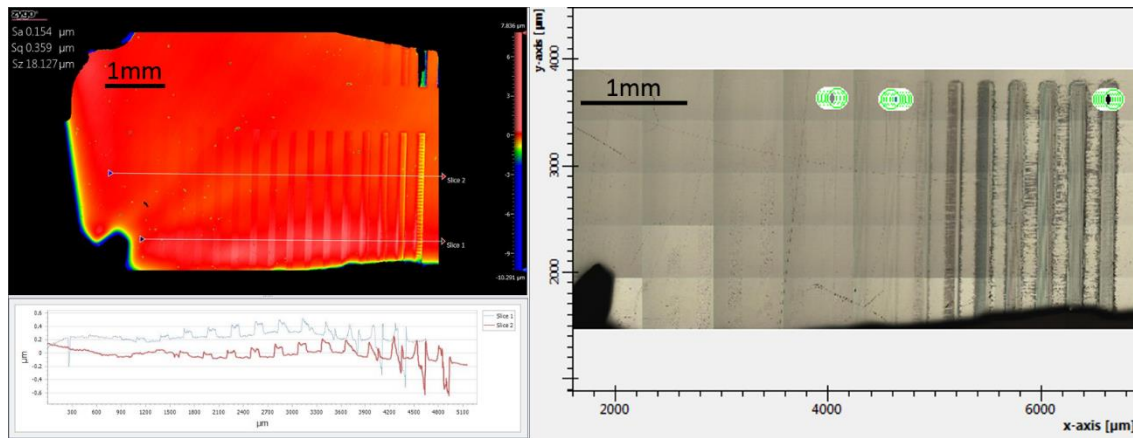
Figure 5-6 WLI and a cut-through of the measured profile for a LIV of nucleation + post-HT is seen on the left. Right is a visible image of the same sample, with the green circles indicating the strips where Raman was measured. Scale on images are shown

Raman microscopy was performed on three of the irradiated regions in the pre-cerammed glass ceramic in order to determine if the Raman signal returned to that of the base glass. The micrographs on the left of Figure 5-7 show zoomed images of these regions, which consisted of areas modified by different irradiation conditions. Three different sets (denoted by 1, 2 or 3 in the legends) were investigated. Set 3 had an exposure fluence of 1.323E-3 J/cm^2, whereas set 2 had a fluence of 1.031E-3 J/cm^2, and set 1 had fluence of 9.65E-4 J/cm^2. The dots in the images to the left are the locations where the Raman spectrum was measured, and their locations are labeled as 1-7 in the micrograph, and are correspondingly labeled in the Raman spectra plotted on the right in Figure 5-7. It was seen that the Raman spectrum post-irradiation were able to return to that of the base glass. A sharp change in the shape of the Raman spectra is seen at the edges of the irradiated regions, where only Raman spectra for high growth or Raman spectra for base sample spectra are observed with no middle state in between. Set 2 does have a small amount of variation in the shape of the Raman spectra on the edges, where there is a slight decrease in the peak around 246cm^{-1}, and as discussed in section 3.5, this

149

suggests that there are small amounts of crystallization in the material. Also in set 3 there

is a slight shift in this peak to lower wavenumbers, which is likely due to the

discoloration and some amount of melting which was seen in section 4.2.2 to have the

246cm^{-1} peak have its peak shifted to slightly shorter wavenumbers, and have a higher

intensity with respect to the fist peak around 200cm^{-1}.
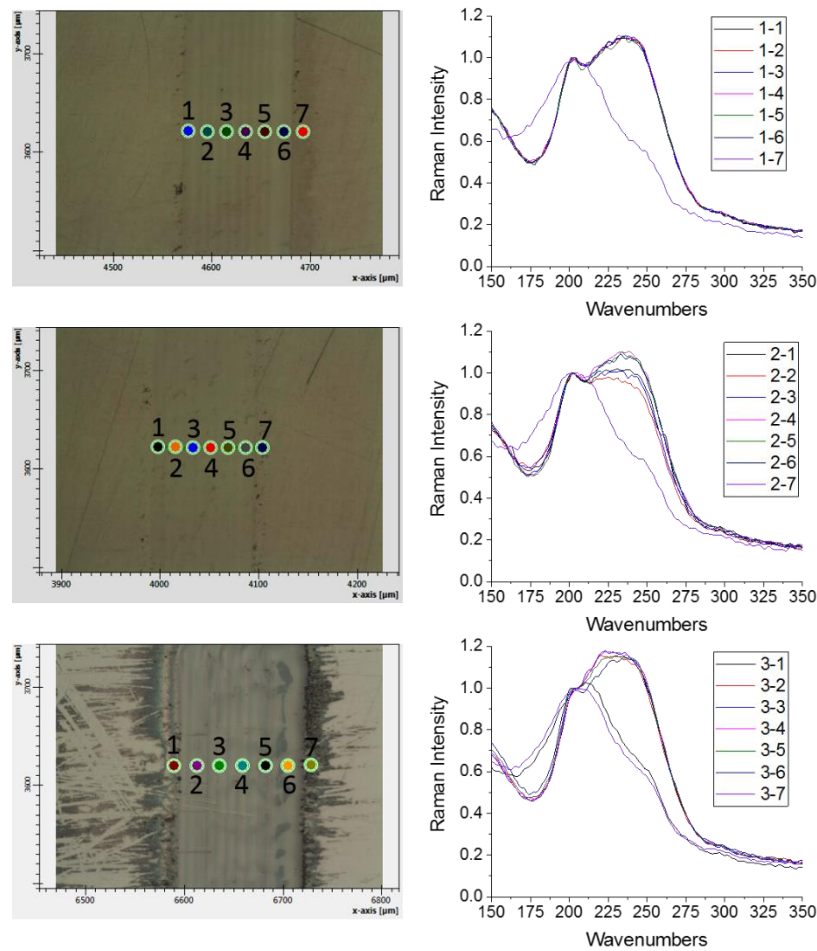
Figure 5-7 Optical micrographs (left) with scale shown (in μm's) for three different irradiated areas of a N+G sample (190-2hrs + 220-30min) sample exposed with varying irradiance levels (λ = 1.03μm) ranging from 9.65E-4 - 1.323E-3 J/cm^2 (965-1323 W/cm^2). The numbered circles in the micrographs correspond to the Raman respective spectra in the overlaid spectra depicted at right.

Next the pillar written geometry was investigated. For the LIV of crystallization with

a pillar-written geometry, visible images from the Raman system are shown in Figure

5-8. The pitch between the columns appears to have them just touching one another as seen in A. The irradiated region was then scratched in order to determine if the modification was able to be seen in the bulk of the sample, or only near surface. The first and second scratch can be seen in B and C respectively. The colored dots in each image correspond to the locations where the Raman spectra were taken. The fluences for A-C in Figure 5-8 were 6.4E-5 - 1.42E-4 J/cm^2 (64-142 W/cm^2, the range given is the fluence value at the sample surface for the laser focus at the top and bottom of each pillar), and for D was 9.1E-5 - 1.833E-3 J/cm^2 (91-1,833 W/cm^2).
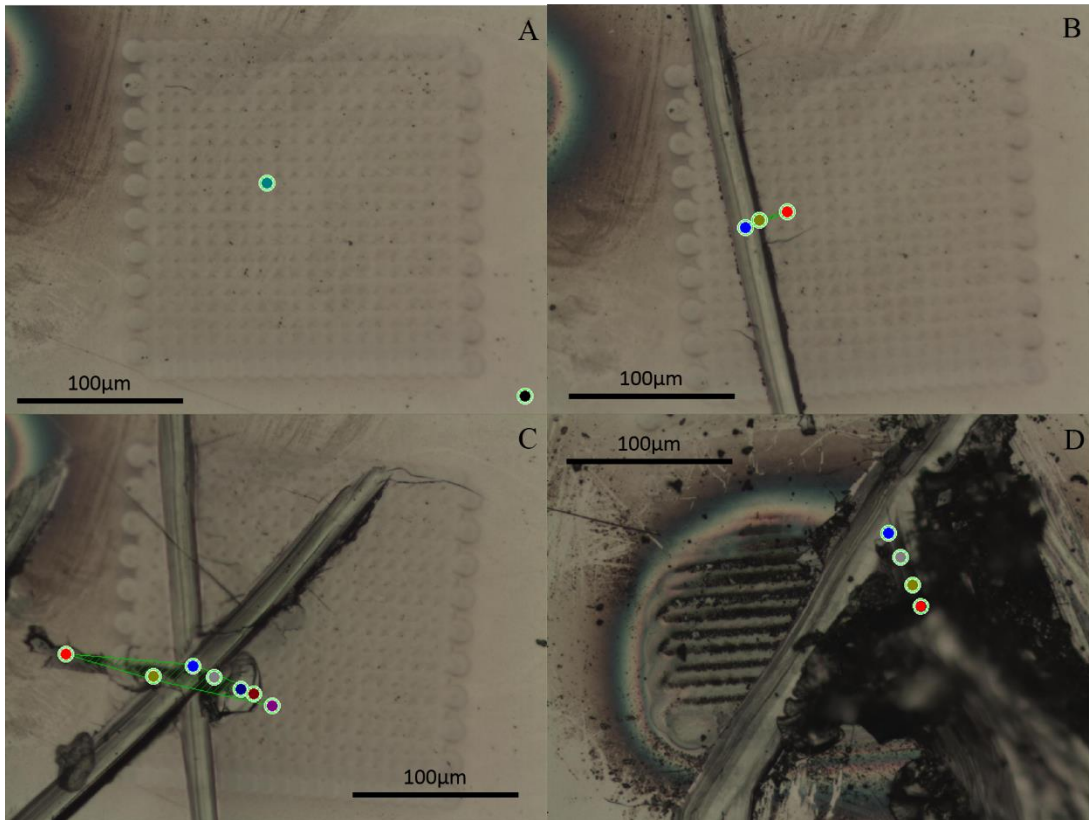
Figure 5-8 The irradiated region with "pillars" is seen on the top left. The first scratch is seen in on the top right, and two scratches is seen on the bottom left. The bottom right is a second region, which had a bigger chip removed than either scratched area. For all the images the circles are where Raman spectra was measured, and were imaged at the same scale.

The Raman spectra for the different locations is shown below in Figure 5-9. There is an obvious difference in the un-scratched spectra between the irradiated region, which appears the same as a base glass sample in section 3.5, and the un-irradiated region, which showed a grown spectra. This shows that indeed LIV of a glass ceramic was able to occur. The spectra after one scratch shows little variation from the un-scratched, sidewall, and bottom of scratch regions. The spectra after two scratches shows mostly vitreous spectra, except for the edge wall of the second scratch (grey circle in Figure 5-8), and the location outside of the irradiated region, but still fractured (red circle in Figure 5-8). The Raman of the secondary irradiation region also showed some amount of LIV. These Raman points go from blue to red in the image of Figure 5-8 corresponding to spectra A-D respectively in Figure 5-9. As the depth was increased, a decrease is seen in the peak around $246 cm^{-1}$, indicating a greater amount of crystallization in the measured region. This would follow the assumption that the modification should trail off further into the sample.
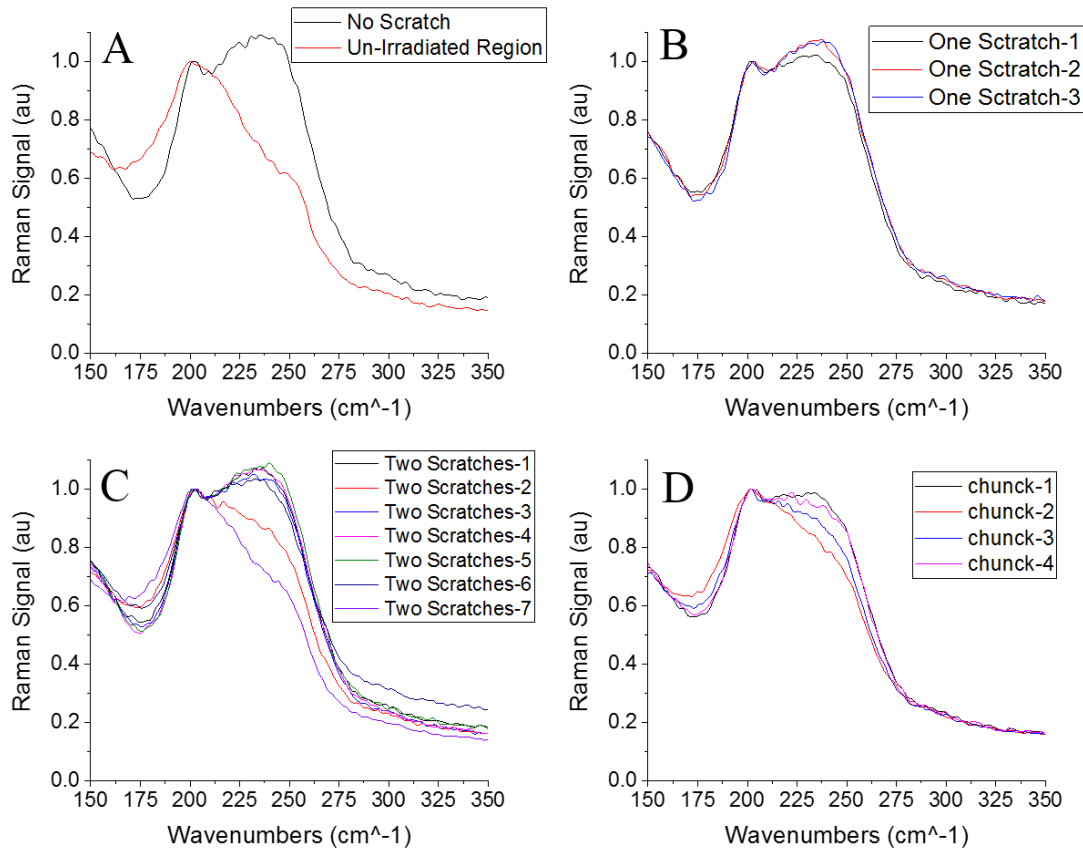
Figure 5-9 The Raman spectra are shown for the different location on the irradiated (A), scratched (B), two scratches (C), and chunk removed (D) samples that were shown in Figure 5-8. A-D correspond to the same location in both figures.

Also graphed is the depth profile of the two scratches where the Raman spectrum was taken, as well as the secondary region and is seen in Figure 5-10 below in order to determine the depth in the sample that the Raman was taken. The first scratch was approximately 2.5 μm deep, and the second scratch was closer to 4μm deep. The chunk that was removed slowly dropped about 4μm, and then steeply dropped another 9μm. This allowed us to confirm that some modification was able to penetrate into the sample.
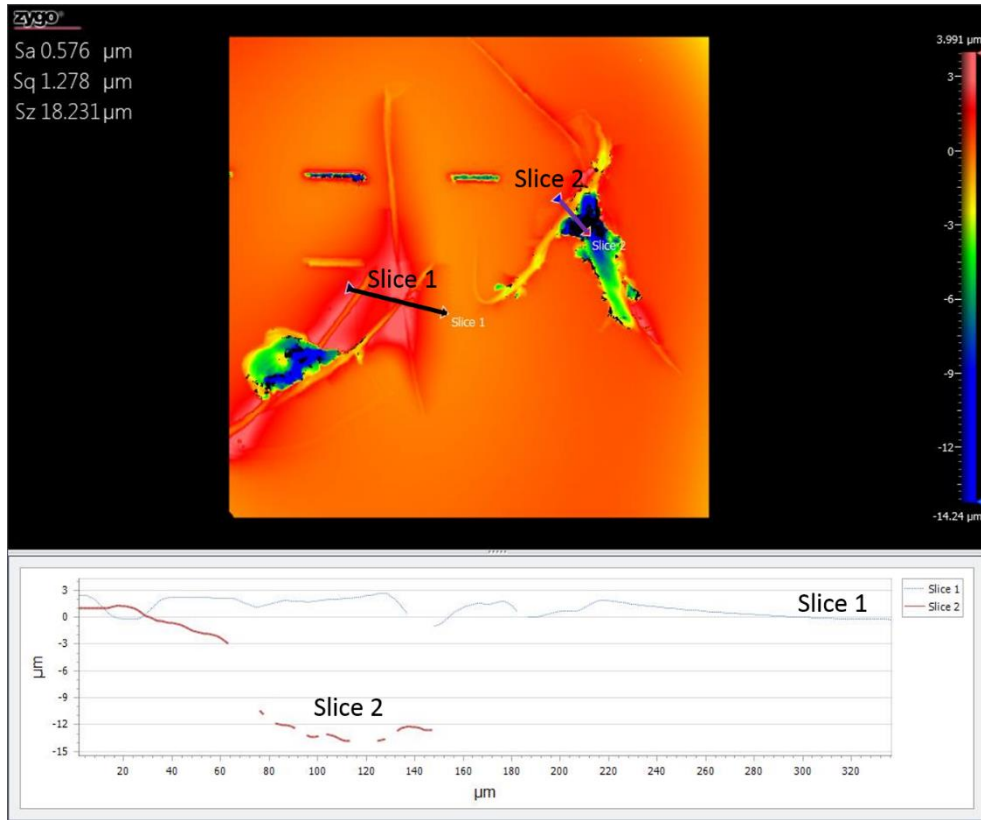
Figure 5-10 The depth profiles for the scratched areas of a laser-exposed pillar structures of pre-cerammed glass ceramic where Raman spectra were taken. The fluences for these two regions were 6.4E-5 - 1.42E-4 J/cm^2 (64-142 W/cm^2) and 9.1E-5 - 1.833E-3 J/cm^2 (91-1,833 W/cm^2) that Shown here (top) is the surface profile with the two slices that were taken indicated and (bottom) are the depth profiles. Measurements of the surface profile were taken along these depths in order to determine how the Raman spectra changes throughout the bulk of the material.

A similar irradiation was performed over a larger region with 32E-5-1.50E-4 J/cm^2 (32-150W/cm^2). A focused ion beam was then used to create a lift-out for imaging with the TEM as described in section 2.4. This lift-out was performed in order to determine the microstructure of the sample at different depths from the surface. The bright field TEM image shown below in Figure 5-11 shows three distinct regions in the material, where the darker regions in the image have more heavy atomic radii (Pb-rich region) or crystals. Insets of the SAED and higher magnification images are shown to the left for these three regions. SAED patterns were also taken in order to probe the crystallinity of

the material, as crystalline spots and diffuse rings are due to the crystal and amorphous phases respectively. The greater the crystallinity the brighter the spots, and the dimmer the diffuse rings. The top region shows the most crystallization as seen with the most distinct crystalline spots in the top SAED pattern and the asymmetric features (likely due to As_2Se_3 containing crystals) seen in the TEM image. The middle section is a transition region, where the SAED pattern has less distinct spots, and the secondary phase in the TEM turns from mainly asymmetric crystals to mainly symmetric Pb-poor droplets in a Pb-rich matrix which would be expected in the base glass. The bottom region has the least distinct spots and most amorphous rings in the SAED pattern, and the TEM image resembles that of the expected phase separated glass. This shows us that as we go further in the material there is a decrease in the amount of crystallization in the material. The reason that the top region has a higher degree of crystallization then inside of the material, despite the fact that the material is highly absorbing, may be that the focus of the laser was close enough to the sample surface that the peak intensity of the laser was slightly below the surface. This could have caused just high enough of an intensity in the bulk for the crystallization to decrease, and this intensity decreases closer to the surface where the intensity was below where the crystals would melt. As the absorption value of the material at this wavelength is at the detection limit of the UV-VIS spectrometer used in this study, the actual location of the most intense irradiation is currently unknown.
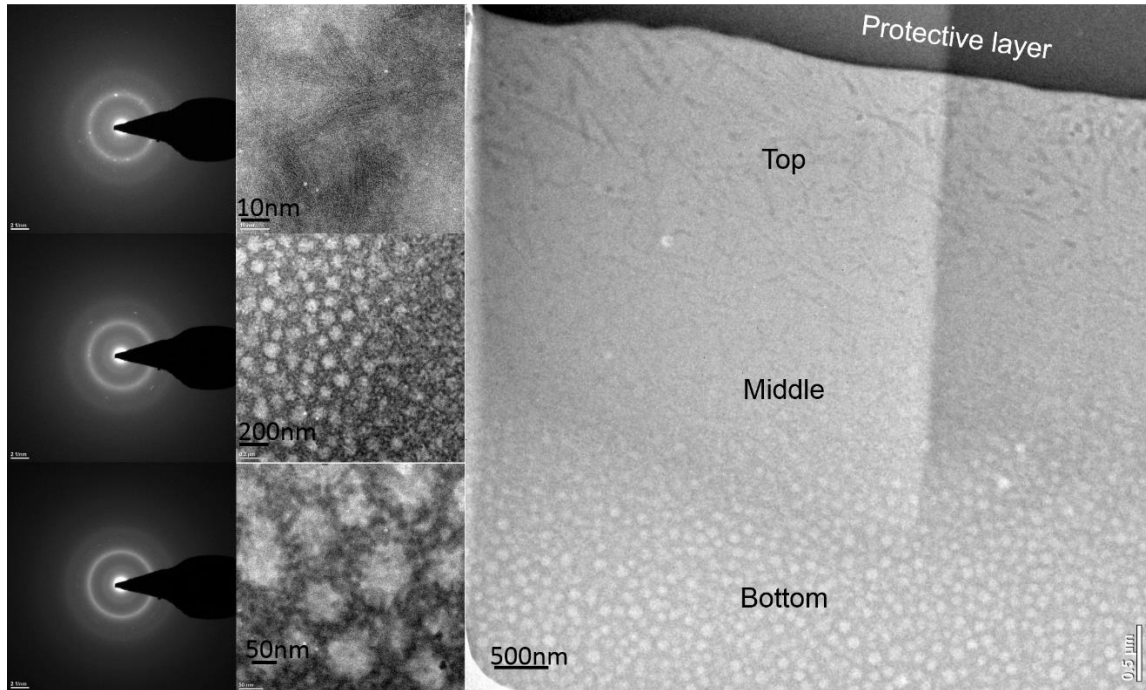
Figure 5-11 Bright field TEM images and corresponding SAED patterns were collected from the top, middle, and bottom regions of the FIB-fabricated cross-sectional TEM specimen.

Through all of the irradiation conditions explored in this part of our study it was seen that within the spatial limits of the tools employed, laser-irradiation regions of the 40 mol% glass ceramic investigated were successfully used to convert a glass-ceramic into glassy state as characterized with Raman spectroscopy, TEM, and SAED. A slight surface expansion was observed for the different conditions of the sample in Figure 5-6, which could impact our ability to quantify index changes in the irradiated areas. Additionally, the modifications were seen to be only near surface modifications as was evidenced through the cracked region. Though the use of a similar laser source with a longer wavelength writing further into the bulk of the sample should be possible.

156

5.6   Conclusions

LIV has preliminarily been shown to demonstrate that laser-exposure could be used to re-amorphize glass ceramic and to show that either the nucleation or growth state of 40mol% PbSe samples could be changed, resulting in an ability to spatially tune either a pre-nucleated or pre-grown sample back to the base glass state. Further characterization with μ-XRD is needed in order to confirm that all of the crystal types were affected as SAED was only able to show that there was a reduction in the total amount of crystallization. Post-nucleated samples exhibiting lower growth post HT + laser + HT (as defined by Raman spectroscopy) which indicates that the pre-existing nucleation was able to be removed with a 1.3μm, fs, KHz laser, which showed preferential growth in areas that were not irradiated post-growth HT. As the post-HT material had a potential smaller change in index than from the base glass to a fully crystallized sample, LIV of a pre-crystallized sample was also investigated. Crystal growth was able to be reduced with a 1.03μm, fs, MHz laser source in this pre-cerammed material where SAED patterns were able to show a gradient in the degree of crystallization in the material with distance into the material. Ideally if the laser was in the transparency range of the material, then controlled writing into the bulk would be able to be attained.

6   FABRICATION OF GRIN OPTICAL ELEMENTS AND DEMONSTRATION OF OPTICAL FUNCTIONALITY

Using what we have realized on the materials and mechanisms explored so far, we have fabricated and shown optical functionality through LIC and laser-induced vitrification. Specifically, two types of optical functionality were selected to demonstrate the utility of these materials and the processing methodologies developed in this dissertation. First a refractive, focusing optic based on 40 mol% GAP-Se base glass using a furnace to nucleate the sample, and a CW above bandgap energy laser to grow the sample was made in order to have a measurable focal length in the IR while still maintaining its transparency. Secondly two diffractive elements (diffraction gratings) were made where one was fabricated using laser-induced crystallization, where a laser was used to crystallize a pre-nucleated sample and then grown with an above bandgap energy pulsed laser, and the other was fabricated using laser-induced vitrification, where a sample was pre-cerammed with a furnace N+G HT and then was converted back to a base glass with a pulsed bandgap laser. Discussed in this chapter are the specifics of the methods used to form each element, and the characterization of the post-processed optical function as well as the refractive index profile as quantified with Raman spectroscopy.

6.1   Laser-induced crystallization focusing optic

A focusing optic was created using the 532nm laser source as described in section 4.1.2. This used an above bandgap energy laser in order to create a spatially varying surface heat source that would then cause a spatially varying heat source throughout the sample. Several laser irradiation conditions were performed in section 4.1.2, with the 532nm, CW source and were further characterized here with Raman spectroscopy and by

measuring the focal length of one of the samples. Only one of the resulting samples was further characterized with Raman spectroscopy in that section, but here that sample along with the others were further characterized for their ability to focus light. As a reminder, the different irradiation conditions that were used are included in Table 6-1. These samples, including the one that was later cross-sectioned for the Raman evaluation in section 4.1.3, had their approximate focal distances estimated. The minimum beam waist and focus location was then further characterized on one of the more promising samples.

Post irradiation, the samples were evaluated for their approximate focal length, and the sample partially characterized in section 4.1.3 had its focal length and minimum beam waist characterized with a 2μm laser. A FLIR SC7000 MWIR camera was used for an initial visual inspection to assess if any index modifications were created by the irradiation. The camera was also used to do a course estimate of any potential focusing effect from the GRIN structure. The focal measurement was performed by placing a grid behind the sample, and then moving the grid further away until it came into focus looking through the sample with the camera, while the sample was in focus in the camera. These initial evaluations of the focal length are shown in table 6-1. Repeatability was evaluated for two different irradiation conditions on two samples each. The repeatability of the estimated focus for these samples was very good.

Six of the irradiated samples showed focusing behavior and did not crack. An initial visual inspection was performed in order to determine if a GRIN was created, and if the sample was damaged or cracked. Samples with powers above 1.113W cracked, or had no discernable index modification that was able to be seen in the IR camera.

159

Table 6-1 The outcome of each of the different varied experimental parameters is shown. Only samples that showed no cracks had their focal distance estimated with an IR camera.

Power (W)	Beam Waist (mm)	Text (°C)	Initial Evaluation	Sample #	Estimated Focus (mm)
0.89	10	190	Good	6	82
0.89	10	190	Good	1	84
0.89	12	190	Good	3	750
1.113	10	190	Good	4	76
1.113	12	190	Good	2	125
1.113	12	190	Good	5	125
1.335	12	190	Cracked		
1.558	10	190	no GRIN		
2.003	10	190	Broke		
2.003	10	200	Cracked		
2.225	10	200	Broke		
2.448	10	200	Broke		

For sample 6, the focusing ability of the GRIN was further evaluated by shining a collimated 2 µm laser beam through the sample in order to better evaluate the focus and to measure the minimum beam waist. The collimation of the laser without the optic was confirmed by the beam waist not appreciably varying across the spatial region where the beam was to be measured behind the optic. The sample was then put in place and the beam was then imaged at various distances behind the optic. The beam waist was calculated by measuring the number of pixels crossed by the beam and converting this through the pixel size to a length scale. For this process, the waist was measured at locations 25mm apart near the focus and 50mm apart further away with a Spiricon Inc. Pyrocam III detector. The data of the beam waist at various locations was then fit with Equation 13 in order to solve for the minimum beam waist and focal distance.

$$w(z) = w_0\sqrt{1 + \left(\frac{\lambda(z-z_0)}{\pi w_0{}^2}\right)^2} \qquad (13)$$

These beam waists are plotted as a function of distance from the optic in Figure 6-1. The beam waist vs distance was then fitted to determine the location and size of the minimum beam waist, and was determined to be 84 ±3mm and 28 ±3μm respectively. An image of the beam going through the optic for the closest measured location to the focus is shown on the left of this figure, as well as the beam without the optic measured at the same location. The quality of the beam focusing is by no mean perfect, but is able to demonstrate that the technique is feasible to create a usable GRIN optic
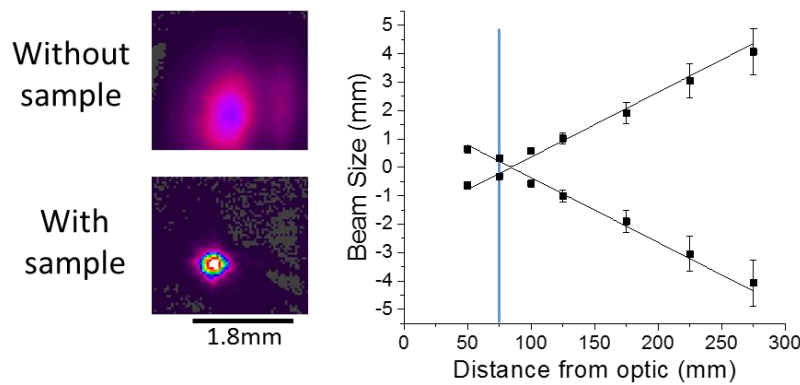
Figure 6-1 The beam waist was measured at different location from the optic (right), which was then able to be used to solve for the minimum beam waist and focal distance. The images on the left are the beam imaged at the blue line on the right graph with and without the optic in place.

Several LIC focusing optics were able to be demonstrated, and the focal lengths and therefore index profiles were able to be modified by changing the refractive index profile through changing the incident power and beam waist of the laser used for the G HT. One of these samples was further characterized by analyzing how a collimated laser beam was affected going through the sample. A minimum beam waist was able to be seen and

measured for this optic. A second type of optical elements that can be created through this method is explored next.

6.2 Diffraction grating via laser-induced crystallization

Similarly to the focusing optic, a LIC grating was made. This was performed in order to show the viability of multiple types of patterning that could be achieved with this method of GRIN. It also is able to highlight profiles that can be made with either LIC or LIV. This section covers the creation of a grating using LIC, where a pulsed 532nm laser was used to locally crystallize the material. Characterization of the post-irradiated sample was performed with a 633nm laser to characterize the created grating through the reflection mode.

For this experiment a grating was created utilizing a 532 nm pulsed laser, and an exposure fluence of $0.085J/cm^2$ (1.55 W/cm^2). This fluence was chosen, as it was just below ablation of the sample with the laser. The beam initially went through a beam splitter, and was directed back upon itself with a mirror to form an interference pattern at the plane where the sample was placed. From the angle of intersection it was determined that the pitch of the formed grating would be around 0.92 μm, which would cause the diffracted angle to be greater than 90° in the transmission spectrum of the glass. The predicted first order reflection diffraction angle is 43° at a wavelength of 633 nm. The sample was characterized post-irradiation with a 633 nm laser and Raman spectroscopy.

Visible inspection of the sample showed three regions where there was likely a grating structure, since viewing these regions from different angles showed different colored reflections when viewed with white light, as would occur with a grating structure that works in the visible as seen in Figure 6-2. A 633 nm laser interrogated the properties

162

of the reflection grating that would be formed, as the sample is highly reflective at this

wavelength. The exit angle of the first order beam with respect to the zeroth order beam

was measured in order to confirm the presence of a grating, and to back-calculate out the

pitch in order to confirm that it was what was predicted based on the pitch calculation

from the angle the beams that were interfered to create the grating.
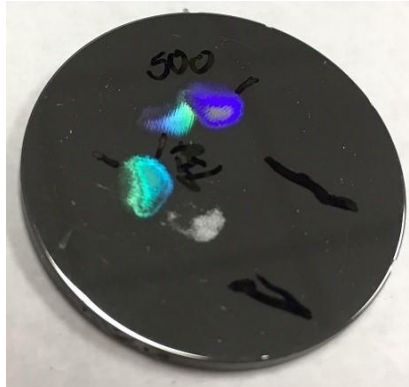
Figure 6-2 Four irradiated locations are seen and show the different colorations that can be observed form the different observation angles present in the image. One of the locations was damaged, and appears silver/white in both images. The disk is 30mm in diameter for scale.

Measurements were taken with an SEM in order to observe the microstructure, as the

feature size was too small to observe with visible microscopy, and therefore WLI as well

and are shown in Figure 6-3 below. Very regular spacing is observed, and appears as if

there may be a slight surface relief. The presence of a change in crystallization state will

need to be confirmed with TEM or μ-XRD.
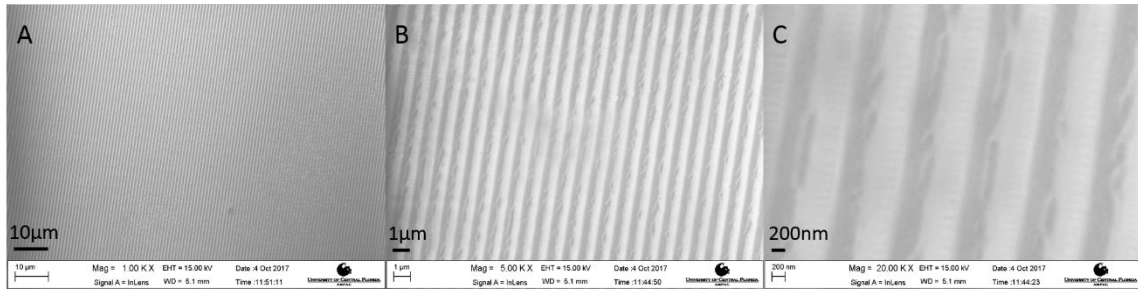
Figure 6-3 SEM images are shown at different magnifications for the irradiated sample.

The laser written structure was interrogated with a 633nm laser in order to see if a reflection grating was able to be formed. Figure 6-4 below depicts the set-up and observed diffraction order that was seen. The laser beam path is indicated by the dashed red line on the left, and hits the sample which is circled in blue, and then travels on to the screen which is seen on the right. The measured angle of the first diffraction order was measured to be 50° for this wavelength, which leads to a pitch of 0.81μm, which is close to what would have been expected.
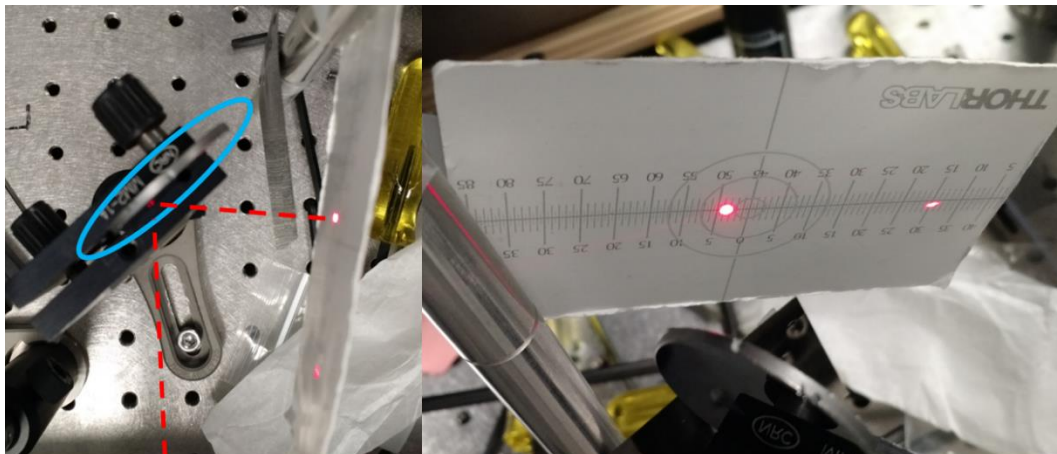
Figure 6-4 The reflection diffraction grating diagnostic set-up used to characterize the post exposed (532 nm, pulsed) sample with a 633nm laser beam (dashed red line). Shown on the left (a) is the sample (circled) being held in place to reflect the grating formed onto the screen and (b) the zeroth and first order diffraction spots.

The pulsed 532 nm laser was able to show a grating structure post-irradiation. The predicted spacing based off of the angle of interference of the laser beams for writing was

164

able to be confirmed through measuring the angle of the first diffraction order in the reflection. As this type of structure is one with a two-tone index, this same type of structure could also be made with LIV.

6.3   Laser-induced vitrification grating

LIV gratings were also made to show the multiple methods possible to pattern this material with different laser conditions by using the 1030nm, fs, MHz laser used in section 5.3. This grating was created using arrays of pillars as described in section 5.3, and then was post-characterized with Raman spectroscopy, observation of diffraction orders for 633nm and ~2μm light, and WLI. In order to achieve this grating structure, the laser conditions used in section 5.3 to LIV a pre-HT sample of 190°C nucleation for 2hrs plus a 30min G HT at 220°C were used. Strips with ~25μm widths, which were made from two rows of columns, were re-vitrified with the laser at a fluence of 3.1E-5 - 1.42E-4 J/cm^2 (31-142 W/cm^2, range is the fluence at the surface when the laser is at the top and bottom of each pillar) with ~25μm of space between the vitrified strips. This should create a grating with a diffraction angle of 0.6° for λ=633nm, and 1.9° for λ=2μm. Similarly to section 5.3, "pillars" were made in the glass ceramic, with 0.01mm spacing between pillars in a row, and with a close packed structure between the two rows. The total grating structure was approximately 1.5 x 1.5mm in size.

In order to evaluate the structures several characterization techniques were used including WLI, Raman, IR diffraction characterization, and visible diffraction characterization. WLI was performed with the system outlined in section 2.12, and is seen in Figure 6-5. The average height change of the material was ~0.16μm, and there is

good homogeneity in the height change across a single strip and between all the strips. The average spacing between the peaks of the strips was also seen to be ~60μm.
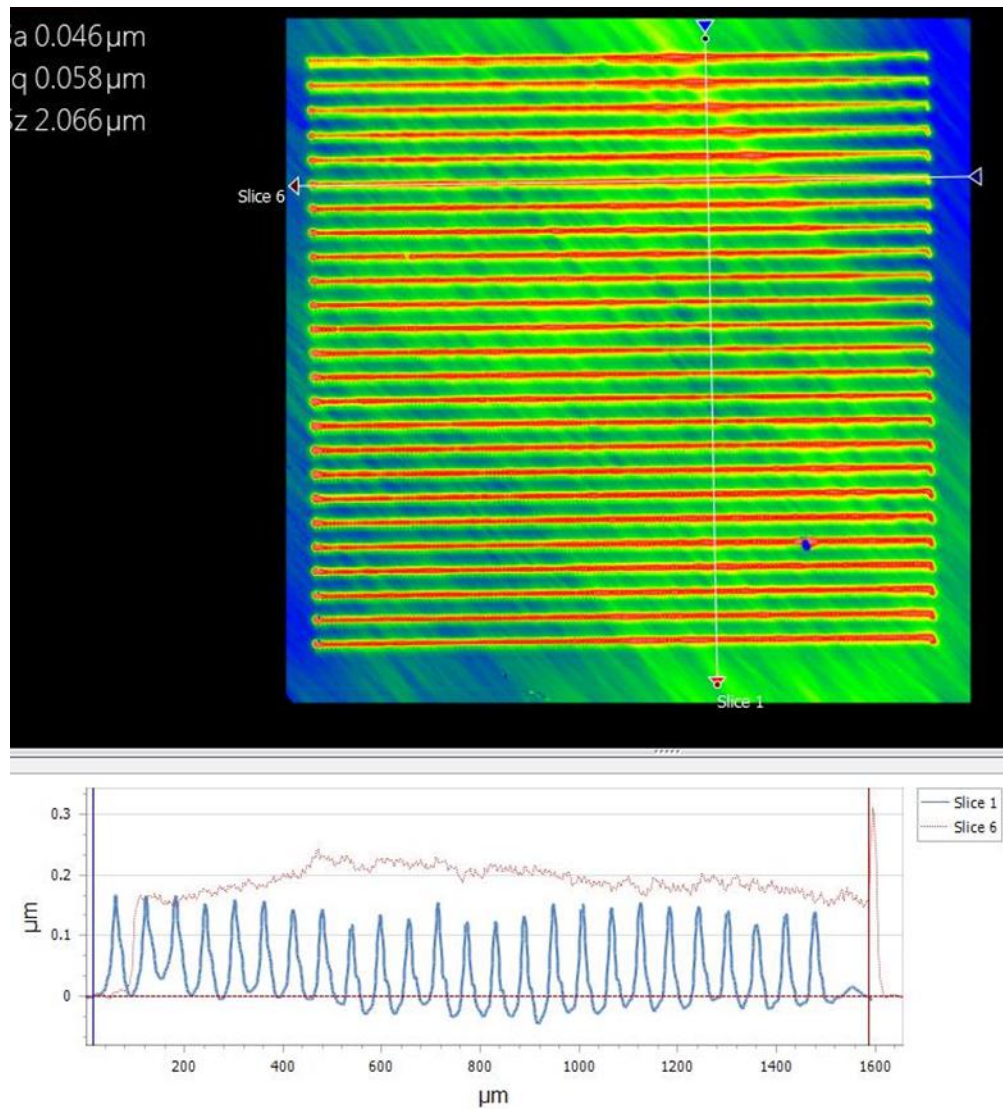
Figure 6-5 WLI of the LIV grating: (top) 2D image of the laser written structure with two slices (slice 1) orthogonal to the writing direction across all grating lines, and (slice 6) along a single grating line following laser processing

Raman was also measured in order to determine the spatial dimensions of the refractive index change in the material. Raman spectra were taken as described in section 2.6, and were taken at a spacing of 2μm in a 2D grid across one of the irradiated strips as seen in Figure 6-6. The Raman spectra were then able to be used to determine the

166

refractive index of the strips, which had a similar profile to the Raman map with values

between 3.0596 and 3.1296 RIU, where the center of the pillars had the lowest index. As

the WLI showed that there was not a change in the photo-expansion from the center of

the pillars outward, the refractive index change is likely solely from the change in the

crystallization of the material.
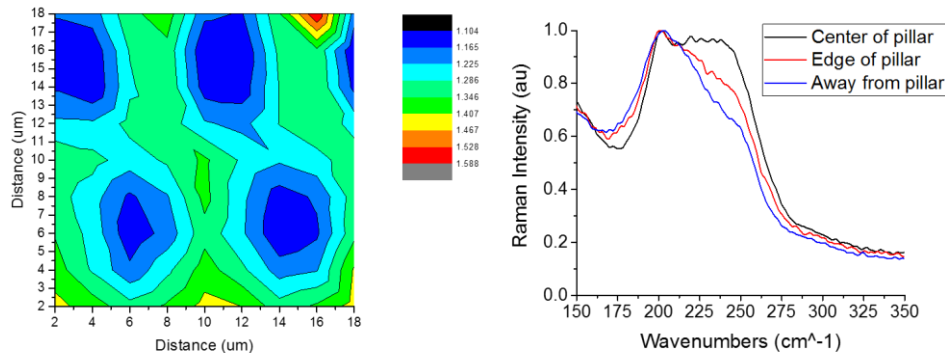
Figure 6-6 A map of the Raman profiles of one of the grating strips is on the left and covers 4 of the pillars that make up the strip. The index profile shows the same type of profile with values ranging from 3.0596 and 3.1296 RIU. The right image is the spectrum at the center of an individual pillar, at the edge of a pillar, and away from the pillar.

The sample was first characterized with a visible, 633nm HeNe laser, so see if a

reflection grating could be observed as there was a height change seen in the WLI

images. The diffraction pattern that was formed is seen in Figure 6-7. The pattern is very

regular, and a faint secondary order is seen to the left of the first order indicating that this

is partially a 2D diffraction grating. This is likely due to the individual columns that were

created, as the spacing between the first and second orders is much wider for the

horizontal direction (spacing between pillars) than the vertical (spacing between strips).

The horizontal order is also much less intense, which is likely due to the very small

amount of height change seen along the strips in the WLI. The diffraction efficiency was

also investigated, but the power of the laser was too low to get a very accurate measurement in the first diffraction order and was seen to be less than 5%.

The Pyrocam described in section 6.1 along with a ~2μm laser was also used to determine if a transmission grating could be observed. As the refractive index change in the irradiated region would be lower, and this same area also saw photo-expansion it was unclear whether the two processes would cancel each other out in the accumulated phase for the laser passing through the grating. As the transmission grating showed much less energy in the diffracted orders as compared to the zeroth order, it seems that the index change and expansion at least partially canceled each other out.
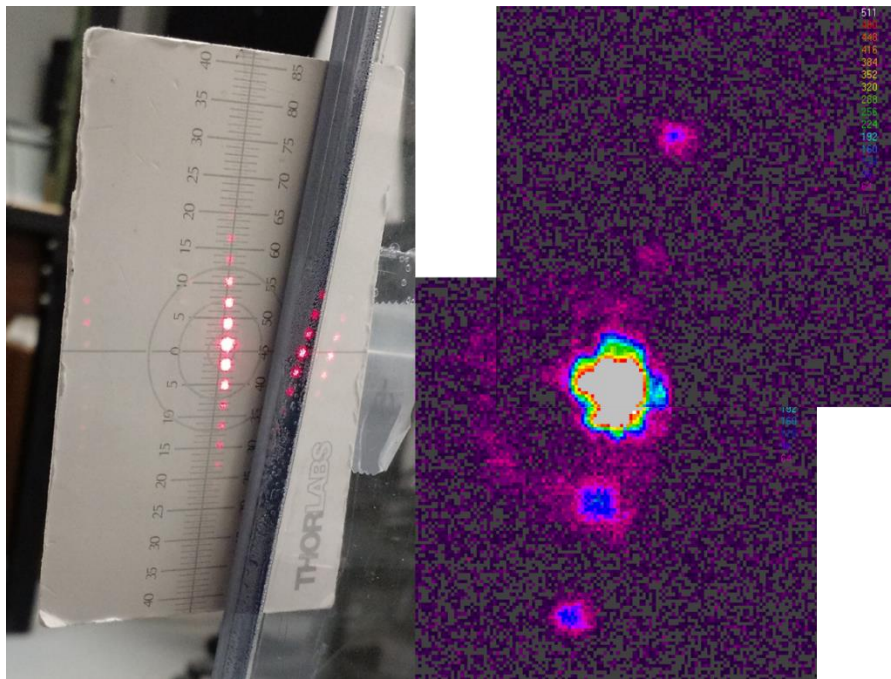
Figure 6-7 The reflection (left) and transmission (right) grating patterns observed for the LIV grating.

6.4   Conclusion

Demonstrators of optical elements through the index patterning of 40mol% PbSe glass ceramics were created. While not optimized for transmission or specific optical

designs, the effort confirmed that laser-assisted protocols based on crystallization or vitrification could modify materials to realize index changes yielding modification in optical function from that of a base glass material. Prototype optics were created using the techniques of LIC and LIV in order to show the various methods that are able to spatially change the refractive index in this material. These two techniques complement each other and allow for more variability of index structures that can be created. They also allow for multiple write cycles if used in conjunction with each other. Focusing optics were able to be created with LIC on pre-nucleated samples. The focal length was able to be varied from 82-750mm by varying the irradiation parameters, and therefore refractive index distribution. Two different methods were able to be used to characterize one of the samples, though imaging a grid through the sample and by characterizing the samples effect on a collimated laser. The two techniques measured focal distances of 82 and 84mm respectively which are within the error of each other.

Diffraction gratings were able to be created through LIC and LIV. These two grating had different pitches though, so a direct correlation between the two techniques was not able to be accomplished. The LIC grating was able to be characterized through visualization of a grating structure with a 633nm beam, as the pitch was too small for characterization with an IR laser that is in the samples transparency range. The predicted pitch as measured by the angle of interference of the beams was 0.92μm, and the pitch calculated from the angle of the first diffraction order was found to be 0.81μm. As these two are fairly close, the diffracted beam is likely from a grating structure in the material.

The LIV grating was able to be characterized with WLI, Raman spectroscopy, and diffraction characterization with a 633nm and an ~2μm laser. The WLI showed that there

was in fact photo-expansion of the material in the irradiated regions, and that this expansion was homogeneous across the region that was irradiated. The Raman spectra was able to be used to map the Raman ratio and therefore refractive index of part of one of these strips. It was seen that the largest modification of the refractive index was seen at the center of one of the pillar structures, despite the fact that there isn't a height difference in between the pillar structures seen with the WLI. This indicated that the refractive index change is likely not tied to the photo-expansion occurring. A grating structure was able to be seen with both the reflective (633nm) and transmissive (2μm) modes of the optic. The transmission grating did not have as many diffraction orders as was seen with the reflection, which could be due to the competing effects of a decrease in the refractive index and photo-expansion occurring in the same region.

Both of these techniques used to create diffraction gratings by modifying the refractive index within the material were able to show grating behavior and therefore show that they are complementary techniques to structure the refractive index within a sample. An overview of all the components that were made are in Table 6-2 below.

Table 6-2 An overview of the demonstrator optical elements including how they were created and their resulting optical function.

Measurement	LIC Focusing Optic	LIC Grating	LIV Grating
Irradiation conditions	λ=532nm, CW, irradiance=0.567 W/cm^2	λ=532nm, pulsed, fluence=0.085J/cm^2	λ=1030nm, pulsed, fluence=1.42E-4J/cm^2
Pre-irradiation heat treatment	190°C-2hrs	190°C-2hrs	190°C-2hrs + 220°C-20min
Resulting optical function	focusing	Grating – 1st order in reflection mode	Grating – several orders in reflection and transmission
Evidence of index change	Changes in the Raman spectra		Changes in the Raman spectra

7   CONCLUSIONS

This study aimed to develop infrared transparent glass ceramics suitable for use as GRIN materials. The effort combined optical material science and evaluation of laser-material interactions to realize optical nanocomposites (glass ceramics) which possessed spatially varying microstructures that resulted in changes in optical properties and measurable optical function. Findings that resulted from the effort confirmed that while this goal was possible, as demonstrated by the first prototypes of optical components created from our materials, both the properties of the parent glass starting material and the methodology used to convert the glass to glass ceramic (i.e., to induce controlled crystallization) were critical to the properties of the final nanocomposite.

Glasses with compositions of $(GeSe_2\text{-}3As_2Se_3)_{1-x}PbSe_x$ with x=0 to 40 in increments of 5 mol% were evaluated for their ability to form glass ceramics upon HT. The base material properties were characterized, and their dependence on the starting glass morphology was determined. Primary to this study were changes in refractive index and transmission with formation of the secondary phase(s), as well as concurrent modifications to other physical properties, such as changes in structure, density, μ-hardness, glass transition temperature, and thermal conductivity. For the base glass the refractive index was seen to be independent of the starting morphology (the glass being either homogeneous or phase separated), while the short wave cut-off (SWCO, defined as 90% of the maximum transmission) was seen to be highly dependent on the starting morphology.

The formation of various crystallized phases (phase type and quantity) as identified via XRD were defined by the parent glass morphology and showed that the transition

between Pb-rich droplets and a Pb-rich matrix corresponds with the transition in the types of crystal phases that were formed. The volume fraction of these phases (created using a fixed nucleation and growth heat treatment protocol) were then used to quantify the predicted refractive index using effective medium theory. This predicted index was compared with the measured index, and confirmed that the post-heat treatment refractive index change was due to induced ceramization from the HT. The change in the transmission associated with the secondary phase formation by this fixed HT protocol was found to degrade due to induced scatter from the ceramization process' precipitated phase(s), thus limiting some compositions from their potential use in components with applications in the MWIR. This was not the case for all materials, nor likely the case for other HT protocols not investigated in this study.

These optical property measurements systematically tracked with the type and volume fraction of crystal phases seen as a function of PbSe content, where there was little change observed in compositions that did not crystallize (5 mol% PbSe), and a repeatable discontinuity in trends at the composition where not only morphology changed but the resulting crystallized phases changed (30 mol% PbSe). From this it was confirmed that while some of the base glass material properties were dependent on the glass morphology and Pb content, the post-HT glass ceramic's properties were largely dependent on the type/amount of the crystal phases formed, and the resulting microstructure.

Of the multiple glass compositions examined, the 40 mol% PbSe material exhibits the greatest potential for use in MWIR optics as it maintained its optical transmission in the MWIR, with a concurrently large, post-HT change in the refractive index on the order of

0.1 RIU. Multiple nucleation and growth HT conditions were investigated to determine the effect of the HT conditions on the post-cerammed material. The post-HT samples were characterized with XRD, refractive index, and Raman spectroscopy. Measurements showed a direct correlation between the composite's crystal phase formation (total volume fraction) as measured via XRD to the refractive index. These facts were subsequently correlated directly to structural changes accompanying the secondary phase formation, specifically showing that refractive index change could be directly correlated with observed changes in the material's Raman spectrum (quantified by a novel method of analysis, defined as the Raman ratio). As this technique allows measurement over small spatial areas (10's of microns) where we would like to evaluate spatial variation in refractive index (for GRIN applications), the technique was shown to directly lend itself to 3D refractive index mapping. This mapping protocol was used to demonstrate quantification of induced GRIN profiles in the 40 mol% PbSe material.

The goal of being able to pattern GRIN structures in the material by spatially modifying the nucleation or growth in the material was investigated on the 40mol% PbSe composition using laser-assisted modification. Multiple irradiation techniques were investigated including laser-induced crystallization of pre-nucleated or base glass samples, laser-induced nucleation with a subsequent (furnace) growth HT, laser removal of nucleation with a subsequent growth HT, and laser removal of (all) crystallization of a pre-nucleated plus grown sample. These samples were characterized with Raman spectroscopy, and the post-processed microstructural modification was documented via electron microscopy.

Laser-induced crystallization of a pre-nucleated sample and a base glass sample were accomplished with a 532 nm, CW laser and a 1064 nm, ns laser, respectively. The Gaussian beam of a 532 nm source was used to create a thermal profile inside the material that translated to a crystallization and therefore index gradient, whereas the 1064 nm exposure resulted in a combination of thermal and photonic effects to create a spatial variation in the growth throughout the sample. Raman spectroscopy was used to evaluate the samples, and spectra were taken across the samples in order to map the induced changes in the material. The 532 nm laser exposure was also simulated, and the refractive index changes predicted from the heating seen in the simulations were compared to those measured from Raman and were seen to have good correlation, though improvements to the models are still needed to be able to have better agreement. The 1064 nm exposure had some Raman features that had not been observed with furnace HT, so the Raman map could not be converted to a refractive index map. Further characterization of these microstructural changes would need to be accomplished through μ-XRD or TEM to confirm relative phase fractions. Both of these irradiation protocols demonstrated changes in the crystallization state of the material, but were limited in their spatial profiles that they could create as they required long exposure times and used wavelengths that were in a high absorption region of the material.

In order to investigate laser-induced modification with a source that was within the transparency region of the material a 110 fs, 1.3μm source was used to induce nucleation in a 40 mol% sample. Following a post-exposure furnace growth HT, the samples were investigated with Raman spectroscopy to determine if there were any changes in the microstructure between irradiated and non-irradiated regions. Irregular results with

questionable reproducibility along with unwanted surface modifications made this laser induced crystallization strategy undesirable. However, the high repetition rate of other systems presented a new strategy that involved an inverse method of patterning the refractive index through laser exposure of a pre-heat treated glass ceramic.

LIV, whereby either a nucleated sample or glass ceramic sample could be selectively restored to its original glassy state was shown to result in patterned index structures. Through localized melting of pre-existing crystallites, the exposure could effectively erase regions where nucleation or growth were already present in the starting material. This first used on 40mol% PbSe sample that was pre-nucleated showed lower growth post HT+laser+HT (as defined by Raman spectroscopy). This indicates that the pre-existing nucleation was able to be removed with a 1.3μm, fs, kHz laser, through preferential growth in areas that were not irradiated, and therefore had more nuclei. As this sample was post-HT, there is high confidence in the reliability of the Raman ratio previously defined for furnace HT being applicable to this situation. Laser erasure of crystal growth was investigated with a 1.03μm, fs source. Post-irradiation the sample was investigated with Raman spectroscopy, and the signal was found to return back to that of the base glass. TEM was also used and showed a decrease in the amount of crystallization in the material post-irradiation. In order to confirm that the sample saw a decrease in all the crystal types, further characterization with μ-XRD is needed.

With the knowledge of the different laser-assisted crystallization mechanisms that are possible in the 40mol% PbSe sample, demonstrator optics were able to be fabricated in order to evaluate GRIN structures written into the material. A focusing optic was able to be created through laser induced crystallization of a pre-nucleated sample. This sample

175

had the focus and minimum beam waist measured with a collimated laser transmitted through the sample. Two diffraction gratings were also created, one with laser induced crystallization, and one with laser erasure of growth. The laser induced crystallization grating has too narrow of a pitch to be able to characterize in the IR, or with Raman spectroscopy, but did exhibit diffraction behavior in the visible for a reflection mode. Additional characterization with TEM is needed to be able to determine if there were changes in the crystal structure that cause the diffraction. The laser erasure of growth sample showed grating behavior in the visible and IR, photo-expansion through WLI, and Raman change back towards the base glass state in the middle of the written structures. A deconvolution of the effects of the photo-expansion and index change has not yet been characterized, but could be carried out with additional microstructural characterization through TEM.

Through this work new materials were able to be developed, and their ability to form a glass ceramic was characterized. Their potential refractive index change upon ceramization was also studied, and a technique for being able to spatially measure the refractive index was developed. Spatial variation of the refractive index of the material upon laser irradiation was also explored and determined. Useful optical elements were then created as proof-of-concept demonstrators in order to show how the various methods of creating GRIN in these materials can be utilized. There are still some aspects of this work that need to be further explored in order to move towards integration of GRIN optical elements made from these materials/techniques into infrared optical systems.

8 FUTURE WORK

While this work has shown conclusively that a multi-component infrared transparent glass can be selectively crystallized with spatial control to yield a tailorable level of refractive index change suitable for use as a candidate GRIN material, there remain several key issues that require further clarification before the material and processing methodologies could be extended towards a prototype optic for a system. These additional items can be separated into aspects of the starting material as well as the processes used to impart controlled, spatially selective conversion from a starting glass to a glass ceramic (or vice versa in the case of laser-induced vitrification, LIV). Sections below are separated to highlight these specific aspects of the process.

Future developments can be continued in the various research thrusts exhibited in this document. Further work can be made in the ceramization process in order to better maintain the SWCO, while still having a useful Δn. Further development of the thermal modeling is also needed. More work can also be performed with LIC and LIV of the material in order to have better spatial control of the index profile, and to have more modification into the bulk of the material. Further development of index patterns that can be created with LIC or LIV that would be useful as functional optical elements also needs to occur. Lastly the scalability of the various techniques needs to be evaluated in order to determine if fabrication of useful optical elements can be performed on large enough scales and at a high enough speeds for production.

8.1   Glass ceramic

Further development can be produced in the compositions that were studied in order to have controlled growth that does not affect the band edge as much as the HT conditions used in this study. Additionally, tuning the composition further may change which crystals are forming, and cause ones that have less scatter to form. In [40], the glass forming region of this glass is able to be pushed up to 50mol% PbSe. With the added Pb-content these glasses may have a greater potential refractive index change, or precipitate out different crystals than those seen in the 35 or 40mol% PbSe that would affect the SWCO less.

Additional work could also include adding halides into the material in order to push the SWCO further into the visible range in order to create optics with short-wave infrared (SWIR) to LWIR capabilities as used in [2,9,33]. These new materials would need to be fabricated and tested for their ability to form a glass ceramic to see if they would be able to ceramize controllably and maintain their optical transparency in the SWIR.

8.2   Thermal modeling

Further development of the thermal models is needed, specifically with respect to the boundary conditions. The modeling that was used was a good first approximation, but need to be further refined. The main thermal property that was not able to be measured for this sample was the coefficient of heat transfer for the convective boundary condition. If this property was able to be measured there would be an increase in the accuracy of the models.

8.3   Laser assisted crystallization

Further laser modification efforts could be performed with a laser that is both in the transparency range of the material, and has a reproducible, good quality beam profile. Additionally by using a slightly different composition such as 45 or 50mol% PbSe, the transparency of the base glass might be low enough to use an ~1μm laser. Also if the addition of halides into the matrix are able to produce material that can be used to form glass ceramic, than these materials might also be able to be used with shorter wavelength lasers as the bandedge is typically reduced in these materials.

Further study with LIV will need a fs, MHz laser that is within the transparency range of these glasses once they are HT. This could be accomplished by switching compositions to one that is much more transparent to 1.03μm light or switch to a laser source further into the IR. This would allow for writing structures inside of the bulk of the material. Further characterization of induced structures also need to be confirmed with μ-XRD or TEM to ensure that the Raman spectra that are obtained are indeed from the crystallization state changing. Additionally this technique could be evaluated for use in conjunction with a gradient HT profile. This could allow for more intricate GRIN structures to be created.

8.4   Additional optical elements

With advances in both LIC and LIV, more GRIN profiles could be realized in order to create different or better functioning optical elements. Further precision of writing could create more efficient and tunable Bragg gratings using the techniques that were explored in this work. Additionally with LIV exploration into Fresnel lenses and polarization plates would be possible. Lastly, the optimal goal for future work would be to have the

ability to make a GRIN lens that would be of high enough quality to be used in a system and would decrease the number of optical elements needed.

8.5   Scale-up feasibility

In order for this research to have an increased impact on society, the ability of the processes and materials to be able to be scaled up needs to be assessed. The size of potentially useful optical elements needs to be analyzed to see if further scale up of the melt size needs to occur, which could mean the composition may need to be altered or the melting methodology modified. The latter, carried out in partnership with a manufacturing partner, has been shown to enhance transmission in similar compositions to those created here.

Apart from being able to create a large enough optical element, one also has to be able to manufacture it on a timescale that is reasonable for production. Several techniques can be used to minimize the time needed. One way is with the addition of holographic writing techniques, where larger regions could be exposed at any given time in order to speed up the laser writing process. The use of masks could also be used in a similar manner.

8.6   Conclusions

There are still many avenues of research to be performed to continue the scope of this work. Further optimization of the material and laser writing techniques are most important in order to be able to have more control of the laser writing process. Additional refinement of thermal models can also help to better refine the irradiation conditions that are needed. Along with optimizing the writing process, new GRIN structures can be

realized and created. The process can then be optimized in order to make sure that the

processing is scalable and is able to be created on a reasonable timescale.

APPENDIX A: DN/DT

Below are index dn/dT data that were measured by Megan Melvin for a directed research project for OSE 4912 at the University of Central Florida on commercially available glass that were manufactured by Schott. Data includes reference data from Schott's website, data from a former student in our research group [114], and by Megan Melvin.

Refractive Index at 4.515 μm, 22°C		
Sample	Measured Index	Standard Index [6-9]
IG2	2.6204±0.0001	2.5117
IG4	2.6208±0.0001	2.6204
IG5	2.6206±0.0001	2.6202
IG6	2.7916±0.0002	2.7927

dn/dT of IG5 at 4.515 μm

$y = 6E{-}05x + 2.6209$

$y = 7E{-}05x + 2.6197$
$R^2 = 0.98884$

$y = 6E{-}05x + 2.6187$

dn/dT of IG6 at 4.515 μm

$y = 5E{-}05x + 2.7911$
$R^2 = 0.92115$

$y = 4E{-}05x + 2.7918$

$y = 3E{-}05x + 2.7918$

184
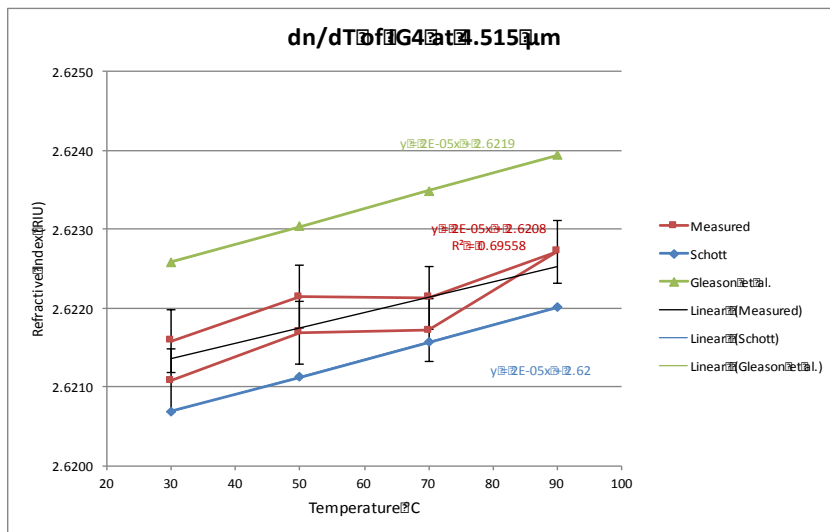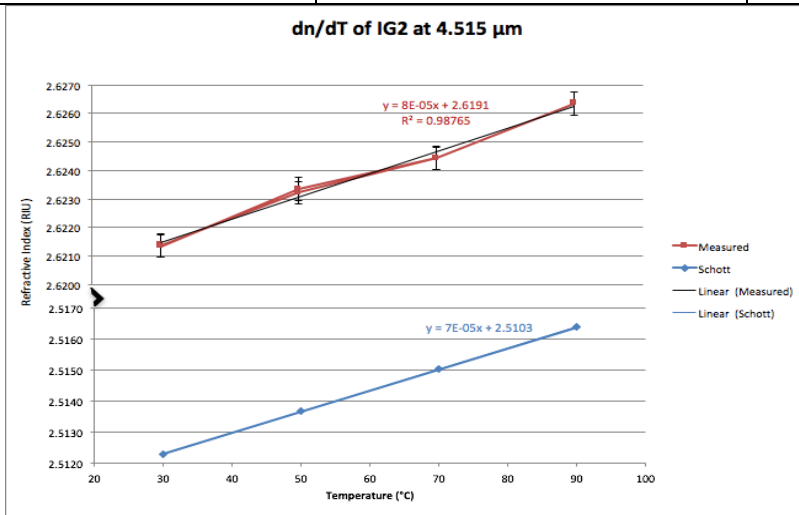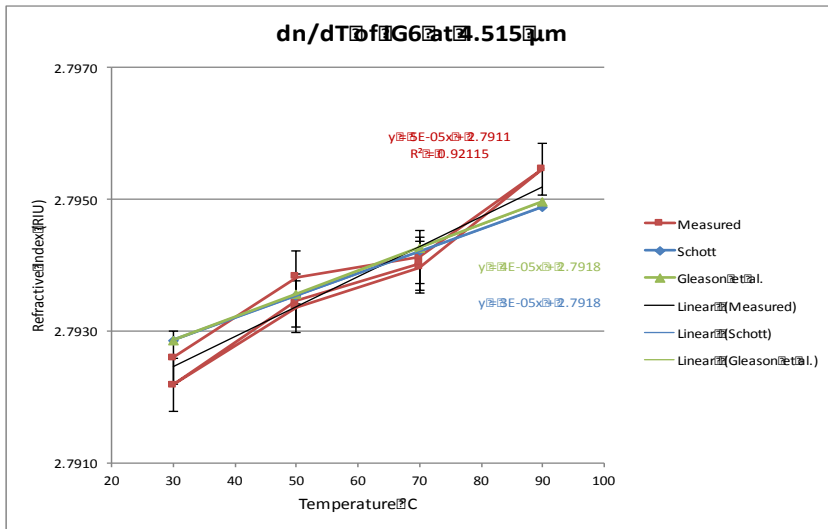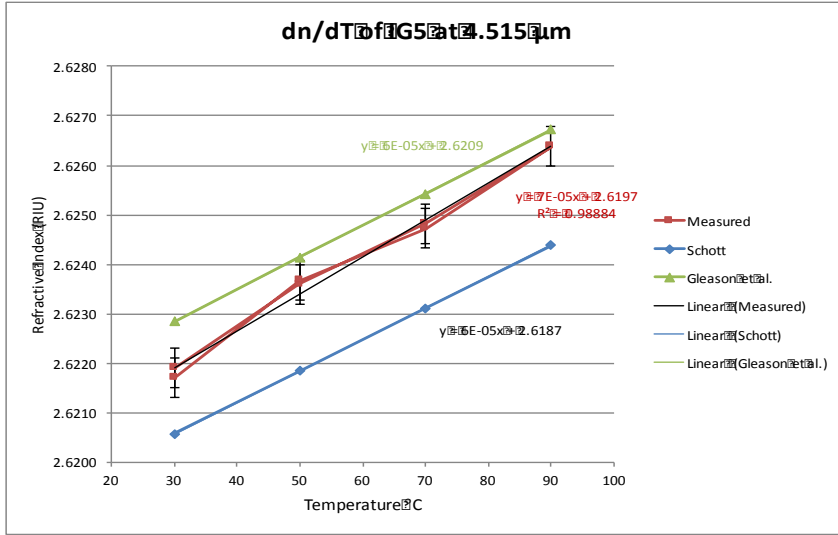
APPENDIX B: PROPERTY DATA FOR 15GESE2-45AS2SE3-40PBSE

15GeSe$_2$-45As$_2$Se$_3$-40PbSe

Product Information

These data are for glass prepared from a 400g melt made using high purity elemental starting materials, vacuum sealed in a quartz ampoule from UCF. Final dimensions are 1" x thickness 2 mm post processing.

Measurements Information

Density was determined by Archimedes method at room temperature. Heat capacity and thermal conductivity was determined by transient plane source method. Transition temperature measured by DSC [error = +/-2°C]. Index at single wavelengths measured by prism refractometry [typical error = 5×10^{-4} in SWIR/MWIR and 1.5×10^{-3} in LWIR]. Transmission window were measured with a UV-VIS and FTIR.

Material Properties (Base Glass)	
As-Batched Composition (at%)	Ge$_{4.3}$As$_{25.7}$Pb$_{11.4}$Se$_{58.6}$
Density (g/cm^3) @ 22°C	5.48 ± 0.001
Thermal Expansion (10^{-6} C^{-1}) [25-180 C]	19 ± 0.1
Specific Heat (J/(g·K)) (25°C)	0.229 ± 0.006
Thermal Conductivity (W/(m·K)) (25°C)	0.239 ± 0.003
Transition Temperature (°C)	201
Crystallization Temperature [peak] (°C)	259
Transmission Window (µm)	1.4-11.8
dn/dT (K^{-1})	90 ± 10
Refractive index at λ =4.515 µm, 30°C	3.0460 ± 0.0004

DSC – Base glass
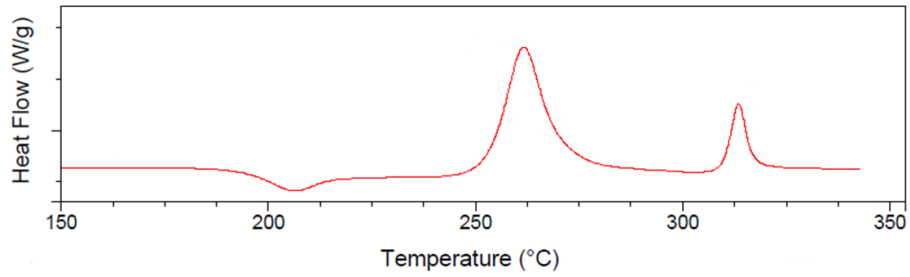
Transmission – Base glass
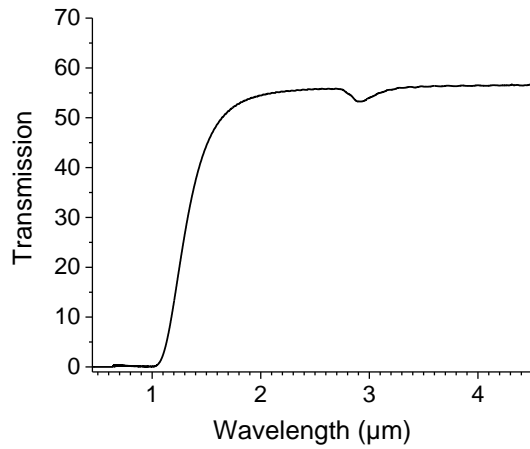
Refractive index – HT glass
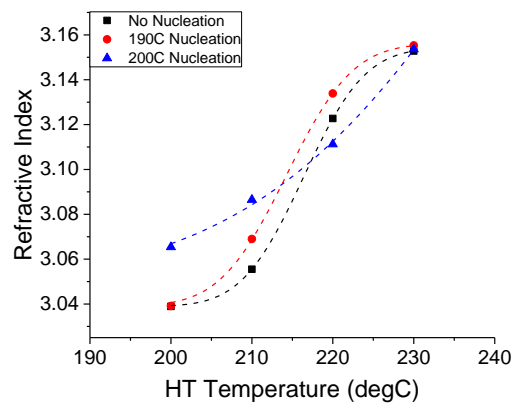
XRD – HT glass
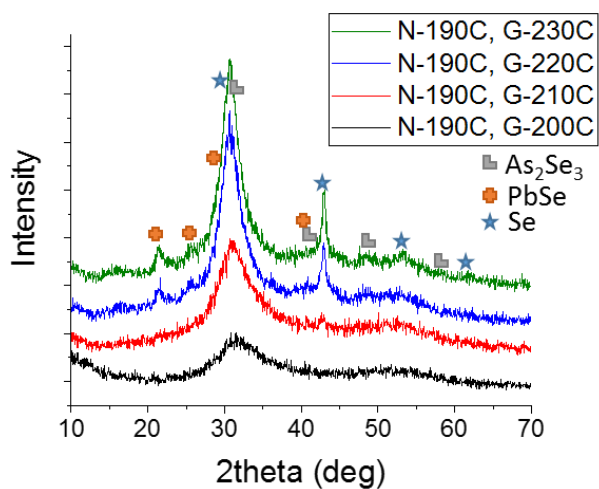
Tabular form – optical and crystal phase information from N, G conditions shown

N	G	Index	Transmission	XRD				
		Index	SWCO	As$_2$Se$_3$	PbSe	Se	Total	Ratio
No-N	G-200°C	3.0389	1.3396	0	0.1	0.1	0.2	0:50:50
	G-210°C	3.0555	1.385	3.4	2.3	0.6	6.3	54:37:10
	G-220°C	3.1227	1.534	8.5	6.3	1.8	16.6	51:38:11
	G-230°C	3.1528	1.5939	11.1	8.8	2.6	22.5	49:39:12
N-190°C	G-200°C	3.0391	1.3635	0.6	0.5	0.6	1.7	35:29:35
	G-210°C	3.069	1.4241	7	4.9	1.5	13.4	52:37:11
	G-220°C	3.1339	1.471	10.7	7.7	2.3	20.7	52:37:11
	G-230°C	3.1553	1.5409	14.2	10.5	3	27.7	51:38:11
N-200°C	G-200°C	3.0654	1.398	0.3	0.1	0.1	0.5	60:20:20
	G-210°C	3.0865	1.4034	3.1	2.5	0.7	6.3	49:40:11
	G-220°C	3.1112	1.4748	9.3	7.2	.2	16.7	56:43:1
	G-230°C	3.1536	1.5132	13.1	9.5	2.6	25.2	52:38:10

REFERENCES

1. C. Lin, L. Calvez, M. Roze, H. Tao, X. Zhang, and X. Zhao, "Crystallization behavior of $80GeS_2$-$20Ga_2S_3$ chalcogenide glass," Applied Physics A **97,** 713-720 (2009).

2. L. Calvez, H. Ma, J. Lucas, and X. Zhang, "Selenium-based glasses and glass ceramics transmitting light from the visible to the far-IR," Adv Mater **19,** 129-132 (2007).

3. "Thermal Cameras for Firefighting Applications, "http://www.flir.com/fire/content/?id=69019.

4. "Thermal Imaging Cameras for Machine Vision / Industrial Safety, "http://www.flir.com/automation/content/?id=65833.

5. J. Yan, T. Zhou, J. Masuda, and T. Kuriyagawa, "Modeling high-temperature glass molding process by coupling heat transfer and viscous deformation analysis," Precision Engineering **33,** 150-159 (2009).

6. M. Poulain, "Halide glasses," Journal of Non-Crystalline Solids **56,** 1-14 (1983).

7. Z. Donghui, X. Fang, C. Guorong, Z. Xianghua, M. Hongli, and J. L. Adam, "Formation and Properties of Chalcogenide Glasses in the $GeSe_2$-As_2Se_3-CdSe System," J Am Ceram Soc **88,** 3143-3146 (2005).

8. J. J. Mecholsky Jun, C. T. Moynihan, P. B. Macedo, and G. R. Srinivasan, "Microstructure and properties of an infra-red transmitting chalcogenide glass-ceramic," J. Mater. Sci. **11,** 1952-1960 (1976).

9. Y. Ledemi, B. Bureau, L. Calvez, M. L. Floch, M. R., C. Lin, X. H. Zhang, M. Allix, G. Matzen, and Y. Messaddeq, "Structural Investigations of Glass Ceramics in the Ga_2S_3-GeS_2-CsCl System," J Phys Chem B **113,** 14574-14580 (2009).

10. M. Roze, L. Calvez, J. Rollin, P. Gallais, J. Lonnoy, S. Ollivier, M. Guilloux-Viry, and X. Zhang, "Optical properties of free arsenic and broadband infrared chalcogenide glass," Applied Physics A **98,** 97-101 (2010).

11. V. S. Vassilev, Z. G. Ivanova, L. Aljihmani, E. Cernoskova, and Z. Cernosek, "Glass-forming regions, properties, and structure of the chalcogenide As_2Se_3-$GeSe_2$-SnTe (Ag_4SSe) systems," Mater Lett **59,** 85-87 (2005).

12. A. B. Seddon, "Chalcogenide glasses: a review of their preparation, properties and applications," J. Non Cryst. Solids **184,** 44-50 (1995).

13. C. Meneghini and A. Villeneuve, "As$_2$S$_3$ photosensitivity by two-photon absorption: holographic gratings and self-written channel waveguides," J Opt Soc Am B **15,** 2946-2950 (1998).

14. V. M. Lyubin and V. K. Tikhomirov, "Novel photo-induced effects in chalcogenide glasses," J. Non Cryst. Solids **135,** 37-48 (1991).

15. L. Petit, N. Carlie, T. Anderson, M. Couzi, J. Choi, M. Richardson, and K. C. Richardson, "Effect of IR femtosecond laser irradiation on the structure of new sulfo-selenide glasses," Optical Materials **29,** 1075-1083 (2007).

16. J. D. Musgraves, S. Danto, and K. Richardson, "4 - Thermal properties of chalcogenide glasses," in *Chalcogenide Glasses*, J. Adam and X. Zhang, eds. (Woodhead Publishing, 2014), pp. 82-112.

17. C. Liu, G. Tang, L. Luo, and W. Chen, "Phase separation inducing controlled crystallization of GeSe$_2$–Ga$_2$Se$_3$–CsI glasses for fabricating infrared transmitting glass–ceramics," J Am Ceram Soc **92,** 245-248 (2009).

18. L. Calvez, H. L. Ma, J. Lucas, and X. H. Zhang, "Glasses and glass-ceramics based on GeSe$_2$–Sb$_2$Se$_3$ and halides for far infrared transmission," J. Non Cryst. Solids **354,** 1123-1127 (2008).

19. X. Zhang, M. A. Hongli, and J. Lucas, "A new class of infrared transmitting glass-ceramics based on controlled nucleation and growth of alkali halide in a sulphide based glass matrix," J. Non Cryst. Solids **337,** 130-135 (2004).

20. A. Marotta, A. Buri, and F. Branda, "Nucleation in glass and differential thermal analysis," J. Mater. Sci. **16,** 341-344 (1981).

21. J. Massera, J. Remond, J. Musgraves, M. J. Davis, S. Misture, L. Petit, and K. Richardson, "Nucleation and growth behavior of glasses in the TeO$_2$-Bi$_2$O$_3$-ZnO glass system," J. Non Cryst. Solids **356,** 2947-2955 (2010).

22. W. Holand and G. H. Beall, *Glass Ceramic Technology* (John Wiley & Sons, 2012).

23. L. Sisken, "Distribution of laser induced heating in multi-component chalcogenide glass and its associated effects," MS Thesis, Optics, University of Central Florida (2014).

24. C. Bhugra and M. J. Pikal, "Role of thermodynamic, molecular, and kinetic factors in crystallization from the amorphous state," J. Pharm. Sci. **97,** 1329-1349 (2008).

25. A. A. Cabral, V. M. Fokin, E. D. Zanotto, and C. R. Chinaglia, "Nanocrystallization of fresnoite glass. I. Nucleation and growth kinetics," Journal of Non-Crystalline Solids **330,** 174-186 (2003).

26. K. Matusita and M. Tashiro, "Rate of homogeneous nucleation in alkali disilicate glasses," Journal of Non-Crystalline Solids **11,** 471-484 (1973).

27. L. L. Burgner and M. C. Weinberg, "An assessment of crystal growth behavior in lithium disilicate glass," Journal of Non-Crystalline Solids **279,** 28-43 (2001).

28. C. S. Ray and D. E. Day, "An analysis of nucleation-rate type of curves in glass as determined by differential thermal analysis," J. Am. Ceram. Soc. **80,** 3100-3108 (1997).

29. A. G. Dias, J. M. S. Skakle, I. R. Gibson, M. A. Lopes, and J. D. Santos, "In situ thermal and structural characterization of bioactive calcium phosphate glass ceramics containing TiO_2 and MgO oxides: high temperature – XRD studies," Journal of Non-Crystalline Solids **351,** 810-817 (2005).

30. A. G. Dias, M. A. Lopes, I. R. Gibson, and J. D. Santos, "In vitro degradation studies of calcium phosphate glass ceramics prepared by controlled crystallization," Journal of Non-Crystalline Solids **330,** 81-89 (2003).

31. G. Yang, X. Zhang, J. Ren, Y. Yunxia, and G. Chen, "Glass formation and properties of chalcogenides in a $GeSe_2$–As_2Se_3–PbSe system," J Am Ceram Soc **90,** 1500-1503 (2007).

32. Z. Yang, L. Luo, and W. Chen, "Red color $GeSe_2$-based chalcohalide glasses for infrared optics," J Am Ceram Soc **89,** 2327-2329 (2006).

33. L. Calvez, P. Lucas, M. Roze, H. L. Ma, J. Lucas, and X. H. Zhang, "Influence of gallium and alkali halide addition on the optical and thermo-mechanical properties of $GeSe_2$-Ga_2Se_3 glass," Applied Physics A **89,** 183-188 (2007).

34. G. Tang, C. Liu, Z. Yang, L. Luo, and W. Chen, "Micro-structural studies of $GeSe_2$-Ga_2Se_3-MX (MX = CsI and PbI_2) glasses using Raman spectra," J. Non Cryst. Solids **355,** 1585-1589 (2009).

35. G. Tang, Z. Yang, L. Luo, and W. Chen, "Preparation and properties of $GeSe_2$-Ga_2Se_3-KBr new chalcohalide glasses," J. Alloys Compounds **459,** 472-476 (2008).

36. L. Calvez, H. Ma, J. Lucas, and X. Zhang, "Preparation and properties of glasses and glass-ceramics based on $GeSe_2$–Sb_2Se_3 and halides," Physics and Chemistry of Glasses - European Journal of Glass Science and Technology Part B **47,** 142-145 (2006-04-01T00:00:00).

37. M. Hubert, G. Delaizir, J. Monnier, C. Godart, H. Ma, X. Zhang, and L. Calvez, "An innovative approach to develop highly performant chalcogenide glasses and glass-ceramics transparent in the infrared range," Opt.Express **19,** 23513-23522 (2011).

38. H. Wang, X. Zhang, G. Yang, Y. Xu, H. Ma, J. L. Adam, Z. Gu, and G. Chen, "Micro-crystallization of the infrared transmitting chalcogenide glass in $GeSe_2$–As_2Se_3–$PbSe$ system," Ceram. Int. **35,** 83-86 (2009).

39. A. K. Buff, "A Study of Crystallization Behavior in Phase Separated Chalcogenide Glasses," MS Thesis, Department of Materials Science and Engineering, University of Central Florida (2016).

40. A. Yadav, M. Kang, C. Smith, J. Lonergan, A. Buff, L. Sisken, K. Chama, C. Blanco, J. Caraccio, T. Mayer, C. Rivero-Baleine, and K. Richardson, "Influence of phase-separation on structure-property relationships in the $(GeSe_2\text{-}3As_2Se_3)_{1\text{-}x}PbSe_x$ glass system," Physics and Chemistry of Glasses: European Journal of Glass Science and Technology Part B. (2017).

41. L. Sisken, M. Kang, C. Smith, A. Buff, D. McClane, C. Blanco, T. S. Mayer, A. Swisher, C. Rivero-Baleine, and K. Richardson, "$GeSe_2$-As_2Se_3-$PbSe$ glass ceramics – novel materials for IR GRIN components," to be submitted, Adv. Opt. Mats (2017).

42. I. D. Aggarwal, C. T. Moynihan, P. B. Macedo, J. J. Mecholsky, and G. R. Srinivasan, "Glass Formation in the Pseudobinary Metallic Selenide Systems $M_{(m)}Se_{(n)}$-$Ge_{(1.5)}As_{(0.5)}Se_{(3)}$," J Am Ceram Soc **55,** 366-368 (1972).

43. C. T. Moynihan, P. B. Macedo, I. D. Aggarwal, and U. E. Schnaus, "Direct observation of the double glass transition in a phase-separated glass," J. Non Cryst. Solids **6,** 322-328 (1971).

44. A. Yadav, A. Buff, C. Smith, K. Chamma, J. Marro, M. Melvin, L. Sisken, C. Rivero-Baleine, T. S. Mayer, A. Swisher, M. Kang, A. Pogrebnyakov, J. Caraccio, T. Loretz, R. Hilton Jr., A. Yee, G. Schmidt, D. Moore, and K. Richardson, "Crystallization behavior and melt size in phase separated $GeSe_2$-As_2Se_3-$PbSe$ materials – impact on manufacturability," in preparation (2017).

45. M. Kang, A. M. Swisher, A. Pogrebnyanov, L. Liu, A. Kirk, S. Aiken, C. Rivero-Baleine, C. Smith, C. G. Pantano, T. S. Mayer, and K. Richardson, "Ultra-low dispersion multicomponent thin film chalcogenide glass for broadband gradient index optics," under review, Advanced Materials (2017).

46. S. D. Campbell, D. E. Brocker, J. Nagar, and D. H. Werner, "SWaP reduction regimes in achromatic GRIN singlets," Appl. Opt. **55,** 3594-3598 (2016).

47. M. A. Pickering, R. L. Taylor, and D. T. Moore, "Gradient infrared optical material prepared by a chemical vapor deposition process," Appl. Opt. **25,** 3364-3372 (1986).

48. G. I. Greisukh and S. A. Stepanov, "Design of a cemented, radial gradient-index triplet," Appl. Opt. **37,** 2687-2690 (1998).

49. D. T. Moore, "Design of singlets with continuously varying indices of refraction," J. Opt. Soc. Am. **61,** 886-894 (1971).

50. B. Arigong, J. Ding, H. Ren, M. Zhou, J. Shao, R. Zhou, H. Kim, Y. Lin, S. Fu, and H. Zhang,"Transformation optics for microwave and optical device design" in *2014 International Conference on Electromagnetics in Advanced Applications (ICEAA)* , 2014).

51. P. McCarthy, R. Berman, D. J. L. Williams, A. Yee, and D. T. Moore,"Optical design study in the 1-5um spectral band with gradient-index materials" in *International Optical Design Conference* , 2014).

52. B. Messerschmidt, T. Possner, and R. Goering, "Colorless gradient-index cylindrical lenses with high numerical apertures produced by silver-ion exchange," Appl. Opt. **34,** 7825-7830 (1995).

53. S. Houde-Walter and D. T. Moore, "Real-time index profile measurement during GRIN glass fabrication," Appl. Opt. **27,** 508-515 (1988).

54. V. Nguyen, S. Larouche, N. Landy, J. S. Lee, and D. R. Smith, "Quantitative comparison of gradient index and refractive lenses," J. Opt. Soc. Am. A **29,** 2479-2497 (2012).

55. L. G. Atkinson, S. Houde-Walter, D. T. Moore, D. P. Ryan, and J. M. Stagaman, "Design of a gradient-index photographic objective," Appl. Opt. **21,** 993-998 (1982).

56. M. Dussauze, V. Rodriguez, F. Adamietz, G. Yang, F. Bondu, A. Lepicard, M. Chafer, T. Cardinal, and E. Fargin, "Accurate second harmonic generation microimprinting in glassy oxide materials," Advanced Optical Materials **4,** 929-935 (2016).

57. A. Lepicard, "Design of Surface Chemical Reactivity and Optical Properties in Glasses," PhD in Materials Science and Engineering /Chemical Physics, University of Central Florida/University of Bordeaux (2016).

58. M. Dussauze, A. Lepicard, M. Bondu, V. Rodriguez, F. Adamietz, T. Cardinal, E. Fargin, and K. Richardson, "Device and method for inducing by thermal poling a spatially controlled refractive index gradient inside an amorphous inorganic material," European Patent application **#EP16176689.4,** (2016).

59. C. Saekeang, P. L. Chu, and T. W. Whitbread, "Nondestructive measurement of refractive-index profile and cross-sectional geometry of optical fiber preforms," Appl. Opt. **19,** 2025-2030 (1980).

60. J. B. MacChesney, P. B. O'Connor, and H. M. Presby, "A new technique for the preparation of low-loss and graded-index optical fibers," Proceedings of the IEEE **62,** 1280-1281 (1974).

61. D. Gibson, S. Bayya, and J. Sanghera,"Homogeneous and gradient index (GRIN) materials for multi-band IR optics" in *Classical Optics 2014* (Optical Society of America, 2014).

62. Y. Jin, H. Tai, A. Hiltner, E. Baer, and J. S. Shirk, "New class of bioinspired lenses with a gradient refractive index," J Appl Polym Sci **103,** 1834-1841 (2007).

63. D. Gibson, S. Bayya, V. Nguyen, J. Sanghera, M. Kotov, R. Miklos, and C. McClain,"IR-GRIN optics for imaging" in *Proc. of SPIE Vol. 9822* (SPIE, 2016).

64. D. Gibson, S. Bayya, J. Sanghera, V. Nguyen, D. Scribner, V. Maksimovic, J. Gill, A. Yi, J. Deegan, and B. Unger,"Layered chalcogenide glass structures for IR lenses" in *SPIE 9070, Infrared Technology and Applications XL*, 2014).

65. R. A. Flynn, E. F. Fleet, G. Beadie, and J. S. Shirk, "Achromatic GRIN singlet lens design," Opt. Express **21,** 4970-4978 (2013).

66. G. Beadie, J. S. Shirk, A. Rosenberg, P. A. Lane, E. Fleet, A. R. Kamdar, Y. Jin, M. Ponting, T. Kazmierczak, Y. Yang, A. Hiltner, and E. Baer, "Optical properties of a bio-inspired gradient refractive index polymer lens," Opt. Express **16,** 11540-11547 (2008).

67. G. Beadie, E. Fleet, and J. S. Shirk,"Gradient index polymer optics: achromatic singlet lens design" in Frontiers in Optics 2010/Laser Science XXVI (Optical Society of America, 2010).

68. J. Hunt, T. Tyler, S. Dhar, Y. Tsai, P. Bowen, S. Larouche, N. M. Jokerst, and D. R. Smith, "Planar, flattened Luneburg lens at infrared wavelengths," Opt. Express **20,** 1706-1713 (2012).

69. Y. Tsai, S. Larouche, T. Tyler, G. Lipworth, N. M. Jokerst, and D. R. Smith, "Design and fabrication of a metamaterial gradient index diffraction grating at infrared wavelengths," Opt. Express **19,** 24411-24423 (2011).

70. D. Le Coq, O. Caulier, E. Bychkov, J. Trolès, and P. Masselin,"Inscription of infrared waveguides in chalcogenide glasses by femtosecond laser" in *17th International Conference on Transparent Optical Networks (ICTON), 2015*, 2015).

71. K. Palanjyan, R. Vallee, and T. Galstian,"Photoinduced GRIN lens formation in chalcogenide Ge-As-S thin films" in *Proc. of SPIE Vol. 9288* (SPIE, 2014).

72. A. Saitoh and K. Tanaka, "Self-developing aspherical chalcogenide-glass microlenses for semiconductor lasers," Appl. Phys. Lett. **83,** 1725-1727 (2003).

73. O. M. Efimov, L. B. Glebov, L. N. Glebova, K. C. Richardson, and V. I. Smirnov, "High-efficiency Bragg gratings in photothermorefractive glass," Appl. Opt. **38,** 619-627 (1999).

74. O. M. Efimov, L. B. Glebov, V. I. Smirnov, and L. Glebova, "Process for production of high efficiency volume diffractive elements in photo-thermo-refractive glass," **US 09/648,293,** (2003).

75. O. Efimov, L. Glebov, and V. Smirnov, "High efficiency volume diffractive elements in photo-thermo-refractive glass," United States Patent 6,673,497 B2 (2004).

76. J. Wilkinson, "Characterization and optimization of solution-derived chalcogenide glass thin films," MS Thesis, Department of Materials Science and Engineering, Clemson University (2012).

77. S. Novak, "Nanoparticles in Solution-Derived Chalcogenide Glass Films," MS Thesis, Department of Materials Science and Engineering, Clemson University (2012).

78. Y. Zou, L. Moreel, H. Lin, J. Zhou, L. Li, S. Danto, J. D. Musgraves, E. Koontz, K. Richardson, K. D. Dobson, R. Birkmire, and J. Hu, "Solution processing and resist-free nanoimprint fabrication of thin film chalcogenide glass devices: inorganic-organic hybrid photonic integration," Advanced Optical Materials **2,** 759-764 (2014).

79. E. A. Sanchez, M. Waldmann, and C. B. Arnold, "Chalcogenide glass microlenses by inkjet printing," Appl. Opt. **50,** 1974-1978 (2011).

80. S. Novak, L. Scarpantonio, J. Novak, M. D. Prè, A. Martucci, J. D. Musgraves, N. D. McClenaghan, and K. Richardson, "Incorporation of luminescent CdSe/ZnS core-shell quantum dots and PbS quantum dots into solution-derived chalcogenide glass films," Optical Materials Express **3,** 729-738 (2013).

81. S. Novak, "Electrospray deposition of chalcogenide glass films for gradient refractive index and quantum dot incorporation," PhD Dissertation, Department of Material Science and Engineering, Clemson University (2015).

82. S. Novak, P. T. Lin, C. Li, C. Lumdee, J. Hu, A. M. Agarwal, P. G. Kik, W. Deng, and K. Richardson, "Direct electrospray printing of gradient refractive index chalcogenide glass films," ACS Appl. Mater. Interfaces (2017).

83. C. M. Schwarz, C. N. Grabill, G. D. Richardson, S. Labh, A. M. Lewis, A. Vyas, B. Gleason, C. Rivero-Baleine, K. Richardson, A. Pogrebnyakov, T. S. Mayer, C. Drake, and S. M. Kuebler, "Fabrication and characterization of micro-structures created in arsenic trisulfide chalcogenide glasses by multi-photon lithography," Journal of Micro/Nanolithography, MEMS, and MOEMS **16** (2) 023508 (2017)

84. C. M. Schwarz, C. N. Grabill, G. D. Richardson, S. Labh, B. Gleason, C. Rivero-Baleine, K. A. Richardson, A. Pogrebnyakov, T. S. Mayer, and S. M. Kuebler, "Processing and fabrication of micro-structures by multiphoton lithography in germanium-doped arsenic selenide," to be submitted to Optics Letters.

85. K. Sugioka, "Ultrafast Laser Micro- and Nano-Processing of Glasses," in *Lasers in Materials Science*, M. Castillejo, M. P. Ossi, and L. Zhigilei, eds. (Springer International Publishing, 2014), pp. 359-380.

86. L. Shah, "Femtosecond laser micro-machining of glasses and polymers in air," PhD Dissertation, College of Optics, the University of Central Florida (2001).

87. D. S. Correa, L. De Boni, A. J. Otuka, V. Tribuzi, and C. R. Mendonça, *Two-photon polymerization fabrication of doped microstructures*, Edited by Ailton De Souza Gomes 333 (2012).

88. A. Zoubir, M. Richardson, C. Lopez, L. Petit, K. A. Richardson, C. Rivero, and A. Schulte, "Femtosecond direct-writing of waveguide in non-oxide glasses," Proc. SPIE 5339, Photon Processing in Microelectronics and Photonics III, (2004).

89. A. Haché, P. A. Do, and S. Bonora, "Surface heating by optical beams and application to mid-infrared imaging," Appl. Opt. **51,** 6578-6585 (2012).

90. I. Mingareev, M. Ramme, and M. Richardson,"Material response of semiconductors irradiated with IR ultrashort laser pulses" in *CLEO Pacific Rim* (CLEO Pacific Rim, 2015).

91. H. Hu, D. A. Fishman, A. O. Gerasov, O. V. Przhonska, S. Webster, L. A. Padilha, D. Peceli, M. Shandura, Y. P. Kovtun, A. D. Kachkovski, I. H. Nayyar, A. E. Masunov, P. Tongwa, T. V. Timofeeva, D. J. Hagan, and E. W. Van Stryland, "Two-Photon Absorption Spectrum of a Single Crystal Cyanine-like Dye," J. Phys. Chem. Lett. **3,** 1222-1228 (2012).

92. K. A. Janulewicz, Y. V. Grigorov, N. T. Le, V. H. Nguyen, K. A. Tran, and Z. U. Rehman, "Absorption dynamics and structural changes due to laser-induced breakdown in transparent dielectrics," Proc.SPIE **9532,** 95320Z-95320Z-8 (2015).

93. M. Alubaidy, "Fabrication of nanofibers reinforced polymer microstructures using femtosecond laser material processing," PhD Dissertation, College of Optics, the University of Central Florida (2012).

94. M. Ramme, "Ultrafast laser material processing for photonic applications," PhD Dissertation, College of Engineering and Computer Science, the University of Central Florida (2013).

95. J. Choi, "Femtosecond laser written diffractive optical elements and their applications," PhD Dissertation, College of Optics, the University of Central Florida (2010).

96. S. Eaton, H. Zhang, P. Herman, F. Yoshino, L. Shah, J. Bovatsek, and A. Arai, "Heat accumulation effects in femtosecond laser-written waveguides with variable repetition rate," Opt. Express **13,** 4708-4716 (2005).

97. R. Le Harzic, N. Huot, E. Audouard, C. Jonin, P. Laporte, S. Valette, A. Fraczkiewicz, and R. Fortunier, "Comparison of heat-affected zones due to nanosecond and femtosecond laser pulses using transmission electronic microscopy," Appl. Phys. Lett. **80,** 3886-3888 (2002).

98. S. Heidrich, E. Willenborg, C. Weingarten, and R. Poprawe,"Polishing and form correction with laser radiation" in *Classical Optics* (Optical Society of America, 2014).

99. S. Maruo and J. T. Fourkas, "Recent progress in multiphoton microfabrication," Laser & Photonics Reviews **2,** 100-111 (2008).

100. M. Agarwala, D. Bourell, J. Beaman, H. Marcus, and J. Barlow, "Direct selective laser sintering of metalsnull," Rapid Prototyping Journal **1,** 26-36 (1995).

101. S. Richter, F. Zimmermann, S. Doring, A. Tunnermann, and S. Nolte, "Ultrashort high repetition rate exposure of dielectric materials: laser bonding of glasses analyzed by micro-Raman spectroscopy," Applied Physics A **110,** 9-15 (2013).

102. Y. Bellouard, A. Said, M. Dugan, and P. Bado, "Fabrication of high-aspect ratio, micro-fluidic channels and tunnels using femtosecond laser pulses and chemical etching," Opt. Express **12,** 2120-2129 (2004).

103. L. Petit, N. Carlie, T. Anderson, J. Choi, M. Richardson, and K. C. Richardson, "Progress on the photoresponse of chalcogenide glasses and films to near-infrared femtosecond laser irradiation: a review," IEEE Journal of Selected Topics in Quantum Electronics **14,** 1323-1334 (2008).

104. K. M. Davis, K. Miura, N. Sugimoto, and K. Hirao, "Writing waveguides in glass with a femtosecond laser," Opt. Lett. **21,** 1729-1731 (1996).

105. K. Richardson, "Engineering novel materials for infrared photonics," CREOL Affiliates Day lecture (2016).

106. R. J. King and S. P. Talim, "A Comparison of Thin Film Measurement by Guided Waves, Ellipsometry and Reflectometry," Optica Acta: International Journal of Optics **28,** 1107-1123 (1981).

107. J. Woollam, B. Johs, C. Herzinger, R. Synowicki, and C. Bungay, "Optical metrology," Critical Reviews of Optical Science and Technology **CR72,** 3-28 (1999).

108. S. Singh, "Refractive index measurement and its applications," Phys. Scripta **65,** 167 (2002).

109. N. C. Anheier and H. A. Qiao,"A mid-infrared prism coupler for bulk and thin film optical analysis" in *Proc. of SPIE Vol. 8016* (SPIE, 2011).

110. H. A. Qiao, N. C. Anheier, J. D. Musgrave, K. Richardson, and D. W. Hewak,"Measurement of chalcogenide glass optical dispersion using a mid-infrared prism coupler" in *Proc. of SPIE Vol. 8016* (SPIE, 2011).

111. N. Carlie, N. C. Anheier, H. A. Qiao, B. Bernacki, M. C. Phillips, L. Petit, J. D. Musgraves, and K. Richardson, "Measurement of the refractive index dispersion of As_2Se_3 bulk glass and thin films prior to and after laser irradiation and annealing using prism coupling in the near- and mid-infrared spectral range," Rev. Sci. Instrum. **82,** (2011).

112. H. A. Qiao, K. A. Lipschultz, N. C. Anheier, and J. S. McCloy, "Rapid assessment of mid-infrared refractive index anisotropy using a prism coupler: chemical vapor deposited ZnS," Opt. Lett. **37,** 1403-1405 (2012).

113. B. Gleason, K. Richardson, L. Sisken, and C. Smith, "Refractive index and thermo-optic coefficients of Ge-As-Se chalcogenide glasses," International Journal of Applied Glass Science **7,** 374–383 (2016).

114. B. Gleason, "Designing optical properties in infrared glass," PhD dissertation, Department of Material Science and Engineering, Clemson University TigerPrints **1568,** (2015).

115. P. Bon, G. Maucort, B. Wattellier, and S. Monneret, "Quadriwave lateral shearing interferometry for quantitative phase microscopy of living cells," Opt.Express **17,** 13080-13094 (2009).

116. J. Yao, P. Meemon, M. Ponting, and J. P. Rolland, "Angular scan optical coherence tomography imaging and metrology of spherical gradient refractive index preforms," Opt.Express **23,** 6428-6443 (2015).

117. J. Yao, P. Meemon, and J. P. Rolland,"Nondestructive metrology of layered polymeric GRIN materials using optical coherence tomography" in *Imaging and Applied Optics Technical Papers* (Optical Society of America, 2012).

118. J. Yao, J. Huang, P. Meemon, M. Ponting, and J. P. Rolland, "Simultaneous estimation of thickness and refractive index of layered gradient refractive index optics

using a hybrid confocal-scan swept-source optical coherence tomography system," Opt.Express **23,** 30149-30164 (2015).

119. A. Prasad, C. Zha, R. Wang, A. Smith, S. Madden, and B. Luther-Davies, "Properties of GexAsySe1-x-y glasses for all-optical signal processing," Opt. Express **16,** 2804-2815 (2008).

120. "M^3 Measurement Solutions Inc," http://www.m3msi.com/.

121. "Laser Heating - A Self Guided Tutorial," http://www.comsol.com/model/laser-heating-a-self-guided-tutorial-12317.

122. J. H. Bechtel, "Heating of solid targets with laser pulses," J. Appl. Phys. **46,** 1585-1593 (1975).

123. A. Zakery and S. R. Elliott, *Optical nonlinearities in chalcogenide glasses and their applications* (Springer, 2007).

124. J. N. Zemel, J. D. Jensen, and R. B. Schoolar, "Electrical and optical properties of epitaxial films of PbS, PbSe, PbTe, and SnTe," Phys. Rev. **140,** A330-A342 (1965).

125. L. Gampel and F. M. Johnson, "Index of refraction of single-crystal selenium," J. Opt. Soc. Am. **59,** 72-73 (1969).

126. L. Sisken, C. Smith, A. Buff, M. Kang, K. Chamma, P. Wachtel, J. D. Musgraves, C. Rivero-Baleine, A. Kirk, M. Kalinowski, M. Melvin, T. Mayer, and K. Richardson, "Evidence of spatially selective refractive index modification in a $15GeSe_2$-$45As_2Se_3$-$40PbSe$ glass ceramic through correlation of structure and optical property measurements for GRIN applications," Opt. Mat. Express **7** (2017) .

127. R. P. Wang, A. Smith, A. Prasad, D. Y. Choi, and B. Luther-Davies, "Raman spectra of Ge_xAsySe_{1-x-y} glasses," J. Appl. Phys. **106,** 043520 (2009).

128. M. V. Kumar, T. Ishikawa, J. T. Okada, and Y. Watanabe, "Fabrication of Advanced Glass and Ceramics by Containerless Levitation Process," Transactions of the Japan Society for Aeronautical and Space Sciences, Aerospace Technology Japan **12,** Ph_25-Ph_29 (2014).

129. M. Fateri, A. Gebhardt, S. Thuemmler, and L. Thurn, "Experimental investigation on selective laser melting of glass," Physics Procedia **56,** 357-364 (2014).

130. A. S. Rieck, "Laser marking process for vitrification of bricks and other vitrescent objects," United States Patent US6064034 A (2000).

131. P. R. Sahm, H. Jones, and C. M. Adam, *Science and Technology of the Undercooled Melt: Rapid Solidification Materials and Technologies* (Springer Netherlands, 2012).

132. B. Raj, *Frontiers in Materials Science* (Universities Press, 2005).

133. D. Lencer, M. Salinga, B. Grabowski, T. Hickel, J. Neugebauer, and M. Wuttig, "A map for phase-change materials," Nat Mater **7,** 972-977 (2008).